



**A University of Sussex PhD thesis**

Available online via Sussex Research Online:

<http://sro.sussex.ac.uk/>

This thesis is protected by copyright which belongs to the author.

This thesis cannot be reproduced or quoted extensively from without first obtaining permission in writing from the Author

The content must not be changed in any way or sold commercially in any format or medium without the formal permission of the Author

When referring to this work, full bibliographic details including the author, title, awarding institution and date of the thesis must be given

Please visit Sussex Research Online for more information and further details



# Reconfigurable Mid-Air Displays

Mohd Adili Norasikin

Submitted for the degree of Doctor of Philosophy

University of Sussex

October 2019



## UNIVERSITY OF SUSSEX

Mohd Adili Norasikin, Doctor of Philosophy

### Reconfigurable Mid-Air Displays

#### Summary

This thesis addressed the difficulties involved in reconfiguring permeable mid-air displays (e.g., fog screens) through the experimental investigations of three interactive prototypes: MistForm, SoundBender, and SonicSpray. Each of the prototypes includes their specific reconfigurability techniques. The discussion begins in Chapter 1. Chapter 2 described a straightforward technique used by MistForm to coarsely and mechanically reconfigure the permeable mid-air display. MistForm can adaptively deform its display surface to a specific condition through linear mist emitters controlled by five actuators. It is capable of turning problems into solutions, for example, a concave display can be used as a shared screen while convex shape as a personal screen. However, the investigation found the MistForm to be large and noisy. These challenges have led to a study investigation of SoundBender in Chapter 3. Chapter 3 described an investigation of a hybrid technique that reconfigured non-solid diffusers. The method can precisely manipulate any given complex sound field, encoded by a metamaterial (MM) mounted on phased array transducer (PAT). The force from the sound affected the surrounding particles. The technique can be used to reconfigure matter such as paper, mist, and flame in air space. However, the chapter did not focus on coordinating its use specifically for permeable mid-air displays. Therefore, this thesis carried out an investigation of SonicSpray in Chapter 4. It describes a technique to reconfigure mid-air display of permeable matter (i.e., aerosols) precisely by using a small form factor PAT. This thesis ends with a conclusion in Chapter 5. The next generation of mid-air displays needs to be in small form factor, multipurpose and controllable, which have been introduced and demonstrated in this thesis. The research in this thesis can facilitate the future design of displays. However, this thesis highlights the response rate of the permeable particles, the primary concern yet to be solved. The airflow speed of the particles was found to be decreased proportionally to the number of transducers used. In the future, for better control the display, researchers should improve the response rate of the particles, for example, using sources with higher sound power.

# Acknowledgements

In the name of Allah, the Entirely Merciful, the Especially Merciful. Praise is due to Allah, Lord of the worlds.

First and foremost, my infinite thanks to my beloved wife,

*Nur Shahidah Hidayu Mohd Nasir*

Throughout my PhD, you have always been caring, loving and supportive, through the ups and downs. I could not have done it without you. You are faithful in supporting me throughout this journey and I appreciate it eternally. Enormous thanks to my precious princesses Nia Adlina and Ana Sumayyah, and my little prince Ali Imran. You all have been the most precious strengths in my journey. To my mum, Rodziah Abd Hamid, dad, Norasikin Mat Ani, dad-in-law, Mohd Nasir A Rahman, and mum-in-law, Zuraida' Ani AB Razak; you are my heart. Your steadfast encouragement and prayers have allowed me to complete this PhD successfully. Thank you for being part of the journey. To my sisters, Kak Long Adila and Adik Nazurah, my brothers, Fadhil and Syukri, my sister-in-law, Swani, and my brothers-in-law, Rasid, Piang, Sarow, and Adik Syahmi; you are lovely people with kind hearts. Thank you for always being there to help whenever I really needed it. I love you all very much.

Special thanks to my supervisors, Professor Sriram Subramanian and Dr Diego Martinez Plasencia. Sriram, throughout my PhD, you have always encouraged me to strive for greater things. In the process, you have provided excellent feedback to help me learn and develop as a researcher. Thank you for your supportive supervision throughout the journey. Thank you for your research grant, which gave me the opportunity to attend SIGGRAPH 2017 in Los Angeles, USA – the world’s largest annual conference and exhibition in computer graphics and interactive techniques – and also for your support in my participation at SIGCHI Summer School Computational Fabrication and Smart Matter<sup>1</sup>, a workshop that allowed me to learn new skills from excellent senior mentors in HCI, and to build my research networks with the best students in computing and fabrication for HCI. The grant has helped me to run my research smoothly and present it at several prestigious HCI conferences, including the ACM CHI Conference on Human Factors in Computing Systems (CHI 2017)<sup>2</sup>, in Colorado, USA; the ACM User Interface Software and Technology Symposium (UIST 2018)<sup>3</sup>, in Berlin, Germany; and the ACM International Conference on Interactive Surfaces and Spaces (ISS 2019)<sup>4</sup>, in Daejeon, South Korea. I enjoyed the valuable experiences of meeting interesting people and potential collaborators at the conferences. Diego, thank you for your support, expertise and passion throughout the journey. Your appreciation of all my works has made me feel that they are special and priceless. I feel honoured to have had this opportunity to work with both of you, to be part of a growing and flourishing field of research, and to make this great thing together.

I am grateful to my funders, the Ministry of Education, Malaysia, and Universiti Teknikal Malaysia Melaka, for supporting this PhD studentship. I am thankful to have been given the opportunity to conduct research in the Interact Lab, University of Sussex and to meet incredible people with invaluable experience who are always willing to help others. To Dr Gianluca Memoli, thank you for your support, both academically and emotionally. From our first conversation about acoustic metamaterials to working on several excellent papers together, I am grateful for your brilliant advice, patience and constant presence during the journey.

A huge thank you goes to all of the fantastic members of the Interact Lab (both past and present): Yutaka, Roberto, Patricia, Ben, William, Spyros, Jordi, Luis Berna, Luis Video, Rafa, Tom, Lucy, Ryuji, Daniel, Deepak, Michi. Thanks to the people who have

---

<sup>1</sup>SIGCHI Summer School Computational Fabrication and Smart Matter (<http://scf-summerschool.com/>)

<sup>2</sup>CHI 2017 (<https://chi2017.acm.org/>)

<sup>3</sup>UIST 2018 (<http://uist.acm.org/uist2018/>)

<sup>4</sup>ISS 2019 (<https://iss.acm.org/2019/>)

been involved with my research. The passion it took to share your experiences with me has not gone unacknowledged. I am thankful to have you all. Lastly, I would like to thank my friends and the groups that became a part of my life and made my time at Brighton was enjoyable. I met many friends and groups which have become part of my life. I am grateful for the time spent with my lab mates and friends, for my badminton buddies and our astounding badminton games, and for many other people and our fond memories. Thank you.

Mohd Adili Norasikin  
*University of Sussex*  
October 2019

# List of published papers

1. Yutaka Tokuda, Mohd Adili Norasikin, Sriram Subramanian, and Diego Martinez Plasencia. 2017. MistForm: Adaptive Shape Changing Fog Screens. In Proceedings of the 2017 CHI Conference on Human Factors in Computing Systems (CHI '17). Association for Computing Machinery, New York, NY, USA, 4383–4395. <https://doi.org/10.1145/3025453.3025608>
2. Mohd Adili Norasikin, Gianluca Memoli, Diego Martinez Plasencia, and Sriram Subramanian. 2017. Acoustic levitation by a metamaterial-based cloak. In 24<sup>th</sup> International Congress on Sound and Vibration (ICSV24). 1-8. <https://iiav.org/icsv24/>
3. Mohd Adili Norasikin, Diego Martinez Plasencia, Spyros Polychronopoulos, Gianluca Memoli, Yutaka Tokuda, and Sriram Subramanian. 2018. SoundBender: Dynamic Acoustic Control Behind Obstacles. In Proceedings of the 31<sup>st</sup> Annual ACM Symposium on User Interface Software and Technology (UIST '18). Association for Computing Machinery, New York, NY, USA, 247–259. <https://doi.org/10.1145/3242587.3242590>
4. Mohd Adili Norasikin, Diego Martinez Plasencia, Gianluca Memoli, and Sriram Subramanian. 2019. SonicSpray: A Technique to Reconfigure Permeable Mid-Air Displays. In Proceedings of the 2019 ACM International Conference on Interactive Surfaces and Spaces (ISS '19). Association for Computing Machinery, New York, NY, USA, 113–122. <https://doi.org/10.1145/3343055.3359704>

# Contents

<b>1</b>	<b>Introduction</b>	<b>1</b>
1.1	The significant research problem . . . . .	11
1.2	Approach . . . . .	12
1.3	Main contributions . . . . .	14
1.4	Thesis structure . . . . .	14
1.4.1	Chapter 2, MistForm: Adaptive shape-changing fog screens . . . . .	15
1.4.2	Chapter 3, SoundBender: Dynamic acoustic control behind obstacles . . . . .	16
1.4.3	Chapter 4, SonicSpray: A tool for reconfiguring permeable mid-air displays . . . . .	17
1.4.4	Chapter 5, Conclusion and future work . . . . .	17
<b>2</b>	<b>MistForm: Adaptive shape-changing fog screens</b>	<b>18</b>
2.1	Introduction . . . . .	18
2.2	Related work . . . . .	20
2.2.1	Shape changing displays . . . . .	20
2.2.2	Permeable mid-air displays . . . . .	22
2.3	MistForm: Shape changing fog screen . . . . .	25
2.3.1	Modular design . . . . .	27
2.3.2	Challenges and general approach . . . . .	28
2.4	Shape reconstruction . . . . .	28
2.4.1	Modelling of pipe shapes . . . . .	28
2.4.2	Ground truth capture . . . . .	29
2.4.3	Data-driven shape reconstruction . . . . .	30
2.5	Projecting on MistForm . . . . .	33

2.5.1	Projector calibration . . . . .	33
2.5.2	Rendering algorithm . . . . .	34
2.5.3	Evaluation . . . . .	37
2.6	Exploring interaction possibilities . . . . .	38
2.6.1	Identifying affordances . . . . .	40
2.6.2	Interacting with 2D content . . . . .	41
2.6.3	Interacting with 3D content . . . . .	42
2.7	Discussion . . . . .	44
2.8	Conclusion . . . . .	46
<b>3</b>	<b>SoundBender: Dynamic acoustic control behind obstacles</b>	<b>48</b>
3.1	Introduction . . . . .	48
3.2	Related work . . . . .	51
3.2.1	Transducer-based acoustic modulators . . . . .	51
3.2.2	Metamaterial-based acoustic modulators . . . . .	55
3.3	Preliminary study of a self-bending beam and reconfiguration method . . . . .	57
3.3.1	Materials and method . . . . .	61
3.3.2	Results . . . . .	62
3.4	SoundBender: Hybrid sound modulators and dynamic self-bending beams . . . . .	67
3.4.1	Step (i): computation of the self-bending curve . . . . .	68
3.4.2	Step (ii): computation of phases to recreate the sound field . . . . .	69
3.4.3	Step (iii): discretisation and fabrication of the metamaterial . . . . .	71
3.4.4	Step (iv): modulator spacing and coupling . . . . .	72
3.4.5	Step (v): algorithms for dynamic control through a PAT . . . . .	75
3.5	Experimental setup . . . . .	76
3.5.1	Finite element method simulation . . . . .	77
3.5.2	Sound field measurement system . . . . .	77
3.6	Evaluation . . . . .	78
3.6.1	Self-bending beam reconstruction . . . . .	78
3.6.2	Dynamic control of the self-bending beam . . . . .	80
3.7	Example applications . . . . .	81
3.7.1	Around-object tactile feedback . . . . .	81

3.7.2	Around-object levitated objects . . . . .	82
3.7.3	Around object non-solid features . . . . .	83
3.8	Limitations and discussion . . . . .	83
3.9	Conclusion . . . . .	85
<b>4</b>	<b>SonicSpray: a technique for reconfiguring permeable mid-air displays</b>	<b>86</b>
4.1	Introduction . . . . .	86
4.2	Related work . . . . .	89
4.2.1	Impermeable mid-air displays . . . . .	89
4.2.2	Permeable mid-air displays . . . . .	91
4.3	SonicSpray: technique for reconfiguring non-solid matter in free space . . .	92
4.3.1	Basic Bessel beam creation . . . . .	92
4.3.2	Lateral reconfiguration of the basic beam . . . . .	93
4.4	Experimental characterisation . . . . .	96
4.4.1	Experimental setup . . . . .	97
4.4.2	Camera-projector calibration . . . . .	98
4.4.3	Speed and laminar airflow test . . . . .	101
4.4.4	Minimum transducers and SPL analysis . . . . .	102
4.5	Evaluation . . . . .	104
4.5.1	Lateral mist resolution by oscillation frequencies . . . . .	104
4.5.2	Lateral mist resolution according to number of transducers . . . . .	105
4.6	Enabling applications with SonicSpray . . . . .	106
4.7	Discussion . . . . .	107
4.8	Conclusion . . . . .	108
<b>5</b>	<b>Final conclusion and future work</b>	<b>109</b>
5.1	Recapitulation of research purpose and findings . . . . .	109
5.2	Contribution to the body of knowledge . . . . .	110
5.3	Implications of the findings . . . . .	110
5.4	Research strengths and limitations . . . . .	111
5.4.1	Strengths . . . . .	111
5.4.2	Limitations . . . . .	114



5.5	Future work . . . . .	114
5.5.1	Reconfigurable volumetric displays of permeable materials . . . . .	114
5.5.2	Dynamic displays with tunable MM . . . . .	116
5.5.3	Reconfigurable displays of trapped permeable materials . . . . .	117
5.6	Final conclusion . . . . .	117
	<b>Bibliography</b>	<b>119</b>
	<b>List of tables</b>	<b>135</b>
	<b>List of figures</b>	<b>138</b>
	<b>List of acronyms</b>	<b>140</b>

# Chapter 1

## Introduction

The concept of mid-air displays have been envisioned in films and science fiction for many years, for example, Star Wars as in Figure 1.1 and Iron Man as in Figure 1.2. The interactive graphics community has also proposed futuristic concepts and visions for the displays such as ‘Ultimate Display’ (Sutherland, 1965) and ‘Radical Atoms’ (Ishii et al., 2012). In these visions, users are able to interact with dynamic displays through their computationally reconfigurable materials. The displays can offer proactive users rather than proactive systems and can enhance users’ experiences and engagement (Rogers, 2006; Alrøe et al., 2012) because they allow users to experience visual content without any human augmentation (e.g., a head-mounted display (HMD)).



Figure 1.1: A mid-air display envisioned in Star Wars: Episode IV - A New Hope (Lucas, 1977).

Many real world prototypes have emerged to realise the concept, for instance, Holovect (Ruiz-Avila, 2016) as in Figure 1.3, AIREAL (Sodhi et al., 2013), MisTable (Martinez Plasencia et al., 2014), and others.

cia et al., 2014b), PixieDust (Ochiai et al., 2014), SensaBubble (Seah et al., 2014), Gushed Diffusers (Suzuki et al., 2016), Point-and-Shake (Freeman et al., 2018), and Luciola (Qiu et al., 2018). PixieDust (Ochiai et al., 2014), for instance, directly projects its digital contents onto its dynamic levitated beads in free space and coordinates user interactions and the digital content with a motion tracking system. These types of display demonstrate cutting-edge technologies and could pave the way for future commercial displays.



Figure 1.2: A mid-air display envisioned in Iron Man 3 (Black, 2013).

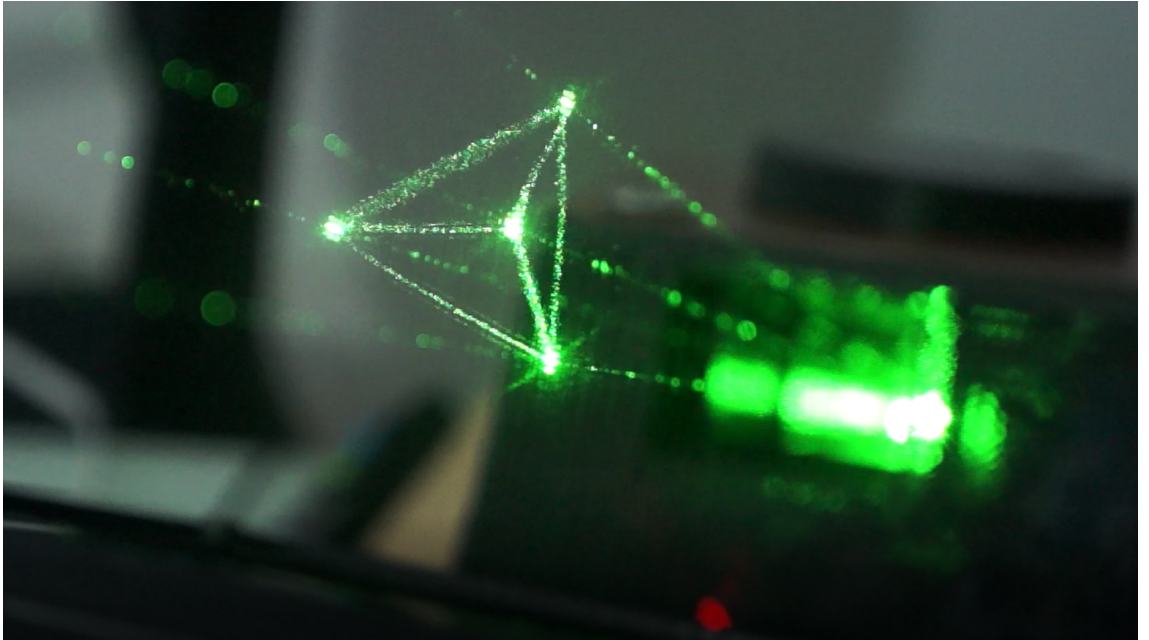


Figure 1.3: A mid-air display made of a laser system and dust (Ruiz-Avila, 2016).

To understand about the reconfigurable mid-air displays, this thesis places them in the context of three concepts (as illustrated in Figure 1.4): light converging, light diverging, and light scattering. These concepts have different permeability. The impermeable

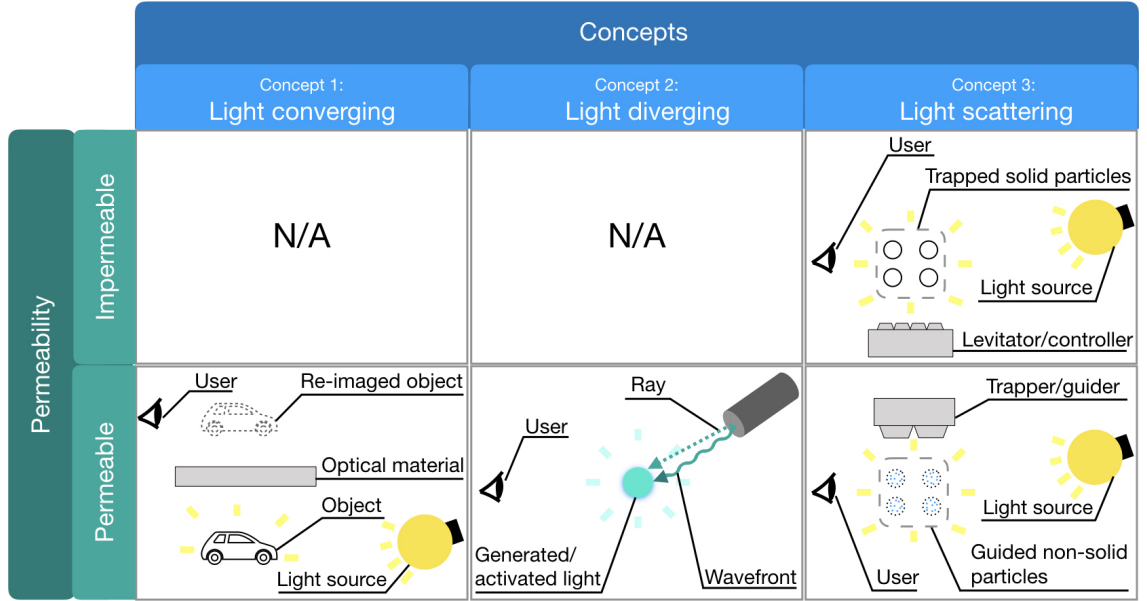


Figure 1.4: Visual mid-air display concepts.

feature, which can be found only in light scattering concept, do not allow anything to pass through the materials and thus become an obstruction to either engagement or sensing technology since light rays are not able to pass through. In contrast, the permeable feature, which can be found in all three concepts, allow gases, liquids and solids to pass through the material. This allows users to share and comment on a task with clients or peers without any obstruction, as in the real world (e.g., nurses in an operation theatre). The permeable feature will unleash the full ability of the user’s actual hands and physical actions. Such abilities include interaction (assuming required sensing technology) and recognising gestures (client pointing at a part of the object) and facial expressions.

The first concept, light converging, as illustration in Figure 1.4, forms an optical real image by intersecting the light rays of an object through optical materials (e.g., optical combiners (Bimber, 2004), concave mirrors (Butler et al., 2011; Monnai et al., 2014) and beam-splitter mirrors (Yamamoto et al., 2014; Tokuda et al., 2015)). Figure 1.5 shows a photo of the display that uses a beam splitter as its optical material. This concept can also be combined with a swept-volume display to create a volumetric display system (Hunter et al., 2017). There are two disadvantages to this concept. First, the eye has difficulty in focusing both real objects (e.g., the user’s finger) and the real optical image of the converged light. This scenario causes users to suffer from eye fatigue after extended use (Zhou et al., 2018). Second, although the displays are permeable, their viewing angle is limited, which constraints users to a fixed position, making screen sharing less practical.

Instead of converging rays, the second concept, as the illustration in Figure 1.4 and

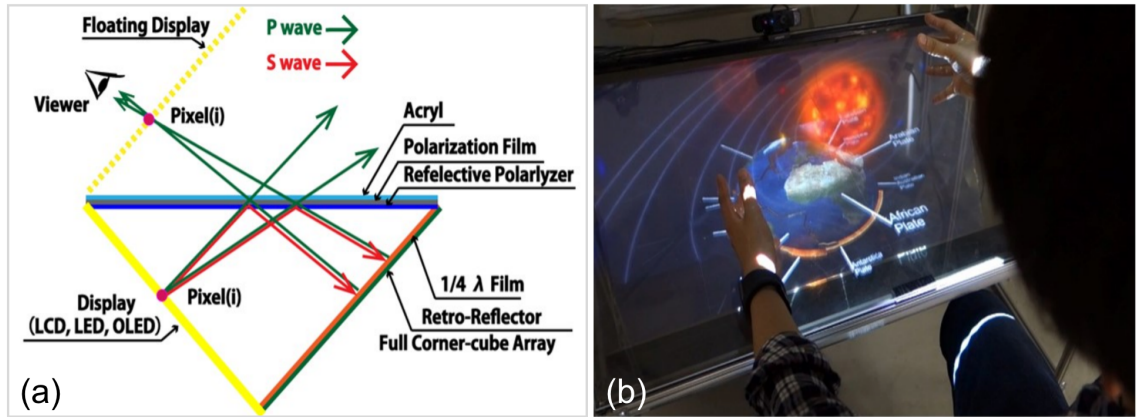


Figure 1.5: A mid-air display example of the light converging concept: (a) the principle of converging the light through an optical material (i.e., a beam splitter), (b) the outcome of the display (Tokuda et al., 2015).

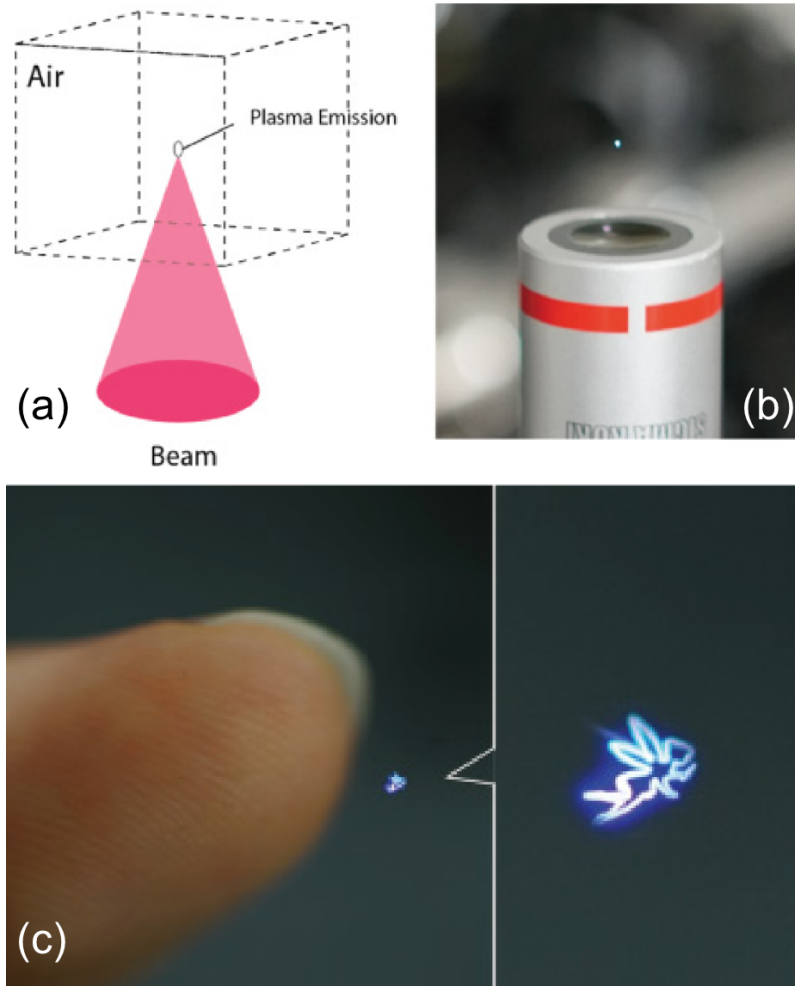


Figure 1.6: A mid-air display example of the light diverging concept: (a) the illustration of a laser-plasma induced by focused femtosecond laser, (b) a photo of the real plasma emission, (c) rendered graphics in the air using the femtosecond lasers (Ochiai et al., 2016b).



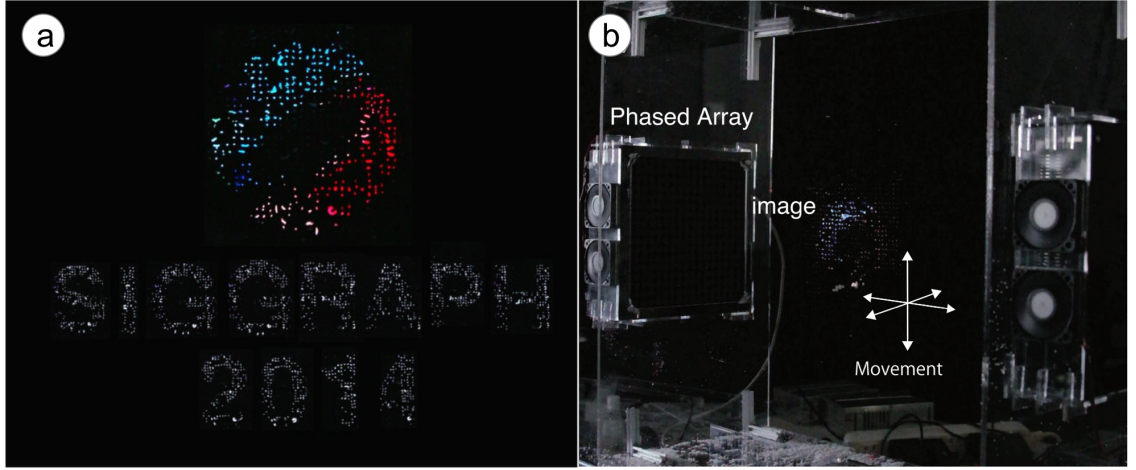


Figure 1.7: A mid-air display example of the light scattering concept that uses ultrasound approach: (a) a mid-air display screen of levitated particles and projected graphical contents, (b) the setup for the ultrasonics levitator (Ochiai et al., 2014).

Figure 1.6 (a), diverges light and form points in free space through a phenomenon called plasma emission. This concept focuses a pulsed laser at a specific point in the air, ionises the molecules there and releases photons, making the emitters co-located with the actual image points (Kimura et al., 2006; Saito et al., 2008; Kimura et al., 2011; Ochiai et al., 2016b). Figure 1.6 (b-c) shows the real photo of a display that uses plasma emission. The pulsed laser occurs in a femtosecond timescale; therefore, the energy is completely transferred to the point of interest before the heat is scattered to the surroundings. However, even though this concept offers advanced technology in visualisation, the safety issue associated with this display (in particular the danger to users' eyes and skin) is still the primary concern (Ochiai et al., 2016b), which makes this technology less suitable for commercial displays. The reason for this is that the plasma generated at a specific point emits energy in all direction.

The third concept in Figure 1.4, scatters light rays from its materials, either through permeable (as in Figure 1.8) or impermeable material (as in Figure 1.7 (a)). This concept includes levitators (e.g., as in Figure 1.7 (b) or manipulators (e.g., as in Figure 1.8 (a-b)) to control voxels (i.e., light scattering particles) in free air, and various approaches, such as ultrasound (Ochiai et al., 2014; Sahoo et al., 2016; Freeman et al., 2018; Qiu et al., 2018), magnetic (Lee et al., 2011), airborne (Alrøe et al., 2012), electrical (Sahoo et al., 2015; Berthelot and Bonod, 2019) and optical traps (Smalley et al., 2018b), have been used to create displays of impermeable materials.

The light scattering particle displays of the ultrasound approach (Omrou et al., 2016;

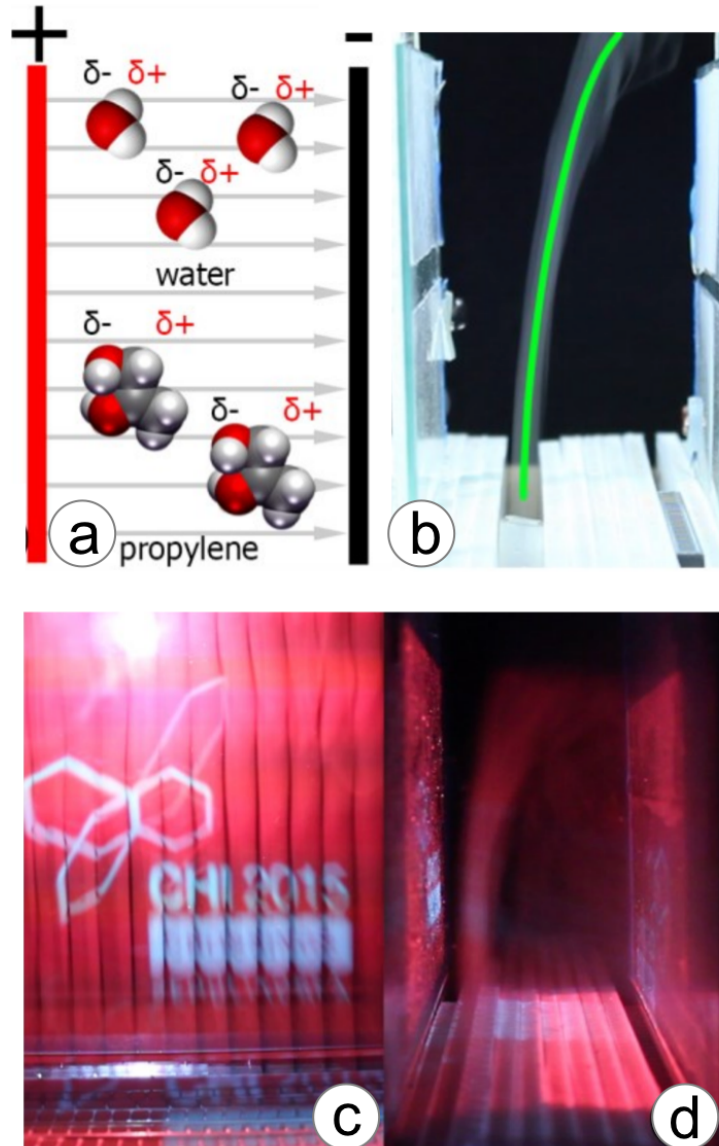


Figure 1.8: A mid-air display example of light scattering concept that is using electrostatic approach: (a) polarity of water and propylene molecules are mobile in electric fields, and the work proposed it as a permeable mid-air display, (b) fog particles with polarity can follow a trajectory, (c) a front view of the permeable display with a projected graphical contents, (d) the side view of permeable display (Sahoo et al., 2015).

[Sahoo et al., 2016](#)) use a sound field to create voxel traps (e.g., standing wave, twin traps, bottle traps). The traps hold and floating objects in them to create a display, and this display position can be moved in free space by reconfiguring the sound field. [Omrou et al. \(2016\)](#) created a reconfigurable chart from the traps and controlled it using the standing wave principle. When two opposed transducers emitted sound, at a constant amplitude and phase, objects could be trapped at the low-pressure nodes in the standing wave. The system was able to move the traps through the computation of the phase difference of the standing wave. [Sahoo et al. \(2016\)](#) enhanced the levitated display by allowing rotation of the voxels. This was achieved through material coating: a patch of electrically charged material was placed on one side of the voxel, then the system created and controlled electric fields from two transparent electrodes. The system modulated voltage through the electrodes, forcing the charged voxels to rotate and thus change the orientation of the voxels. The ultrasound approach was independent in terms of the material it could manipulate (except the one from [Sahoo et al. \(2016\)](#) above). It was able to levitate various materials, including polystyrene beads ([Omrou et al., 2016](#)), insects, electronic components, fluids, and even food ([Xie et al., 2006](#); [Marzo et al., 2017a](#); [Vi et al., 2017](#)). However, the ability of this approach to reconfigure displays of permeable materials was relatively low.

[Berthelot and Bonod \(2019\)](#) used an electrical approach for their light-scattering display. Specifically, the researchers used an electrically driven planar trap to levitate a small light scattering particle (i.e., nano-sized matter) into the air and manipulated the particle’s motion to draw in free space. This levitation was achieved by polarising electrodes (using DC or AC electrical voltage). The system had two inner- and outer-ring electrodes surrounded by four compensation DC electrodes, fabricated on a commercial printed circuit board. It used a high-voltage amplitude and a strong trap that allowed for high-speed displacement. It oscillated the electric fields at high frequencies (150 kHz) to reconfigure the trajectory of electrically charged particles in three-dimensional (3D) space and encoded the trajectory of the particles with electric voltage from the stationary planar electrodes. It illuminated the particles with a green laser beam and reconfigured their motion to draw graphics in free air (circles, squares and stars, for example). This display can be scaled up; however, this incurs a high price point due to the use of the laser.

An example of a magnetic light scattering display is ZeroN ([Lee et al., 2011](#)). It features a single mid-air element that relies on electromagnets. The element, which is a magnetic



ball, floats in the air and the system can track and project useful graphical content onto it. ZeroN demonstrates a few useful applications, such as simulation of the solar system for education – users can directly touch the floating ball due to the strong trap imposed by the approach. However, the system requires a bulky apparatus to work. It requires not only electromagnetism to reconfigure the ball movement in the vertical direction, but also mechanical actuators for the horizontal direction.

One mid-air display example that uses an airborne light-scattering display is Aerial Tunes (Alrøe et al., 2012). It floats a foam ball based on an airflow field. This work combines a sensor and air stream, creating a physical soundscape slider that is floating. It allows a user to select and place the ball between 2–30 cm above its base and remain floating. It follows a concept close to the Tibetan singing bowl <sup>1</sup>, producing different tones of sound based on the height of the ball. However, this system requires prolonged engagement due to the instability of the floating balls and the challenges of understanding the system. This display includes impermeable material, which obstructs the view at the back of the display and makes interaction for opposing users (e.g., sharing comments and feedback between peers) less engaging.

The light scattering display of an optical trap display (OTD) as in Figure 1.9 (Smalley et al., 2018b). It traps a particle in an optical trap and reconfigures its motion in free space to draw an image. In particular, it forms a voxel in mid-air by first confining a cellulose particle (i.e., impermeable material) – a common product of the paper-making industry – in a near-invisible (405-nm wavelength) optical trap. The trap position is then reconfigured in a volume while being illuminated with a red-green-blue (RGB) laser light. This display system can create fine points of full-colour images in mid-air (1,600 dots per inch). However, it suffers from poor scanning speed. For example, 18.9 second was required to draw a 3 cm x 2 cm image of Big Buck Bunny.<sup>2</sup> In addition, the particle is sensitive to airflow and the system depends on an enclosed setup for a robust OTD system.

The displays of the light-scattering concept above are reconfigurable. However, they share a common limitation: they are impermeable and untouchable. All of these displays depend on the levitated matter in free space; therefore, directly touching the display can disturb the trap (Freeman et al., 2018) and cause a system failure. This flaw imposes a negative impact on user engagement. In contrast, the light-scattering concept of permeable particles allows the user to reach- and walk-through the display since the materials used are

---

<sup>1</sup><https://www.youtube.com/watch?v=FZ1YgV5zwxg>

<sup>2</sup><https://peach.blender.org/>

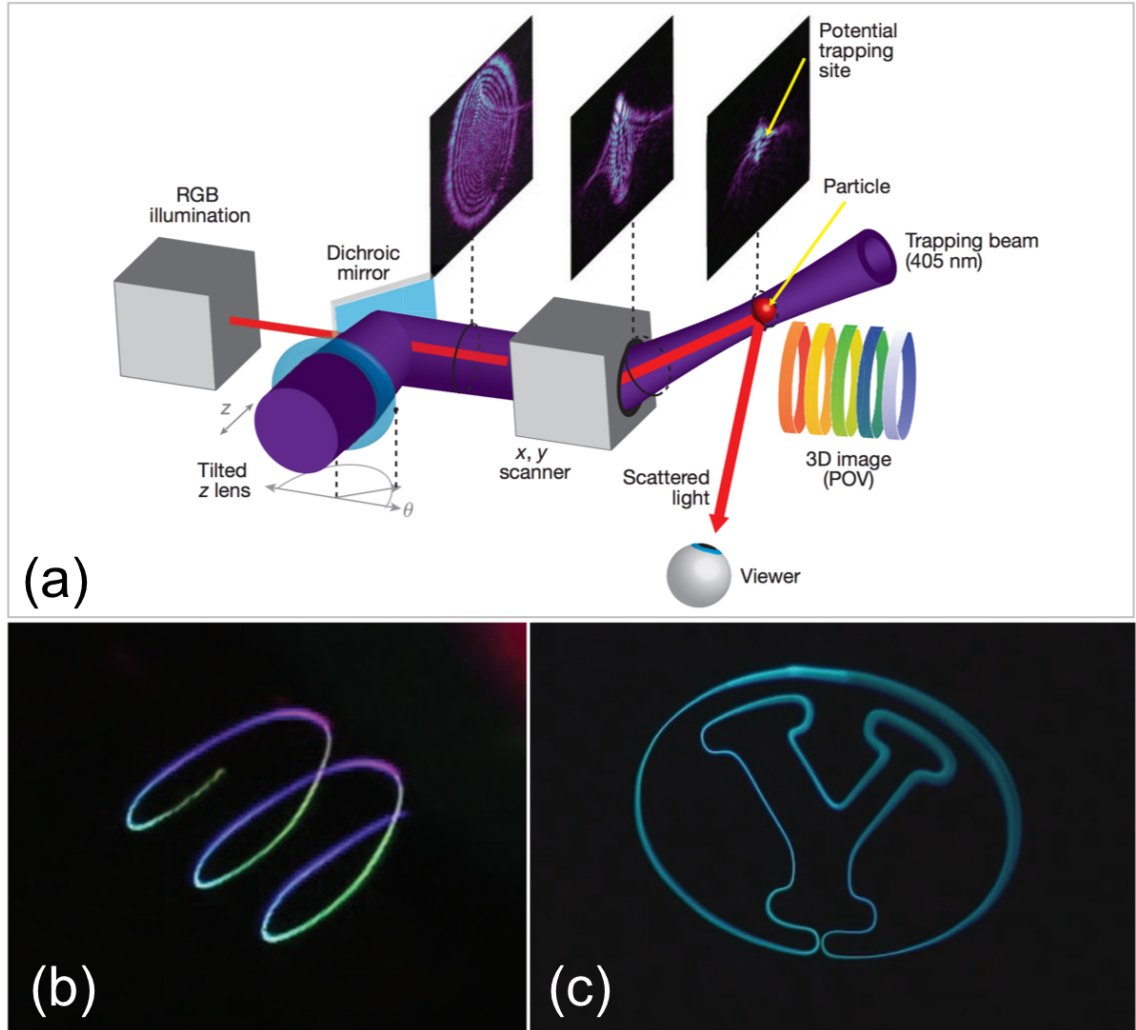


Figure 1.9: A mid-air display example of the light scattering concept that uses optically trapped particle: (a) an optomechanical levitator and display system to trap and reconfigure and illuminate a particle in mid-air, (b) a rendered helix in mid-air, (c) an outline of a logo rendered in mid-air ([Smalley et al., 2018b](#)).

safe (i.e., mist, dust, water). Some examples of this are fog screens (Rakkolainen, 2008b; Palovuori and Rakkolainen, 2012; Martinez Plasencia et al., 2014b; Lam et al., 2014), water-drop displays (Eitoku et al., 2006, 2009; Barnum et al., 2010) and illuminated-dust displays<sup>3</sup> (Perlin et al., 2006; Ruiz-Avila, 2016).

Illuminated-dust displays, which include infrared (IR) lasers either as light sources or dust detectors, detect dust particles (Perlin et al., 2006) in free air and illuminate the dust with a laser. The illumination brightness is determined by the distance from the dust to the light source. It can also be achieved by reconfiguring the properties of the air (i.e., humidity, temperature, refractive index), which also contains dust (Ruiz-Avila, 2016). By doing so, the air will react to light differently than its surroundings, making it visible. The main issue with this type of display is that the instruments are expensive, which is the biggest challenge for commercialisation (Smalley et al., 2018a).

Water-drop displays (Eitoku et al., 2006, 2009; Barnum et al., 2010), which include water pump, projector and solenoid, have demonstrated their capability to create two-dimensional (2D) screen in mid-air. Gatorade<sup>4</sup> adapted the system and combined it with motion-capture technology to advertise<sup>5</sup> a commercial product. The system used 2,500 switches to reconfigure the water on and off, creating the moving image of a person engaging in sports activities such as running and hopping. This type of display is impressive. However, in a scenario in which a user interacts with the display, the user and the ground will be wet; therefore, this display is not capable of being used interactively, and there are safety concerns due to the splashing of water drops causing slippery floors. Additionally, the display requires a water pump and solenoid to push the water uniformly through linear holes on a long pipe, which makes it bulky.

Fog screens make use of a linear mist emitter guided by an airflow mechanism to form a laminar curtain of mist. The system then projects graphical content onto the curtain using a light projector. With a combination of sensing technology, it has been shown to enable an interactive walkthrough interface for applications such as advertisements (Rakkolainen and Lugmayr, 2007), mid-air information in the airport (Rakkolainen, 2008b) and interactive mid-air drawing systems (Rakkolainen and Palovuori, 2005). Fog screen displays have been studied for a long time, but they are still bulky due to the requirement of fans and physical guiders for the mist emitter, which makes the systems less practical. However, of the three concepts, the light scattering concept of fog screens has the greatest potential to

---

<sup>3</sup>[https://www.youtube.com/watch?v=THYhP3\\_wmLs](https://www.youtube.com/watch?v=THYhP3_wmLs)

<sup>4</sup><https://www.gatorade.com/>

<sup>5</sup>[https://www.youtube.com/watch?v=FG\\_11oacWoQ](https://www.youtube.com/watch?v=FG_11oacWoQ)

become a practical mid-air display. This is because the user can reach through the display, both real objects and generated graphics are always in focus, and the particles used are dry and safe. The user can reach out or walk through without any concern about slipping, safety or system failure. However, the main challenges for the permeable displays within this concept are the difficulties associated with their reconfiguration ([Sahoo et al., 2015](#)) and the high price point ([Smalley et al., 2018a](#)).

## 1.1 The significant research problem

The reason why permeable mid-air displays are difficult to reconfigure is that the materials used are non-solid ([Sahoo et al., 2015](#)), which means that they are difficult to shape or trap. Despite the work of [Perlin et al. \(2006\)](#) and [Ruiz-Avila \(2016\)](#), which has demonstrated ways of detecting and illuminating dust in free air, the system is costly ([Smalley et al., 2018a](#)). These challenges have placed serious limitation on the commercialisation of these displays. Therefore, this thesis raises three questions:

1. What are the techniques that can sufficiently reconfigure mid-air displays?
2. What is the technique that can control permeable mid-air displays with sufficient reconfigurability (coarse or fine manipulation) and can be used in HCI applications?
3. How does the permeable mid-air display reconfiguration technique perform?

To sufficiently control permeable mid-air displays, this thesis hypothesises a technique can be studied and designed. The study will permit the exploration of strategies to co-ordinate its capabilities, which can lead to an understanding of adequate reconfigurability (coarse or fine manipulation) for HCI applications. As per the hypothesis, this thesis projects three aims:

1. To study techniques of adequate reconfigurability (coarse or fine) for permeable mid-air displays.
2. To design techniques of adequate reconfigurability (coarse or fine) for permeable mid-air display in HCI applications.
3. To evaluate the performance of the reconfiguration technique.

## 1.2 Approach

In the literature, there are various approaches to reconfiguring permeable mid-air displays including ultrasonic, mechanical, electrostatic, and air modification. This thesis then maps their practicality (price, form factor and reach-through ability) using a starring system, as seen in Table 1.1.

A system with ultrasonics requires at least a phased array transducer (PAT) to reconfigure particles in the air. This makes use of small transducers ( $\phi = 10\text{mm}$ ) that can be found in cheap off-the-shelf products. The technique manipulates particles in the air with sound field regeneration through the PAT. By doing this, there is no limit to user interaction; however, previous studies have used ultrasonic to control non-solid particles for other mid-air applications rather than visual display applications, for example, smells (Hasegawa et al., 2018) and haptic feedback (Carter et al., 2013). Therefore, this thesis will focus on the visual display.

The mechanical approach, as shown in Table 1.1, is straightforward (Lam et al., 2014). It requires cheap off-the-shelf mechanical hardware (e.g., stepper motors and fans) to configure the movement of the mist emitter, matching it with the projected graphical content. With this technique, the system is large in size due to the mist particle guider mechanism (e.g., fans and pipes), yet its size does not limit user interaction.

The electrostatic approach does not allow the user to reach through the display (Sahoo et al., 2015). It uses electrodes to reconfigure the trajectory of a laminar-charged mist. The mist is charged with a corona-based charger and flows between the electrodes of the electric field. It reconfigures the mist trajectory by varying voltage in the field. Despite this, the work claims to be able to increase the space between electrode plates to improve user interaction; however, this requires considerable space for the display alone.

The air modification approach includes an IR laser and dust detector (Perlin et al., 2006; Ruiz-Avila, 2016). These displays reconfigure air (e.g., humidity, temperature) at any target point in space, making the voxels visible since the air reacts to light differently compared to its surroundings. Although these techniques are capable of creating a 3D model in mid-air, the apparatus is expensive (Smalley et al., 2018a).

Table 1.1 shows that the mechanical and ultrasonic approaches have the highest number of stars, thus demonstrating practicality in comparison with the other approaches. Both have a low price point and unlimited reach-through. Therefore, this research will conduct a series of experimental investigations on interactive prototypes, focusing on these

two approaches.

Techniques	Price	Form factor	Reach-through
Ultrasonic ★★★★★	Low ★	Small ★	Unlimited ★
Mechanical ★★	Low ★	Large	Unlimited ★
Electrostatic ★	Low ★	Large	Limited
Air modification ★	High	Medium	Unlimited ★

Table 1.1: Table of the practicality of permeable mid-air display techniques.

Using three interactive prototypes, this thesis will design, implement, and evaluate reconfigurable mid-air displays that use permeable materials. Each prototype exploits a specific capability of the mid-air display. The first prototype builds a coarse-mechanically reconfigurable mid-air display called MistForm (Tokuda et al., 2017), an adaptive laminar fog screen that can deform according to human gestures. The system first tracks the user’s gesture and drives five actuators that hold a pipe of mist emitters accordingly. This prototype uses machine learning to create screen shapes and evaluate them based on reconstructing errors. It collects a set of points at the surface of the mist curtain and learns the shapes before it reconstructs them back. The system randomly shapes the screen and projects spheres onto each shape, then performs an evaluation by analysing the re-projection error (i.e., the sphere’s distance from the expected position to the actual detected position).

The second prototype, called SoundBender (Norasikin et al., 2018), uses a fine-ultrasonically reconfigurable mid-air display of a hybrid setup (a combination of a PAT and a metamaterial (MM)). This prototype creates high-fidelity sound fields (i.e., bent sound beams) through the MM and reconfigures the field with the PAT. Eventually, this enables re-configuration on the particles in mid-air because the acoustic radiation energy can act on the particles. The evaluation of the prototype is carried out using in-depth empirical analysis based on sound pressure level (SPL) using both simulation and experimental measurements. The results of the simulated sound field will be generated using COMSOL Multiphysics, while an acoustic acquisition machine will obtain the actual measurement.

Finally, the third prototype, SonicSpray (Norasikin et al., 2019), exploits the technique used by SoundBender to create a reconfigurable mid-air display in a minimal form factor. This prototype can reconfigure a laminar aerosol using only a 6 x 6 transducer ( $\phi = 10\text{mm}$ ) array. The evaluation of the prototype is carried out based on SPL simulations in

COMSOL Multiphysics and measurements of the Reynolds number (Re).

The data for the evaluation is obtained using calibrated apparatus, such as Brüel&Kjær (B&K) microphone and a PAT. Most of the equipment for this research has been built and maintained in the Interact Lab<sup>6</sup>, University of Sussex. The research approach, method, and techniques in this thesis are, to the best of my knowledge, a novel strategy to address the difficulty of reconfiguring the permeable mid-air displays.

### 1.3 Main contributions

This research suggests techniques for the reconfiguration of permeable mid-air displays with sufficient reconfigurability (coarse and fine manipulation). This is explored using experimental investigations of three interactive prototypes: MistForm, SoundBender, and SonicSpray. This thesis illustrates the use of the proposed techniques and investigates the performance of the three interactive prototypes for HCI applications.

MistForm is a collaborative work of all authors. Plasencia conceived the idea. Tokuda and the author of this thesis designed and implemented the system, gathered experimental data analysed them, and demonstrated the concept. All the authors contributed to the discussion and edited the published manuscript (Tokuda et al., 2017). The author of this thesis conceived the idea for SoundBender (Norasikin et al., 2018) and SonicSpray (Norasikin et al., 2019), designed and implemented the systems, gathered experimental data, demonstrating the concept, and analysed the data.

### 1.4 Thesis structure

This section briefly explains how the chapters of the thesis will proceed. Firstly, this thesis presents three interactive reconfigurable mid-air display prototypes in three separate chapters – MistForm in Chapter 2, SoundBender in Chapter 3 and SonicSpray in Chapter 4. Table 1.2 summarises the features and limitation of the three prototypes. MistForm can coarsely reconfigure permeable matter (i.e., mist) as visual displays. It uses a mechanical approach to reconfigure the matter in the air. However, it costs a large form factor.

In contrast, SoundBender demonstrates smaller form factor compared to MistForm. It reconfigures the matter through ultrasonics approach. It can finely reconfigure matter in the air (i.e., air particles, fog, polystyrene beads) and offers beyond visual displays (e.g.,

---

<sup>6</sup>Interact Lab website <http://www.interact-lab.com/>

haptic display). To demonstrate the insight of the technique in SoundBender, particularly for reconfigurable visual displays, and to improve the form factor in both MistForm and SoundBender, SonicSpray describes a visual display system that uses a similar technique but with a different sound field from SoundBender. In addition, it features a smaller version of display than in SoundBender. This thesis then closes with a conclusion chapter (Chapter 5).

Prototypes	Approach	Reconfigurability	Form Factor
MistForm (Tokuda et al., 2017)	Mechanical	Coarse	Large
SoundBender (Norasikin et al., 2018)	Ultrasonics	Fine	Small
SonicSpray (Norasikin et al., 2019)	Ultrasonics	Fine	Smaller

Table 1.2: Table of the proposed prototypes, its features and limitations.

#### 1.4.1 Chapter 2, MistForm: Adaptive shape-changing fog screens

This chapter<sup>7</sup> describes an investigation of an interactive prototype, MistForm. It is capable of reconfiguring the permeable mid-air display of a laminar mist curtain at a coarse level of control. MistForm can support one or two users, interacting with either 2D or 3D content. MistForm combines affordances from both shape-changing interfaces and mid-air displays. For example, a curved display can maintain content within a comfortable reach for a single user, while a convex shape can support several users engaged in individual tasks. MistForm also enables unique interaction possibilities by exploiting the synergies between shape-changing interfaces and mid-air fog displays. For instance, moving the screen will affect the brightness and focus of the screen at specific locations around the display, creating spaces with similar (collaboration) or different visibility (personalised content).

<sup>7</sup>This chapter was published in Proceedings CHI ‘17, Proceedings of the 2017 CHI Conference on Human Factors in Computing Systems, pp. 4383–4395 (<http://doi.acm.org/10.1145/3025453.3025608>)



This chapter describes the design of the MistForm and analyses its inherent challenges, including image distortion and uneven brightness on dynamically curved surfaces. This chapter also provides a machine-learning approach to characterise the shape of the screen and a rendering algorithm to remove aberrations. It also describes the novel interactive possibilities that reflects MistForms’s potential and limitations. Although this prototype provides sufficient reconfigurability, the two critical limitations – bulk and noise – pave the way for the study of a second interactive prototype, SoundBender, as described in Chapter 3.

#### 1.4.2 Chapter 3, SoundBender: Dynamic acoustic control behind obstacles

This chapter presents a preliminary study<sup>8</sup> and a final study<sup>9</sup> of the reconfiguration technique for the ultrasonic approach to permeable displays in free air. The popularity of the ultrasonic approach is growing (particularly in the HCI community) for various applications, for example, in haptics, on-body interaction, and levitation-based displays. The reason for this is that the sound field can be controlled precisely using a minimal and versatile PAT. However, these techniques share a critical limitation: the physical size of the transducers limits the fidelity of the sound fields that can be produced.

This chapter provides a solution to this limitation using a hybrid-technique prototype, the SoundBender, which combines a PAT and an acoustic MM, a high fidelity sound manipulator. The hybrid prototype reconfigures the fine sound field, created by MM, through the versatile PAT. This chapter explains the approach to the design and implementation of such a hybrid prototype (i.e., to create complex sound fields), as well as methods to manipulate the field dynamically (i.e., to stretch or steer it). This chapter also demonstrates the innovative applications enabled by this prototype, such as levitation, tactile feedback and control of permeable matter around and beyond obstacles. However, this chapter does not study the minimal form factor device – a critical limitation when reconfiguring laminar permeable displays. Therefore, Chapter 4 describes a study to address this particular issue.

---

<sup>8</sup>The preliminary study in this chapter was presented in the 24<sup>th</sup> International Congress on Sound and Vibration ICSV24.

<sup>9</sup>The final study was published in Proceedings UIST ‘18, Proceedings of the 31<sup>st</sup> Annual ACM Symposium on User Interface Software and Technology, pp.247–259 (<http://doi.acm.org/10.1145/3242587.3242590>)

### 1.4.3 Chapter 4, SonicSpray: A tool for reconfiguring permeable mid-air displays

There are two significant issues concerning the reconfiguration of permeable mid-air displays: (1) the size of the system that increases as its complexity increases, and (2) the ability to retain the laminar flow of the mid-air display. These two issues place serious limitation on the practicality and commercial success of such systems.

This chapter<sup>10</sup> addresses the two issues by introducing a new, minimal form factor technique, namely SonicSpray, which combines ultrasound field computation and a projection mapping algorithm. The technique can precisely modify laminar mist for mid-air displays in the real world. This chapter proposes and justifies the design and describes the implementation steps to build the display. It verifies and evaluates the performance of the reconfiguration and projection algorithm. It demonstrates a working prototype to finely reconfigure a laminar mist using only a 6 x 6 ultrasound transducer array (for each transducer,  $\phi = 10\text{mm}$ ). This chapter also explores various useful applications in HCI (e.g., applications for learning, entertainment and the arts).

### 1.4.4 Chapter 5, Conclusion and future work

This chapter concludes the process and suggests techniques that sufficiently reconfigure permeable mid-air displays based on the study of the interactive prototypes. It also includes a number of strategies to coordinate the capabilities of the three prototypes and their prospective improvements for future HCI applications. This chapter also suggests studies that can be expanded upon by the HCI community.

---

<sup>10</sup>This chapter was published in Proceedings of ISS '19, Proceeding of the 2019 ACM International Conference on Interactive Surfaces and Spaces, pp. 113–122 (<https://doi.org/10.1145/3343055.3359704>)

## Chapter 2

# MistForm: Adaptive shape-changing fog screens

### 2.1 Introduction

In this chapter<sup>1</sup>, Plasencia conceived the idea, Tokuda and the thesis author designed and implemented the system, gathered experimental data and analysed them, and demonstrated the concept. The thesis author discussed and edited the published manuscript of this chapter (Tokuda et al., 2017) with all the authors.

This chapter provides a solution to the difficulty of reconfiguring permeable mid-air displays by coarsely changing the shape of a fog screen. The MistForm, features a fog display surface and a mechanical actuation approach to the fog manifold, which allows the displacement of a continuous fog surface in a range of 18 cm. MistForm retains the affordances of both shape-changing interfaces (i.e., changing the position of each point of the display) and permeable screens (i.e., reach-through capabilities and directional light-scattering). For instance, a concave shape (Figure 2.1 (A)) can cover a single or multiple user’s view. It optimises the concavity to allow comfortable hand reach and allows for interaction both in front of and behind the display (i.e., through the fog).

The interplay between shape-changing and permeable affordances enables unique 2D and 3D interaction capabilities. First, moving parts of the fog display will change the angle between the observer and the light projected. This change is useful to attenuate common issues associated with fog displays, such as uneven brightness and blending of

---

<sup>1</sup>This chapter was published in Proceedings CHI ‘17, Proceedings of the 2017 CHI Conference on Human Factors in Computing Systems, pp.4383–4395 (<http://doi.acm.org/10.1145/3025453.3025608>).



Figure 2.1: (A) MistForm is a shape-changing fog screen, enabling single-user and dual-user interactions; (B) with 2D or 3D content; (C) a computational approach and projection algorithm work together to minimise artefacts including shape distortion and uneven brightness, related to projecting onto a shape-changing fog display (note the parallel edges and brightness in the checkerboard).

neighbouring pixels. Second, MistForm can transform these issues into reconfigurable features. It uses the shape that produces uneven brightness and blending as regions of optimum visibility (for example, shared or disjoint regions, where each user can see one region clearly while the others are dim and blurred as in Figure 2.1 (B)). Finally, it can adjust the shape to ensure the fog surface stays within the depth of field of the user's eyes. This capability establishes MistForm as the first display with an adjustable zone of comfort (Shibata et al., 2011), allowing direct hand interaction with 3D content in much larger volumes than typical planar 3D displays.

The first part of this chapter focuses on addressing the engineering challenges related to fog screen reconfigurations that make an adaptive shape-changing screen of permeable material. This includes the design of the display, the identification of the challenges related to projecting onto such screens, the formulation of the problem, and a technique that is scalable for larger display sizes and higher shape resolution (i.e., more actuators). This chapter uses a data-driven technique based on the input of their linear actuators to estimate the 3D shape of the fog screen. Finally, it contributes a projection algorithm to correct image distortion (see Figure 2.1 (C)). This is done by taking the shape and fog brightness profile into account, together with other relevant factors such as projector properties and the user's location. It evaluates the reduction in distortion of the prototype and reports the results achieved.

The second part of this chapter presents an exploration of the various interaction possibilities and demonstrates key scenarios enabled by the MistForm. The focus is specifically on exploiting the interplay between shape changing and permeable displays (i.e.,

fog screens). The chapter concludes with a discussion on the future possibilities and limitations of this type of system.

## 2.2 Related work

MistForm explores the synergies and engineering problems of the shape-change reconfiguration technique in mid-air displays. This section reviews previous studies in these fields.

### 2.2.1 Shape changing displays

Visions such as Kinetic Interactions ([Parkes et al., 2008](#)), Organic User Interfaces ([Coelho and Zigelbaum, 2011](#)) or Radical Atoms ([Ishii et al., 2012](#)) have fueled research on shape-changing interfaces in HCI. When focusing on display systems, FEELEX ([Iwata et al., 2001](#)) as in Figure 2.2 was one of the first to feature the concept of shape-change through reconfigurable bits of the display surface, using the technique of computer-controlled mechanical actuators. It uses an array of linear mechanical actuators together with pre-rendered image projections to reconfigure the display surface. The actuators move in the z-axis direction (up-down) to activate the surface. The surface has a maximum size of 24 cm x 24 cm (namely FEELEX 1), and a minimum of 5 cm x 5 cm (namely FEELEX 2). Other systems have adapted this reconfiguration technique, resulting in a shape-change display of different sizes and formats; Lumen ([Poupyrev et al., 2004](#)), for instance, has a similar size to FEELEX 1. It is capable of sensing human touch using a combination of electromechanical and capacitive sensing mechanisms. The display uses a shape memory alloy (SMA) for its mechanical actuators. The SMA can contract when the temperature rises, and expands to its initial state when the temperature drops down. The display uses a simple mesh of copper to perform basic capacitive coupling, a process that transfers energy between distant electrical networks. The display system detects changes in the energy transfer rate and uses this information to change the surface bits accordingly.

InFORM ([Follmer et al., 2013](#)) extends the computer-controlled mechanical actuators technique by integrating it with a tracking system and light projection, allowing both users and objects to interact with the reconfigurable display surface, in real-time. For example, it demonstrates an application of 3D model manipulation whereby it renders a physical representation of the 3D model, and users can move a token in a specific direction to browse different 3D models, as well as to transform, translate, scale and paint a selected

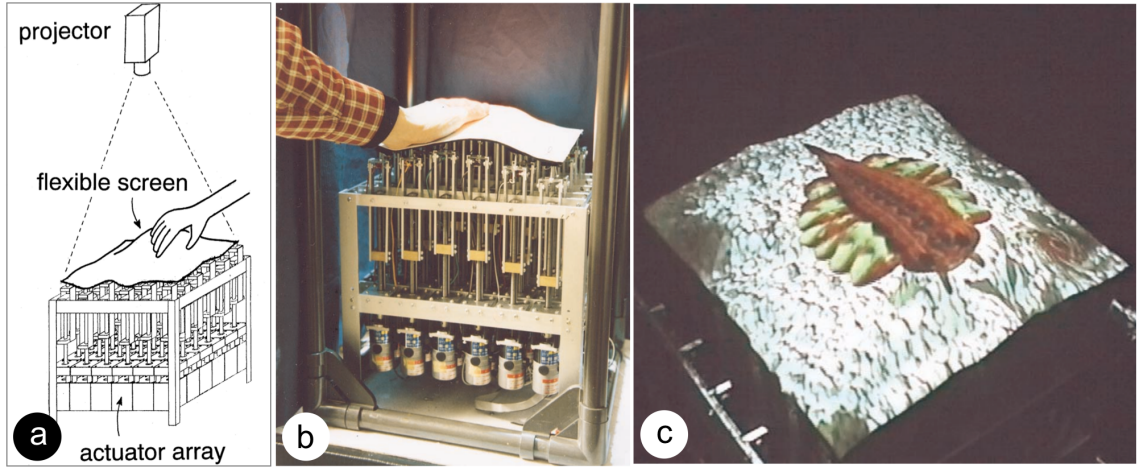


Figure 2.2: An example of mechanically controlled displays (Iwata et al., 2001).

model. The surface of the interactive display is large, covering a surface area of up to  $38.1 \text{ cm}^2$ , and comprises an array of polystyrene pins array linked to computer-controlled actuators, where each pin has a  $9.5 \text{ cm}^2$  surface area.

ShapeClip (Hardy et al., 2015) adapts the technique but as a modular shape-change display, making it portable and scalable. A single unit of this display comprises two light resistors and a stepper motor, resulting in a  $2 \text{ cm} \times 2 \text{ cm}$  screen size. The unit converts a sampled pixel brightness from the light resistor into control signals, and changes its height accordingly. The ShapeClip reports a display at a various surface sizes, for example, a display with array units of  $4 \times 4$  and  $8 \times 2$ .

Surflex (Coelho et al., 2008) uses the same technique of computationally controlling mechanical actuators for a different shape-change display format. The display embeds SMA in a foam, similar to that used in Lumen (Poupyrev et al., 2004), and reconfigures the foam surface by electronically controlling the SMA coil temperature. This is done through an  $8 \times 8$  array of SMA coils (i.e., each pixel has two horizontal and vertical coils). Surflex can produce an unlimited number of surface deformations. Roudaut et al. (2013) explored the technique using six actuation strategies of dielectric electro active polymers and SMA and described the shape resolution based on ten quantifiable features: area, granularity, porosity, curvature, amplitude, zero-crossing, closure, stretchability, strength and speed.

Rather than using mechanical actuators to reconfigure a display, Actuated Workbench (Pangaro et al., 2002) and BubbleWrap (Bau et al., 2009) use electromagnetic actuators arranged in an array. Both display systems reconfigure their display surfaces by manipulating magnetic fields through pulse-width modulation (PWM). Both use an electromagnet

to force surface objects to any target position. Actuated Workbench is capable of tracking objects that have IR LED using a camera with an IR filter. This can provide visual feedback through a light projector on its  $16.5 \text{ cm}^2$  display surface. By doing so, the display system can synchronise the 2D graphical projection with its surface physical state, making it as a shape-change physical user interface. BubbleWrap, which is the size of the palm of the hand, encloses its reconfigurable cells in fabric. Its reconfigurable surface expands and contracts the cells up to a height of 15 mm. It has the potential to be used as a textile-based haptic display.

[Takashima et al. \(2016\)](#) built a large shape changing display from reconfigurable flat panels that are mounted on Roomba robots. The display consists of three screen panels (each panel is 61 cm x 150 cm in size), a motion tracking system and a light projector. The system first detects a specific motion of the user and translate this into reconfiguration signals for the panels. It reconfigures the panels into a concave shape for private use, and it expands the panels for individual use. [Coelho and Zigelbaum \(2011\)](#) and [Rasmussen et al. \(2012\)](#) explored these shape-changing designs and their practical techniques. However, most previous studies investigate on shape-changing or reconfigurable displays focus on solid display elements, and only a few describe permeable systems in mid-air. Introducing reach-through features (i.e., the use of permeable material) into shape-change displays opens up new areas of exploration for practical display design in the future (by reducing storage space, for example, or by making use of a reconfigurable non-rigid display).

## 2.2.2 Permeable mid-air displays

Permeability is a feature of displays that form an image on a plane in space, avoiding accommodation conflicts within the proximities of that plane (i.e., in front and behind) and enabling reach-through interactions. Permeable mid-air displays are available in the three different concepts that have been explained briefly in Chapter 1 (and as illustrated in Figure 1.4): light converging, light diverging, and light scattering concepts.

### 2.2.2.1 Light converging optic

Light-converging optical elements (i.e., optical combiners, concave mirrors, convex and Fresnel lenses) have been often been used to create a mid-air images by presenting a stigmatic pair of points of the image at symmetrical positions in relation to the optical elements ([Bimber, 2004](#)). Approaches using optical combiners (e.g., half-silvered mirrors or a beam splitter) between the user and the image ([Poston and Serra, 1994](#); [Hachet et al.,](#)



2011; Hilliges et al., 2012; Lee et al., 2013; Martinez Plasencia et al., 2014a) hinder reachability and interaction. For example, SpaceTop (Lee et al., 2013) and HoloDesk (Hilliges et al., 2012) render 3D objects in mid-air; however, the user needs to see the content through the half-silvered mirror. While looking at the objects through the mirror, both systems incorporate a tracking system, allowing interaction to occur behind the mirror. Half-silvered mirrors (i.e., a beam splitter), which can be found in criminal interrogations rooms, reflects half of the incident light rays and permit the other half through the surface. The mirror produces a floating object after the light rays of the display screen have been transmitted have converged as a reimaged object.

Retroreflective imaging (Yamamoto et al., 2014; Tokuda et al., 2015) removes the barrier (i.e., the mirror), and allows for reachable floating images in-front of the user. This is done by combining off-the-shelf beam splitters and retro-reflectors. Retroreflective material is widely used for traffic signs; it reflects light backwards towards the incident light (in car headlights, for example) and the material is easy to install since it has no problem with alignment. To create floating images, a beam splitter first needs to reflect light rays from the source towards retroreflective material. Then, the light rays will reflect on the beam splitter and the beam splitter will transmit the rays through it to form mirror images in mid-air.

HaptoMime (Monnai et al., 2014) uses an aerial imaging plate (AIP), providing similar affordances to retroreflective imaging. The AIP comprises only a plate, but with optical properties that allow incident light to reflect twice inside it. The reflected light rays converge at a location that is symmetrical to the AIP. The AIP does not have a fixed focal length; therefore, the distance from the source to the AIP will be the same as the distance from the AIP to the converged point.

Vermeer (Butler et al., 2011) uses a swept volume 3D display at the focal point of a concave mirror and forms the volumetric 3D content in a small area above the mirror. This occurs when two parabolic mirrors, equal in size, are placed opposite to each other, resembling a ‘clamshell’ setup (i.e., their focal points are opposed to each other). If there is a large hole at the top of the upper shell, then any object that is placed inside the lower shell will reimage, as if the object is floating just above the hole. Due to the parabolic properties of the mirrors, the light rays converge just above the hole of the upper mirror.

Despite techniques in the light converging concept are effective at presenting a floating image, real objects (e.g., fingers) occlude the light-converging elements and the real objects always appear in front of the floating image, causing incorrect occlusions and eye fatigue.



### 2.2.2.2 Diverging light

This concept provides techniques that focus pulsed laser energy at a specific point in the air, releasing photons from ionised molecules at that point (i.e., plasma emission). Therefore, the point emits light and can be co-located with actual image points to form a mid-air image. The plasma emission uses a short pulse duration that lasts for nanoseconds or less; for instance, [Kimura et al. \(2006\)](#) created a mid-air image with voxels from a nanosecond-pulsed laser, which generated 100 voxels per second. [Kimura et al. \(2011\)](#) later improved the technique and created an even greater number of voxels: 300 per second. [Saito et al. \(2008\)](#) used a shorter pulsed laser (100 fs), and create a greater number of voxels: 1000 voxels per second. The technique provides sufficient voxels per second for a practical mid-air display (no flickering effects occur, as if the voxels are simultaneously drawn). However, displays in the light diverging concept do not allow a user to interact with the generated plasma. [Ochiai et al. \(2016b\)](#) proposed a mid-air display with a femtosecond-pulsed laser (between 100 fs and 269 fs), which allows users to touch the generated plasma. The display can generate up to 1,000 voxels (using a 100 fs pulse) and 200,000 voxels (using a 269 fs pulse). A higher number of voxels can create an image with a better resolution of an image in the air. Although the user can touch the image, the plasma energy is still a main concern because it can cause damage to the user eye and skin. This concern makes the display less suitable for user interaction.

### 2.2.2.3 Light scattering particles

Several relevant studies explore the reconfiguration of displays within the light-scattering concept. One such study is that of [Sahoo et al. \(2015\)](#), which constrained a charged fog screen between transparent electrodes. The system then reconfigured the trajectory of the fog by modulating the voltage. However, the electrodes in the prototype hindered user interaction. This problem does not occur in a prototype by [Lam et al. \(2014\)](#). The authors describe a 2D array of a small and flat fog emitters, which can create small fog displays at discrete positions across a table top. However, the affordance of screen continuity can only be ensured across display elements when the emitters are switched on in the same line.

A second approach by [Lam et al. \(2015a\)](#) mounted fog emitters on moving guides, allowing for continuous displacement, but not for continuity across the display. Thus content must be kept small (within the limits of one emitter). To create a mid-air display that can reconfigure and change its shape, as well as offer interesting capabilities, the

light-scattering performs favourably compared to the other two concepts: it is safer and has no issue with incorrect occlusion, which makes it the best option.

This light-scattering concept also functions with different scattering mediums, for example, waterdrop particles (Eitoku et al., 2009; Barnum et al., 2010), fog particles (Kataoka and Kasahara, 1993; Rakkolainen, 2008b; Martinez Plasencia et al., 2014b) and airborne particles (Perlin et al., 2006; Schneegass et al., 2014). The light-scattering patterns of these mediums depend on the size and shape of the particles. Most relevant to this research is, Mie scattering (i.e., from spherical particles whose diameter is around or larger than the wavelength of incident lights, such as in a fog screen), which diffuses light directionally towards the projection axis. However, this effect produces uneven brightness on the images (i.e., very bright when looking straight at the projector, and decaying to the sides as the angle increases). This issue has been reported (Rakkolainen, 2008a) and corrected in subsequent studies (Martinez Plasencia et al., 2014b); however, this directional scattering can also offer interesting affordances, such as creating face-to-face (Olwal et al., 2007) or multi-view displays (Yagi et al., 2011). This chapter exploits the affordances of this concept, focusing on the interplay of the changes in the display’s shape, which remain unexplored.

## 2.3 MistForm: Shape changing fog screen

MistForm creates a continuous and permeable display surface of 84 cm x 56 cm, which can be moved forwards and backwards up to 18 cm, enabling a range of shapes to be created. Mistform’s working volume is designed to cover the space for direct 3D interaction that an average (or shorter) adult user can reach, as detailed later in this chapter. It can also be used to support collaborative interaction for two users in front of the display.

The design of MistForm is an adapted version of that proposed by Kataoka and Kasahara (1993), using a laminar flow of fog constrained by curtains of air to avoid turbulence and maintain the consistency of the display surface. It follows the guidelines proposed by Martinez Plasencia et al. (2014b) (i.e., the projector above the display with the fog flowing down) as the interactive scenarios for reach-through interactions. It uses a long-throw projector, placed at 2 m from the display. reasons for this are that, first, it minimises the angle between the projector rays and the observer in front of the display, which allows a better use of the directional light scattering provided by the fog screen, as smaller angles provide higher brightness. Second, a longer throw allows projected content to remain in

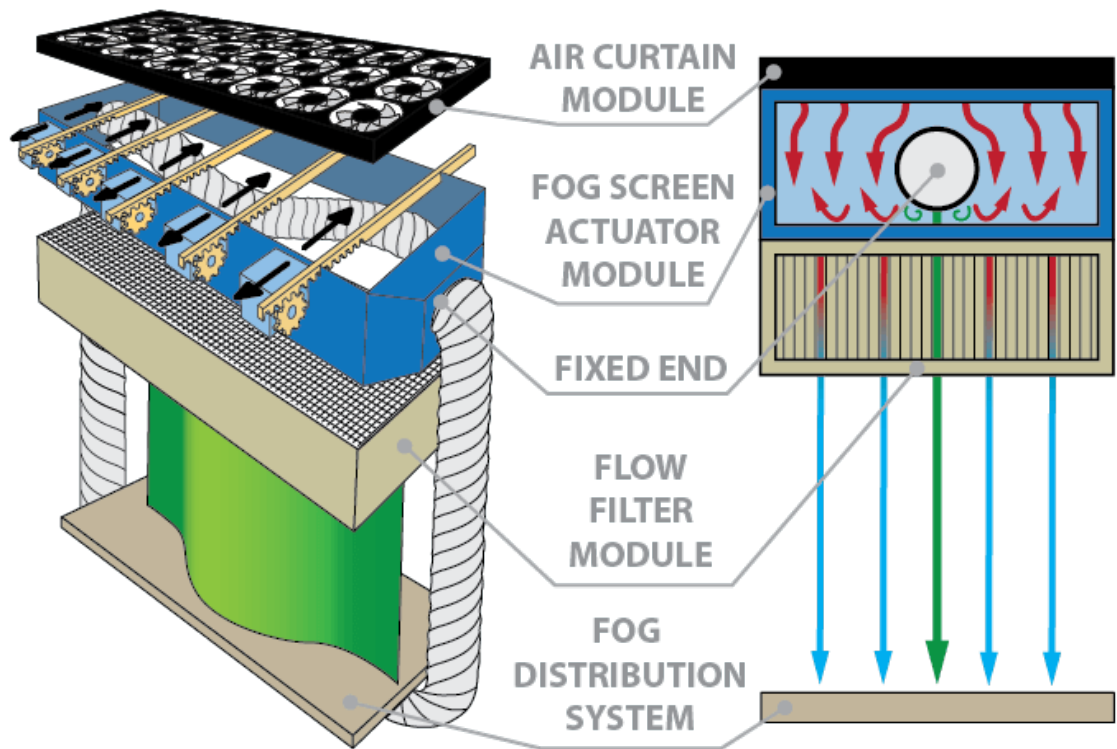


Figure 2.3: An overview of the main elements in MistForm. The actuator module uses a PVC flexible pipe (10 cm diameter) and an array of five linear actuators. A fan array creates the airflow around the pipe and into the filter module, to create a shape changing fog display with a working volume of W:84 cm x D:18 cm x H:59 cm.

focus within the 18 cm depth of the fog screen’s range of motion.

The main difference to previous approaches is that MistForm includes a flexible fog manifold and five linear actuators, displacing the manifold within a range of 18 cm, to enable the shape changing fog surface. This moving manifold requires an additional display space of 9 cm to each side in order to protect the working space with an additional laminar flow of air.

It uses an off-the-shelf 3D projector and shutter glasses, to display stereo content, Kinect v1 for hand tracking and interaction (i.e., its laser projector works even through the fog) and OptiTrack for head tracking and perspective corrected rendering.

### 2.3.1 Modular design

Figure 2.3 shows the modules of the MistForm in detail: the air curtain module, the manifold actuator module and the flow filter module. The air curtain module consists of a 7 x 3 array of 12 cm ARX DC ceramic bearing fans ( $291.6\text{m}^3/\text{h}$ ), covering the entire display area (84 cm x 36 cm). This module blows air around the flexible pipe and into the flow filter module, to produce a laminar flow of fog.

The screen actuator module consists of five 12 V stepper motors and a  $\varnothing$  100 mm flexible PVC ducting pipe. There is an array of  $\varnothing$  2 mm holes of array at the bottom of the flexible pipe that is placed on top of the flow filter module. The pipe is fixed at both ends and is transversely actuated by five stepper motors by linear motion shafts. This allows a displacement of 18 cm at a maximum speed of 40 cm/s. Mechanical switches at the ends of the shafts’ range (home positions) initialise them and correct drift during operation.

The fog distribution system delivers fog to the flexible manifold, using a fog machine and a 12 cm DC circulation fan. The fog distribution system controls the fog density and velocity, and influences pipe flexibility (i.e., air pressure changes the stiffness of the fog pipe).

The flow filter module consists of multiple layers of  $\varnothing$  6 mm vertical fluted plastic. This fluted array filters the wake turbulence created when the flow from the air curtain module blows around the circular pipe, creating a laminar air curtain around the fog screen. This combination of modules results in a dynamic fog screen moving inside a volume of W:84 cm x D:18 cm x H:59 cm, and the arrangement allows for 3D content to be projected without vergence-accomodation conflict (Hoffman et al., 2008) within MistForm’s working volume, as detailed in the exploration of interaction possibilities.

### 2.3.2 Challenges and general approach

MistForm offers interesting affordances, such as maintaining the display surface within an ergonomic reach for the user, better support for freehand 3D interaction or support for 3D multi-user scenarios using proxemics cues. However, projection onto dynamic curved surfaces inherently introduces distortion in the shape of the content. This, in conjunction with the uneven brightness distribution typical in fog screens (i.e., Mie scattering) can seriously hinder its use.

This chapter suggests a projection algorithm to overcome these limitations. The algorithm computes the content as it should be seen from the user’s eye position. Then, for each pixel projected onto the curved display surface, the algorithm determines the colour that should be mapped to that pixel using the 3D position of the point on the screen and the location of the user’s eyes. Although a full description of the algorithm is provided later in this chapter, the explanation above helps to illustrate how the algorithm requires accurate registration of all user’s eyes, of the projector and of the 3D shape of the display itself. While the first two are common considerations in virtual reality (VR) and projection mapping systems, the real-time characterisation of the display shape remains a specific challenge and this chapter addresses this challenge in the study of following section.

## 2.4 Shape reconstruction

This section provides a more detailed description of the reconstruction technique to aid replication by other researchers.

### 2.4.1 Modelling of pipe shapes

The deformation of the MistForm’s fog screen is driven by the displacements of five actuators and the two fixed ends of the display. The choice of stepper motor allows for reconfiguration of the display position, as long as the actuator speed and torque limits are met.

$$x_i = \frac{s_i}{S} \cdot T \cdot P \quad (2.1)$$

According to these criteria, it should be possible to create a direct mapping between the number of steps taken from the homing position ( $s$ ), steps per revolution ( $S=200$ ), number of teeth in the gear ( $T=11$ ) and the pitch of the raft ( $P=1.9$  cm), and the location

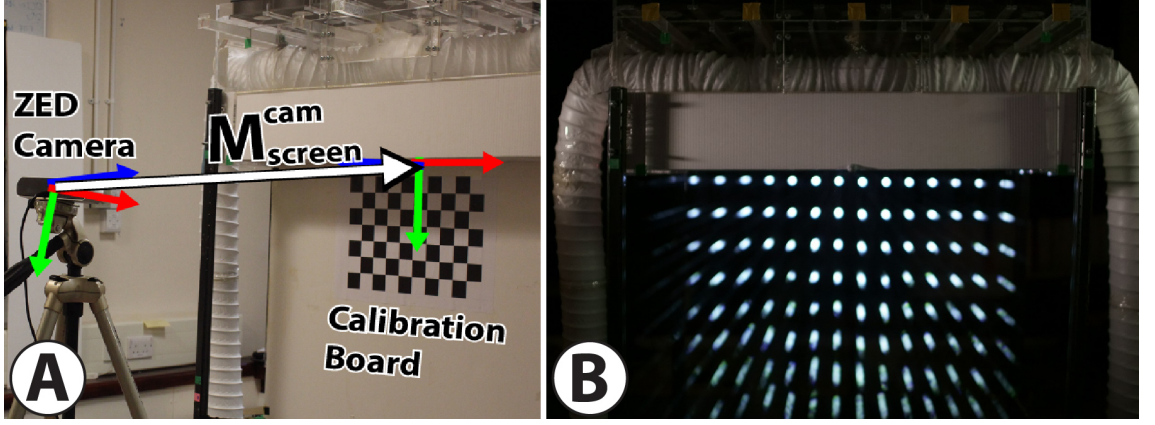


Figure 2.4: Sampling ground truth data: MistForm projects an array of  $15 \times 8$  points on the display and uses a calibrated stereo camera (i.e., intrinsics and extrinsics) to retrieve 1,023 samples.

$(x_i)$  of the servos, as shown in Equation 2.1. These five inputs are defined as a vector  $\bar{x} \in \mathbb{R}^5$ . The main goal is to estimate the 3D position  $v$  of each point of the display surface, given a specific input vector  $\bar{x}$ . To retrieve these, a sparse set of  $15 \times 8$  points is projected in even distribution across the display volume.

This study uses a data-driven technique, formulating the goal as the computation of the position of these projected points,  $V = \{v_1, \dots, v_{RC}\} \subseteq \mathbb{R}^4$ , where  $R = 8$ ,  $C = 15$  and  $N = R.C$ . Later on, spline fitting will allow an interpolation of intermediate 3D points.

This study will make use of homogeneous coordinates (i.e., 3D points as  $V = v_i(x, y, z, 1) \in \mathbb{R}^4$ ), homogeneous  $4 \times 4$  matrices and right hand systems of reference. This will ease the explanation of the projection algorithm. For some explanations, this study will vectorise  $V_c = \{v_n^c\}_{n=1}^N$  into a column vector  $V \in \mathbb{R}^4N$ , representing the sparse shape to compute for a given  $\bar{x} \in \mathbb{R}^5$  (i.e., display state). To describe a set  $C$  of these variables, this study will label them as  $V_c = \{v_n^c\}_{n=1}^N$ ,  $V_c$  and  $\bar{x}$ , with  $c \in C$ .

## 2.4.2 Ground truth capture

This study uses a data-driven technique to reconstruct the display shape, correlate the display state to screen shape, and validate the correctness of the proposed model.

### 2.4.2.1 Preparing for data acquisition

A stereoscopic camera (Stereo Labs ZED) was used to capture 25 images of a checkerboard of a known size ( $10 \times 7$  tiles, 2.4 cm side) at different positions and orientations in front of

the camera. A technique discovered by Zhang (2000) was used to retrieve each camera's intrinsic and distortion parameters and their positions relative to the checkerboard in each image. To compute the relative position from one camera to another, this study used the *Levenberg–Marquardt* optimisation method (Marquardt, 1963). A checkerboard was placed at a known position, to retrieve the position of the camera pair relative to MistForm (see  $M_{screen}^{cam}$  in Figure 2.4 (A)).

#### 2.4.2.2 Dataset construction

Using the projection of the static pattern of 15 x 8 points (see Figure 2.4 (B)), the setup above allowed for stereo triangulation to detect the 3D coordinates  $w_i(x, y, z, 1) \in \mathbb{R}^4$ , relative to the stereo camera. Points were then transformed to MistForm's space using the camera extrinsics as  $v_i = M_{screen}^{cam} \cdot w_i$ .

This study collected data from  $J=1,023$  random shapes, recording the actuator's input ( $\bar{x}$ ) and three samples of 15 x 8 projected points, and created the ground truth  $V$  as the average of these three samples, creating a fixed dataset  $D = \{\{\bar{x}_j, V_j\}_{j=1}^J\}$ , which were later will be used for training (subset  $M$ , with 800 samples) and evaluation (subset  $E$  with 223 samples) to assess the quality of the proposed model.

#### 2.4.3 Data-driven shape reconstruction

##### 2.4.3.1 Regularised least square linear regression model

To predict shape  $V$  from the five actuators' input  $\bar{x}$ , this study used a linear regression model:  $V = \bar{x}^T W$  where  $W \in \mathbb{R}^{5 \times N}$ .

The five actuators move linearly along the  $Z$ -axis. The projected pattern (15 horizontal dots) assures that at least three or four points fall between any two actuators, giving enough resolution to reconstruct the shape of the pipe between the two actuators. Very little variation is expected along the  $Y$ -axis, as the laminar filter module creates a thin straight layer of fog flowing downwards. Therefore, this study can reasonably assume the linear relationship between  $V$  and actuator's input  $\bar{x}$ .

Let  $X = [\bar{x}_1, \dots, \bar{x}_M^T] \in \mathbb{R}^{M \times 5}$  and  $Y = [V_1^T, \dots, V_M^T] \in \mathbb{R}^{M \times 4N}$ . Applying the regularised least square method, the optimised value of  $W$  can be calculated as follows:

$$W^* = \operatorname{argmin}_W \|Y - XW\|_2^2 + \lambda \|W\|^2 \quad (2.2)$$

where  $W \in \mathbb{R}^{5 \times 4N}$  is the linear regression weight matrix and  $\lambda$  is a regularisation



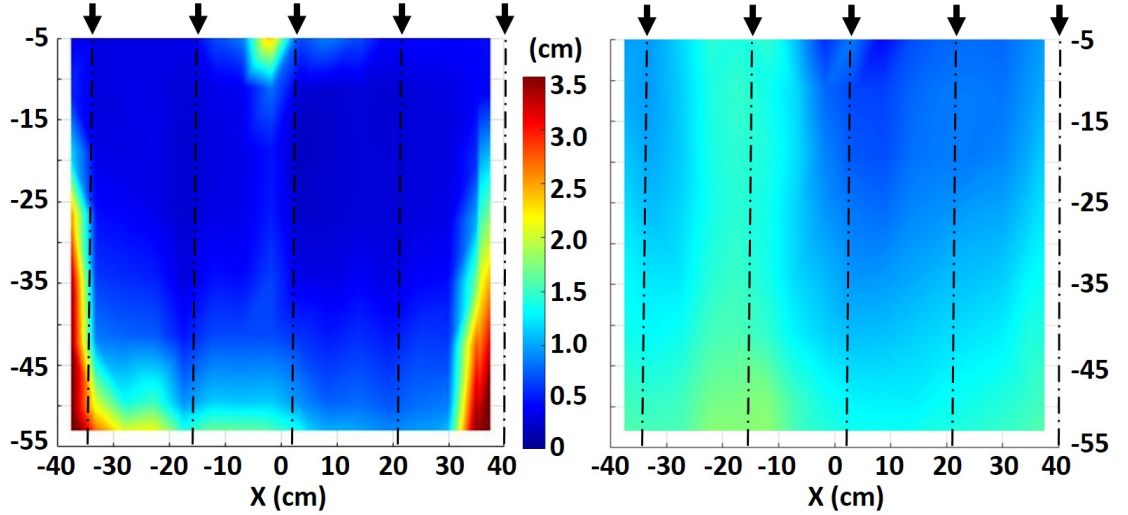


Figure 2.5: Estimation of the turbulence across the display (left) and reconstruction error from the proposed regression model (right). Black arrows indicate step motor  $X$  positions.

parameter to penalise large, complex  $W$  values. The solution has the following closed form, where  $I \in \mathbb{R}^{5 \times 5}$  is the identity matrix:

$$W^* = (X^T X + \lambda I)^{-1} X^T Y \quad (2.3)$$

To account for missing data in set  $M$ , this study relied on the assumption that points remain constant across  $Y$  (i.e., fog flows downwards). Thus, this study assigned missing  $Y$  values to the average  $Y$  value of the corresponding row, and missing  $X$  and  $Z$  values to the average  $X$  and  $Z$  values of the column. After the imputation process, this study used the complete training data matrix to solve Equation 2.3, producing a matrix  $W$ .

Matrix  $W$  allows for position estimation to a sparse set of 15 x 8 points on the fog screen at run time. The continuous shape (intermediate points) is interpolated using cubic splines. For this study, 800 shapes of training data were robust enough to consider drift effects (i.e., missed steps) for moderate periods of time; however, mechanical switches were still required to reset the position when the actuators reached the end of their range.

#### 2.4.3.2 Shape reconstruction evaluation

This study used set  $E$  (223 shapes) to evaluate MistForm's shape reconstruction model. This section reports the accuracy that has been achieved and analyses the causes of error by visualising the error distribution on the fog screen at the  $XY$ -plane.

To gain insight into the error introduced by the turbulence of the fog itself, independ-



ently of the shape, this study first measured the deviation between the three measurements that were taken from each point, for each given shape. For a fixed point, this study averaged its deviation across all of the different shapes, to provide an estimate of the flow turbulence at that point. Figure 2.5 (left) shows the application of this process at all points across the display (i.e., display turbulence). The average deviation across all points is 0.94 cm, with a minimum deviation of 0.21 cm to the top of the display and up to 3.8 cm to the bottom right. The five black arrows mark the  $X$  positions of the actuators, to evaluate their effects.

Higher error patterns can be observed at the left and right sides caused by: a) friction between the moving laminar flow (both the fog and protective air) and the outer non-moving air; b) blending between neighbouring pixels (Rakkolainen, 2008a), which makes measurements less accurate. High error values are also present at the bottom of the fog screen, as a result of flow becoming more turbulent (and non-linear) as it travels away from the flow filter module. It is worth noting that, while the top of the display shows less turbulence (i.e., smaller deviation), there is a point of high error in the top centre position. This position matches the location of the projector through the display, and this study suggests that the bright spot around the projector could make the detection of projected points around that area less reliable.

Figure 2.5 (right) shows the average error from the proposed regression model across the display. The global average error of the model is 1.2 cm, with a maximum error of 1.84 cm to the bottom of the display around  $X = -20$  cm. A minimum error of 0.41 cm is located around the top centre. This study found that this average error to be acceptable, as it lies in the order of magnitude of the inherent turbulence (0.94 cm) and the thickness of the fog screen ( $\sim 2.0$  cm).

The error is also more evenly distributed than in the previous configuration; however, it still shows the same tendencies as observed in Figure 2.5 (left), showing higher values at the bottom and both sides of the fog screen. The transition from laminar to turbulent flow is more noticeable below  $Y = -45$  cm, again leading to higher errors in the shape estimation.

There are unexpected high error bands around  $X = -20$  cm (between the first and second stepper motors), not observed in Figure 2.5 (left), indicating a lower predictability at that part of the pipe. After a post-hoc investigation of the pipe and the step motors' connections, this study found that the length of the flexible pipe between these stepper motors was slightly longer than other sections, which resulted in a more flexible (and less

predictable) part of the display.

#### 2.4.3.3 Shape control: From intended shape to actuators' input

The proposed regression model enables computation of the resulting display shape, given the actuators' input. However, in most situations (as exemplified later in this thesis), a reverse process is needed: to compute what the input must be in order to produce a desired shape.

Unfortunately, the proposed model does not support inverse regression (i.e., not invertible matrix). The model implemented a simple gradient descent method, which, when given a set of input points, finds the actuator's input that results in a shape minimising error (i.e., sum of the squares of the distances). Equation 2.1 is used to produce the first estimation for an actuator's position and the resulting shape, which has been refined iteratively. A gradient is computed at each step of each actuation (i.e., how much the change of one step affects the error), and it iterates for the actuator maximising gradient (minimising error).

## 2.5 Projecting on MistForm

The model described above, allows MistForm to reconfigure the 3D shape of its fog surface. However, as introduced earlier, the observer's location and projector's parameters are also required to correct shape distortion and uneven brightness. This section describes the process followed to calibrate the projector; it then provides a detailed description of a rendering process, and an evaluation of the final round trip reprojection error a user would perceive, as a result of inaccuracies in the calibration and 3D reconstruction method.

### 2.5.1 Projector calibration

To determine the intrinsic and extrinsic properties, the calibration uses a projector-camera system (inFocus In116A and Kinect v1). The calibration process first determines the projector's intrinsics and its position relative to a depth camera, then the position of the camera relative to MistForm is computed. The projector's intrinsics and extrinsics relative to Kinect were computed by using a sparse dataset of points mapping projected 2D coordinates to Kinect 3D coordinates (a fixed 9 x 6 checkerboard projected onto a flat white board, collecting a total of 594 points). This calibration process uses the approach by Zhang (2000) to retrieve projector's extrinsics ( $M_{kinect}^{proj}$ ) and intrinsics, and transforms the

intrinsic matrix<sup>2</sup> into the equivalent projection matrix ( $P_{proj}$ ). The process determines the position of Kinect relative to MistForm ( $M_{screen}^{kinect}$ ) using a checkerboard, as did the stereo camera before, which allows the computation of the projector position to MistForm ( $M_{screen}^{proj} = M_{screen}^{kinect} \cdot M_{kinect}^{proj}$ )

### 2.5.2 Rendering algorithm

MistForm’s rendering algorithm makes use of several stages, explained in the following subsections. Current implementation of MistForm with a single 3D projector can provide support for stereoscopic rendering for two users (exemplified later in this chapter); however, it can be used with glasses-free multi-projector arrays supporting several users. Additionally, brightness compensation in the rendering algorithm makes use of the attenuation profile of fog. However, using other profiles (e.g., the bidirectional reflectance distribution function of cotton fabric) will allow the algorithm to be reused for other shape changing displays.

#### 2.5.2.1 Rendering user-specific views

For a variable number of  $N$  users, the algorithm produces a set of  $2 \cdot N$  observer views, one for each eye (Figure 2.6 illustrates an example for one user, for simplicity). In the case of a multi-projector array, one observer view would be computed per projector. Let  $e_i \in E$  be an observer view,  $M_{screen}^{ei}$  its position relative to MistForm and  $P_{ei}$  the projection matrix that determines what the eye would see through MistForm’s from panel (defined by corners  $TL(-0.45, 0, 0.18)$  and  $BR(0.45, 0.56, 0.18)$ ).

The algorithm then renders the 3D scene into a texture  $t_i$ , capturing the observer’s view of the 3D scene from its position. This produces a total set of textures  $T = U_{i=1}^{2N} t_i$ , with the views of all  $N$  users around the display.

#### 2.5.2.2 Geometric compensation

Compensation of geometric distortion in each texture  $t_i$  can be faced as a projection mapping problem. Using the proposed regression model, it creates a 3D model of the current shape of the fog surface, and renders it from the projector’s perspective (i.e., using  $P_{proj}$  and  $M_{screen}^{proj}$ ), which allows MistForm to reconfigure the projection on each point of the fog surface.

---

<sup>2</sup><http://ksimek.github.io/2012/08/13/introduction/>

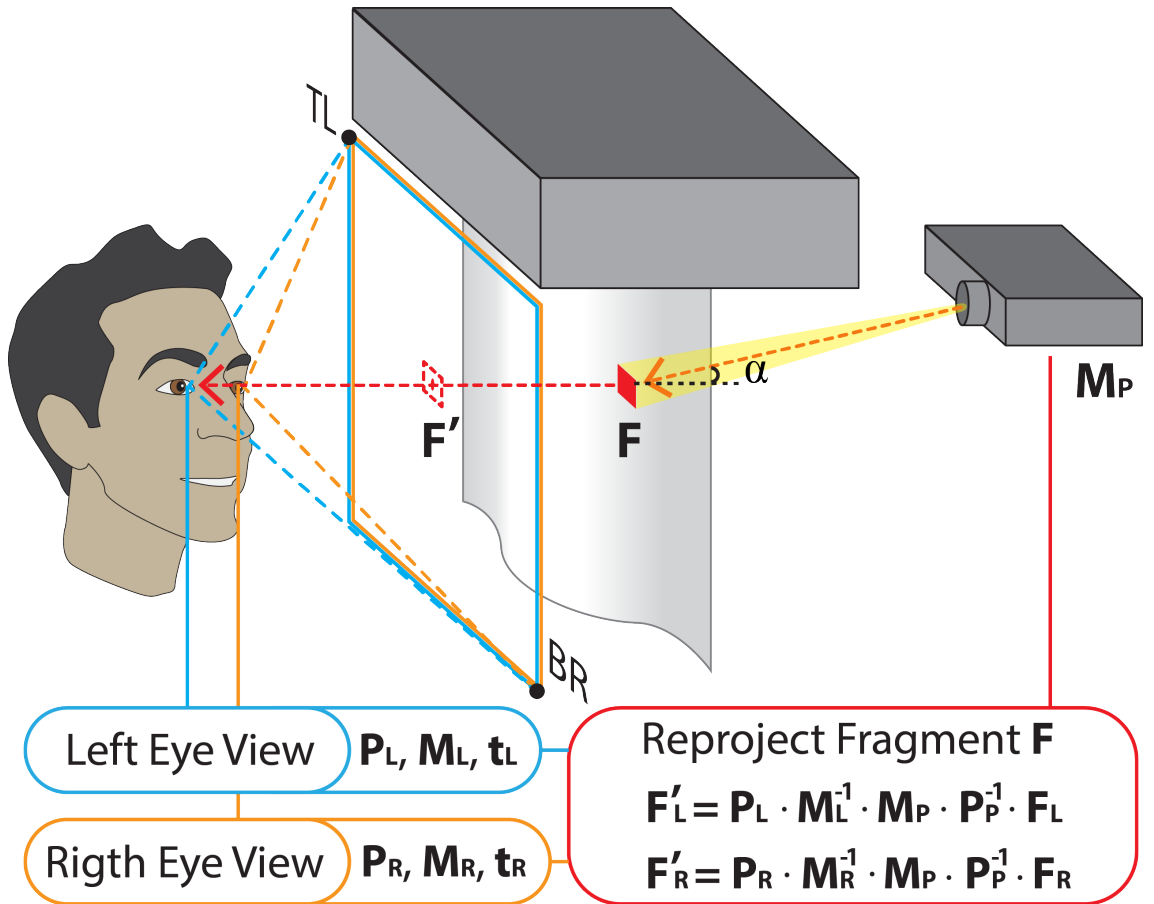


Figure 2.6: An example of the rendering algorithm for a user that computes the view of the user's eyes through MistForm's front panel. Each pixel,  $F$ , projected on the screen is reprojected towards the observer ( $F'$ ) to determine its colour.

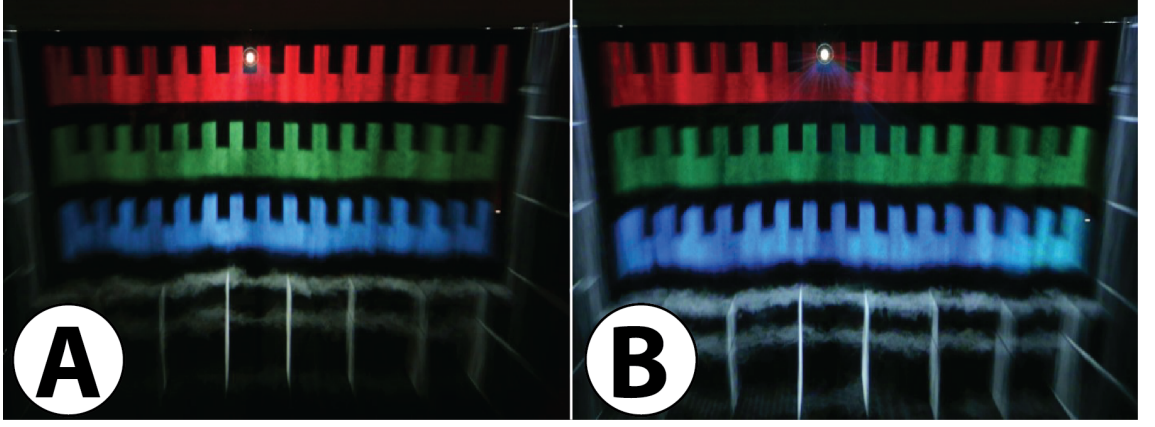


Figure 2.7: Example images of brightness without correction (A) and with correction (B).

MistForm created a custom fragment shader that reprojects each fragment (i.e., point on the fog screen) to the observer’s space and then retrieves the colour that should be projected on that point from  $t_i$ . Let  $f_{NDC}$  be the coordinates of the screen point in the projector’s  $NDC$  space. Its mapping to the observers’  $NDC$  coordinates ( $f_0$ ) can be computed as shown in Equation 2.4.

$$f_0 = P_{ei} \cdot (M_{screen}^{ei})^{-1} \cdot M_{screen}^{proj} \cdot (P_{proj})^{-1} \cdot f_{NDC} \quad (2.4)$$

The mapping from observer’s  $NDC$  to  $UV$  texture coordinates can then be easily computed as in Equation 2.5.

$$(u, v)_{ti} = (0.5 \cdot (f_0 \cdot x + 1), 0.5 \cdot (1 - f_0 \cdot y)) \quad (2.5)$$

It must be noted that all matrices (and their inverse) involved in this reprojection algorithm are constant across all pixels in a frame and can be precomputed once per frame. Thus, only matrix multiplications are required, incurring on a minimal performance hit.

### 2.5.2.3 Brightness compensation

To correct uneven brightness (see Figure 2.7), this study follows the approach described by Martinez Plasencia et al. (2014b), but instead of using a sparse attenuation mask and interpolation, the application is done on a per-pixel basis in the fragment shader. This is done by encoding the attenuation profile (i.e., mapping  $\cos \alpha$  to the inverse of the brightness distribution) as a precomputed texture. This is then used by the fragment shader to correct brightness on each pixel, based on the dot product between the projected ray and the observer (see angle  $\alpha$  in Figure 2.6).

### 2.5.3 Evaluation

To demonstrate that the algorithm can correct the projection distortion induced by the shape of the screen, MistForm displayed several virtual spheres on 50 different fog shapes (as seen in Figure 2.8 (left)), and analysed their reprojection error (i.e., distance between where each sphere should be seen and where it was actually detected). To do this, a calibrated camera is placed at 70 cm in front of the display (i.e., the position of an observer’s eye), and the spheres were distributed in three planes of 11 x 6 spheres, across MistForm’s volume (see enhanced working volume for 3D free-hand interaction, later). This study measures reprojection error using three alternatives:

- *No Correction*: This mode illustrates the effect of not taking the shape curvature into account. As a best effort in this case, this study computes perspective corrected views as seen through the plane  $Z = 0$  (i.e., centre of the volume).
- *Naïve Spline Reconstruction*: This study produces a *Naïve* reconstruction model based on cubic splines, and uses the displacement of control points (Equation 2.1) and the position of the two fixed ends of the pipe as control points to approximate the shape of the pipe, to extrude this curve downwards (i.e., fog flowing downwards), and to estimate the shape of the display. The proposed projection algorithm is used; the only change being the reconstruction algorithm.
- *Regression Model Reconstruction*: This measurement uses the proposed reconstruction technique and projection algorithm, as explained throughout this chapter.

Figure 2.8 (right) shows the results obtained from each of these three configurations. Unsurprisingly, the *No Correction* approach yields very negative results, with an average reprojection of  $12.34 \pm 8.9$  px (mean and standard deviation). Results only remain relatively low at the top centre of the display, where the camera is aligned to the projector, yielding minimum distortion. Considering the camera location and extrinsic parameters, this can translate in an error in the range of 0.49–3.02 cm. The high deviation of error across the display also implies noticeable distortion as content is moved across different points of the screen.

The *Naïve Spline* and *Regression* models resulted in average errors of  $6.36 \pm 3.72$  px and  $3.79 \pm 2.2$  px, respectively. Error distribution follows the previous observations, being relatively higher at the sides and bottom of the display. The *Spline* model shows greater errors on the right side of the display. This can indicate parts of the display

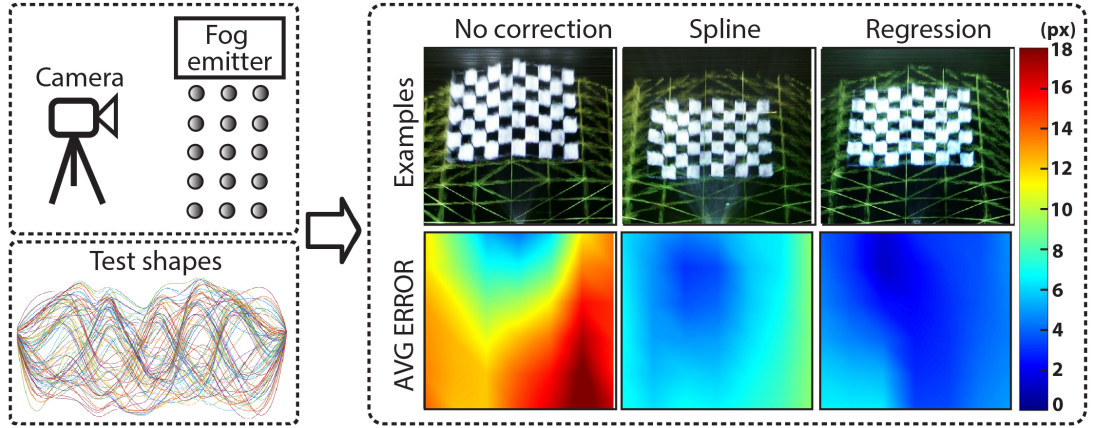


Figure 2.8: Projected virtual spheres distributed across MistForm’s working space (top left), using 50 different shapes (bottom left). The reprojection error for three different approaches: (left–right) no correction; *Naïve Spline* correction; using the proposed model.

with more complex dynamic behaviour as a result of the pipe, which does not adapt to a *Spline* model defined by the position of the actuators alone. The additional resolution in the proposed model allowed it to capture the complex dynamic behaviour, resulting in a more stable error distribution. The *Spline* model results in average error 0.91 cm, against average errors of 0.55 cm for the *Regression* model. This difference might not seem enough to justify a more complex reconstruction approach, especially considering the results from the proposed *Regression* model could be subject to a ceiling effect due to the inherent turbulence in the fog. Additionally, the higher deviation of errors in the *Spline* model (errors in the range of 0.37–1.43cm) results in a less stable correction as contents are moved across the display, while the proposed model provides more stable results (0.22–0.85cm).

## 2.6 Exploring interaction possibilities

The type of displays proposed in this chapter inherit affordances both from shape changing and fog displays. However, it is the combination of both that enables new interaction possibilities, both for 2D and 3D content. This section first identifies these novel affordances, then discusses the opportunities they raise for 2D and 3D interaction.

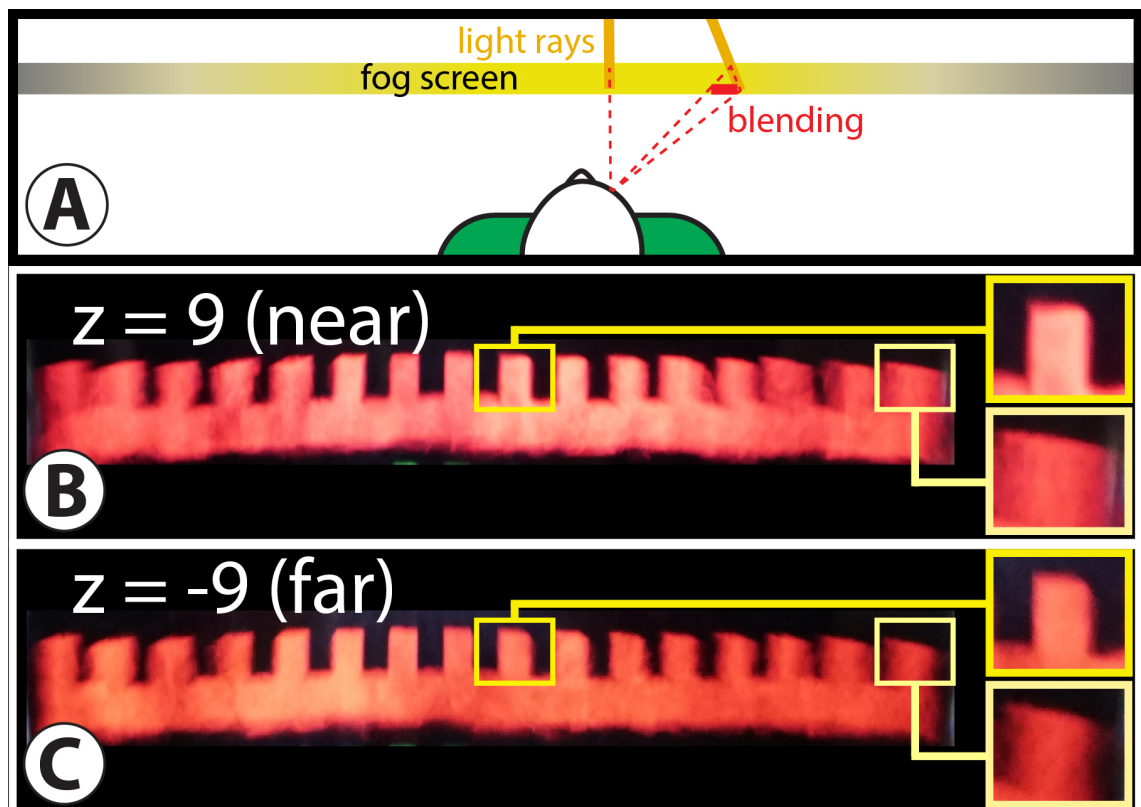


Figure 2.9: (A) The interplay between the position of the display, brightness and blending with neighbouring pixels. Both effects become more apparent when the display moves closer to the user (B), and decreases with distance (C).



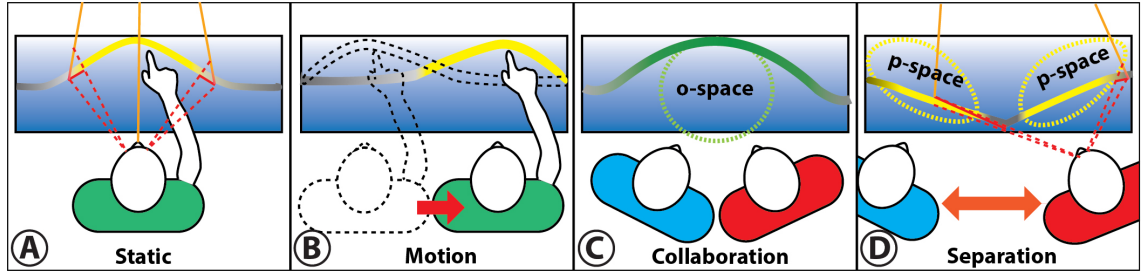


Figure 2.10: Examples for 2D interaction. (A) a concave shape produces a central region with optimum visibility, with bigger distortion to the sides; (B) this shape can adapt to user’s displacements in front of the display; (C) concave shapes offer support for close collaboration, while a triangular shape creates regions for personal interaction (D).

## 2.6.1 Identifying affordances

### 2.6.1.1 Blending, uneven brightness and shape changes

Fog screens introduce visual artefacts due to directional light scattering (uneven brightness) and volumetric scattering (blending pixels) of small particles (Rakkolainen, 2008b; Martinez Plasencia et al., 2014b). The tendency of pixels to blend with neighbouring pixels is related to the thickness of the fog display: light starts scattering as it travels through the fog curtain, which will make it visible in other areas/pixels of the display (see red area in Figure 2.9 (A)). Thus, blending will be minimal where the projector’s light rays are perpendicular to the fog surface, and will increase further to the sides. Uneven brightness is also related to the angle between the projector rays and the observer, making the display brighter between the observer and the projector and decreasing to the sides (as shown in Figure 2.9 (A) where yellow represents brightness). In a system such as MistForm where the user stands within an interactive range of the display and the projector is positioned far away, small displacements of the screen can have a drastic influence on these effects. As illustrated by Figure 2.9 (B), when MistForm is at its closest position to a user, both uneven brightness and blending become more significant than with the display 18 cm further away (Figure 2.9 (C)). MistForm’s shape-changing capabilities not only mitigate such common issues, but also turn these issues into reconfigurable features, which enable zones of shared visibility (Figure 2.10 (C)) and personalised 2D (Figure 2.10 (D)) and Figure 2.11 (B)) and 3D (Figure 2.13) views, as explained in the following next sections.

### 2.6.1.2 Zone of Comfort(ZoC), fog screens and shape changes

Autostereoscopic, multi-view and, in general, any planar 3D displays only allow small working volumes, due to the interplay between vergence–accommodation conflict ([Hoffman et al., 2008](#)) and the limited depth of field (DOF) of the human eye. When seeing 3D content in these displays, our eyes converge on the 3D object, but they must focus on the display surface (i.e., vergence–accommodation). Given the depth of field of our eyes ( $\pm 0.3$  dioptries (DPT)), only real objects within 0.3 DPT of the display surface will also be in focus, which defines the display’s zone of comfort (ZoC) ([Shibata et al., 2011](#)). Thus, if we focus on a display within our arm’s reach (e.g., 50 cm  $\sim$  2 DPT), we will only see our hand in focus in front of 7 cm of the display (43 cm  $\sim$  2.3 DPT), which means we will only be able to interact comfortably with 3D contents inside those 7 cm.

In comparison, MistForm offers two advantages. First, being permeable, our hands can access the space behind the display surface. In the example above, this would give access to an extra 9 cm (59 cm  $\sim$  1.7 DPT) resulting in a ZoC of 16 cm. Secondly, by moving the fog surface, the location of this bigger ZoC can be dynamically adjusted. By tracking user’s focus (their gaze or hand trackers, for instance), the dynamic ZoC can move to keep both hands and 3D content within the  $\pm 0.3$  DPT range, allowing comfortable interaction and without accommodation issues. Contents outside, would still be correctly visible (using the proposed algorithm), but the adjustable ZoC should move towards them if user still wants to interact with them. The implementation – explained later in this chapter – describes how this can be used to increase the working volume from 7 cm up to 30 cm.

### 2.6.2 Interacting with 2D content

When not using 3D glasses, MistForm can be used to display 2D content on its display surface. The geometric compensation is not needed here, but the display’s shape reconstruction will still be needed to wrap contents correctly (e.g., to make the curvature of a dialog window match the actual curvature of the screen) and to allow user’s input to be mapped to content correctly (e.g., to map a finger touch to a small button).

Exploiting the relationship between brightness, blending and shape, MistForm’s projection surface can adapt to the position of users in front of it. For a single user, a concave shape can cover the space his arms can reach comfortably (Figure 2.10 (A)). The central part of the shape would minimise artefacts, enabling a main space for interaction, the

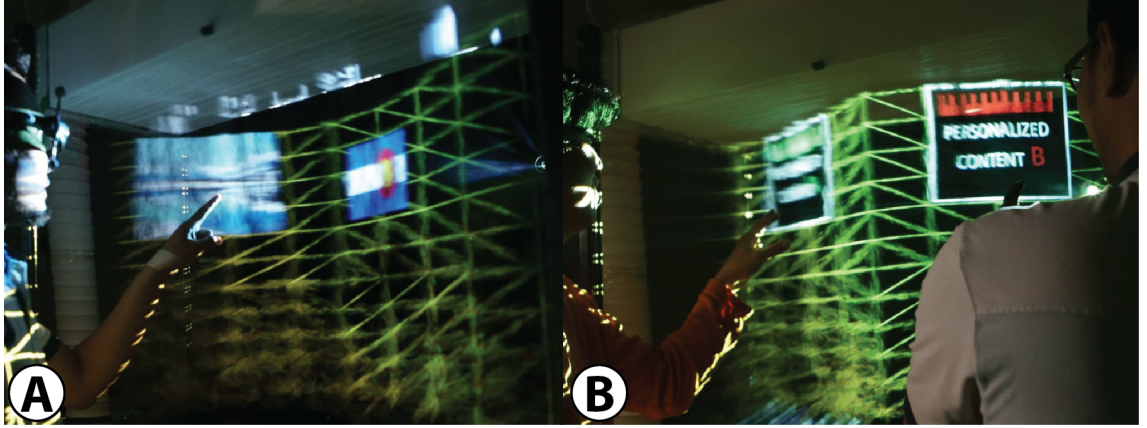


Figure 2.11: Concave shapes adapt well for single user scenarios (A). Triangular shapes create separate spaces for two users (B).

space closer to the periphery would suffer both from blending and lower brightness, making it more appropriate for holding peripheral content. Adapting the shape as the user moves (Figure 2.10 (B)) can keep contents within reach or even at constant positions relative to the user (central or peripheral), as a reduced version of the personal cockpit (Ens et al., 2014). If a second user joins, this affordance can be applied to reinforce proxemic interactions between the users (Ciolek and Kendon, 1980). For collaborating users (see Figure 2.10 (C)), the display should be placed to the back of their o-space (Figure 2.10 (C)), but still within the limits of the user's reach. This will ensure that brightness is higher for both observers.

In contrast, if users break apart to focus on individual tasks (e.g., separation, divergent users' views), the display could progressively reconfigure its shape from a concave to an almost triangular shape (see Figure 2.10 (D)), creating a differentiated surface for each user. Unlike the previous configuration, this would result in considerably different angles between each point of the screen and the observers; while the space in front of each user would offer good visibility for them personally, their visibility of the other user's space would suffer from high brightness attenuation and blending. These attributes work together to create personal spaces for each user (see Figure 2.11 (B)).

### 2.6.3 Interacting with 3D content

#### 2.6.3.1 Enhanced working volume for free-hand 3D interaction

MistForm was designed relying on the possibility of dynamically regulating the ZoC of the display, by adjusting the position and shape of the fog display. MistForm offers a

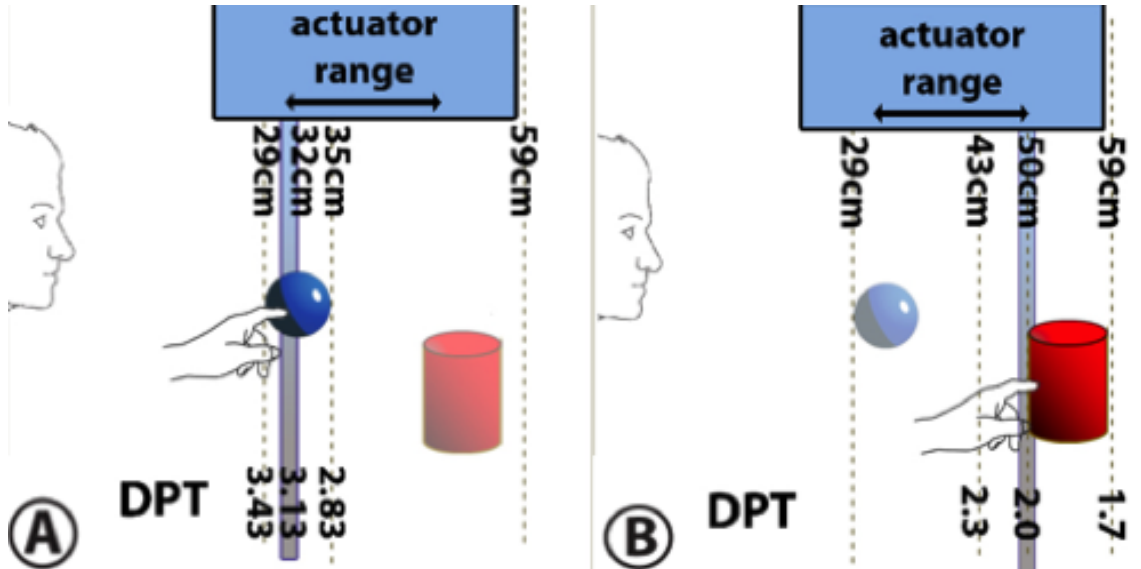


Figure 2.12: The actuator's range (18 cm) is enough to dynamically extend the display's ZoC to cover the full range that an average male user can reach comfortably, by adjusting the position of the fog screen.

total working depth of up to 30 cm, covering the space where an average male adult user can interact comfortably. This study uses the ergonomic metric RULA ([McAtamney and Corlett, 1993](#)) and computed minimum (i.e., upper arm at  $-10^\circ$ ; and lower arm at  $100^\circ$ ) and maximum interaction distances (i.e., upper arm at  $45^\circ$ ; and lower arm at  $80^\circ$ ). Using average anthropometric measurements (i.e., upper and lower arm length of 36.88 cm and 35.92 cm respectively), this results in a working depth of 28.8 cm and 55.4 cm, which aligns with estimates by other researchers, (for example, 0.4–0.8 arm's length in a work by [Valkov et al. \(2011\)](#)).

In Figure 2.12, (A) and (B) illustrate how the range of the linear actuators (18 cm) is enough to cover this working volume for a user standing at 32 cm from this display. In this situation, for any 3D content shown inside the working volume, it is possible to place the diffuser surface within 0.3 DPT, assuring that both the object and the user's hands that are interacting with it stay within the ZoC. User's hand position has been used to detect the intent of his/her interaction. The bounding box of the objects within 7 cm to the hand are fed to the shape control algorithm to automatically determine the best display position. This binary condition can cause sudden changes of shape when hand movement makes an object fall out of the range, and progressive approaches should be taken instead.

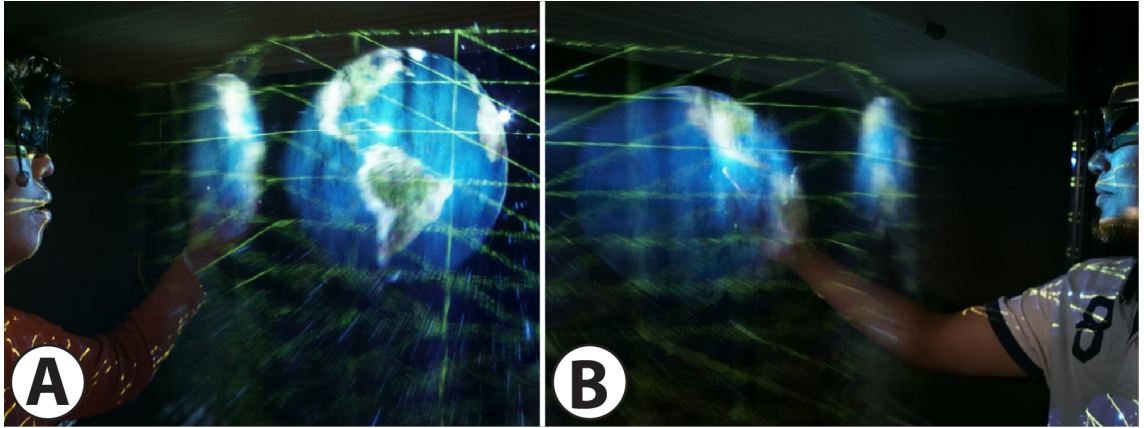


Figure 2.13: Triangular shapes provide users with independent 3D views, while minimising visibility of the other user’s view.

### 2.6.3.2 Support for multi-user scenarios

The dependency between brightness, blending and shape allows MistForm to deliver different 3D views to its users, within limitations. Multi-view support is depicted in Figure 2.13, and it is based on the use of triangular shapes. As explained in the multi-user 2D scenarios, this configuration maximises the difference in perceived brightness between the two regions of the display and was used as a way to enforce disjointed working spaces. The same property has been used to allow for different perspectives of the same shared 3D object, presented in the o-space between the users. Each user will see a bright image of the 3D object from his/her perspective, while only receiving a residual image (i.e., less bright and distorted) from the other user’s perspective. The technique in this chapter, cannot allow for full multi-user 3D support (e.g., contents spanning across the whole screen) and can only dedicate specific parts of the display to each user. However, this technique can still be of use in the examination of common objects of interest; it can be supported with a conventional 3D projector and can be combined with personalised 2D contents to support mixed focus scenarios, such as those by [Martinez Plasencia et al. \(2014b\)](#).

## 2.7 Discussion

MistForm is the first system to explore the novel interactive possibilities that arise from combining: a) the inherent properties of fog as a display medium; and b) the ability to dynamically track and move the permeable screen to affect its visual properties. The research included in this chapter has shown how this can offer innovative possibilities. Adjusting the shape of the display can be used to reduce blending and uneven brightness,

which are known issues in fog displays, and the shape changes employed can transform these issues into useful and controllable features. The research in this chapter explored this feature and identified display configurations to optimise visibility to all users or to produce personalised regions to specific users. Combining the shape changing patterns with proxemic or ergonomic considerations and specific use cases, have allowed this study to identify interesting usage scenarios.

Moving the fog surface enabled a dynamic/movable ZoC, which allowed the current research to produce a prototype that provides a working volume more than four times large than an alternative planar 3D (despite using a relatively small actuation range of 18 cm), which allows for the comfortable interactive range of an adult user. MistForm’s dynamic ZoC can offer a flexible alternative to other display techniques in scenarios where 3D interaction with our real hands, real tools, or semiotic gestures aimed at co-workers are important. For example, in a 3D CAD application, a designer using a cave automatic virtual environment (CAVE) will only be able to interact comfortably with 3D content within the front few centimeters of the display. Proxies (e.g., virtual hands and pointers) allow for interaction beyond this space, but at the expense of the expressiveness of the user’s real hands (eyes focus on the CAVE wall, not on the hands). If the designer needs to be aware of a client’s feedback (e.g., the client pointing at a part of a 3D object), the designer will be forced to switch focus between the display surface (to view the content) and the client’s hand (to observe the gesture). This can hinder collaboration and create unnecessary visual fatigue, as the user must constantly shift focus between their hands and the display, even if both are virtually close. VR solutions can attenuate these issues, as they do not require shifts in focus; however, direct facial expressions are occluded and collaboration is limited by the expressiveness of the mediators (i.e., avatars) used. Benefits also apply in training scenarios, e.g., conducting a surgery, where tools (e.g., scalpels) are central to the task. MistForm allows hands, scalpels, and (virtual) organs to remain in focus. An awareness of their surrounding which is not possible when using HMDs, will allow trainees to observe and engage with other users as in the real world, e.g., nurses in an operation theater. The techniques have been described, and their evaluation using the MistForm prototype, should also serve as a basis for other researchers exploring this field, and help them to solve the most demanding challenges involved.

The prototype presented, however, is not free of limitations. The *Naïve* model of actuators and fans is noisy (66 dBA at the user’s interaction area), which can hinder interaction, particularly when considering collaborative scenarios such as conversing with



peers. Using an aerosol heavier than air (e.g., cooling-down fog, or using dry ice) may offer a departure point for further exploration. The fog aerosol in MistForm is lighter than air, which requires the use of a relatively faster flow of air to achieve the desired display height. A heavier aerosol will function with a slower flow, allowing the use of less powerful, and therefore, quieter fans. A better choice of linear actuators may also reduce noise even further, and could also improve MistForm’s ability to adjust its ZoC (currently limited to 40 cm/s), making it suitable for tasks requiring faster hand motion. The choice of active shutter glasses will also affect perceived brightness, which may become an issue if larger form factors are explored (i.e., brightness will become even lower to the sides, and shutter glasses will further decrease brightness). Although this was not an issue with MistForm, this choice of 3D technology was simply a matter of convenience, and this chapter suggests interested practitioners to use alternative technologies, such as passive glasses. This will involve the calibration of a second projector, but the methods and algorithms described herein will remain applicable.

Using multiple projectors is another interesting line of exploration. As demonstrated by [Yagi et al. \(2011\)](#), a multi-view display can be created using a dense array of projectors, removing the need for 3D glasses. Furthermore, as these rely on using the brighter parts of the scattering function (i.e., users see the pixels from the projector that is directly aligned with their eyes), this will allow for the use of dimmer projectors while still making better use of their brightness profile. Moving the display surface relative to the user may also help align the view to the user’s eyes and thus avoid crosstalk between other views.

## 2.8 Conclusion

MistForm is a novel display technology combining the affordances of shape changing and fog displays. This chapter presented a suitable design and identified challenges related to this technology, addressing the estimation of the display shapes created and a projection algorithm to remove optical artefacts using geometric and brightness compensation. It also evaluated both the reconstruction and projection algorithms, and showed that the proposed technique can successfully minimise the distortion that occurs as a result of projecting on changing surfaces. This work explored the novel possibilities enabled by combining the shape-changing with mid-air displays. For example, MistForm can change shape and demonstrate how brightness and blending affect different areas of the display. This chapter showed how this can be used to support different scenarios involving single

or multiple users. It also indicated how moving the fog surface can create a dynamic ZoC for the display, enabling freehand interaction over larger volumes without vergence–accommodation issues. These features illustrate the potential of MistForm and enable new forms of interaction and collaboration. Although this chapter provides information that supports the ability to reconfigure mid-air displays composed of permeable materials, two drawbacks are observed. First, the system is noisy and bulky due to the hardware requirements, e.g., a pipe for mist diffuser, mechanical actuators to drive the pipe, fog machine, and a base to support the system. Second, it only offers coarse control. Chapter 3 and Chapter 4 discuss how to limit these drawbacks. The thesis author invented the idea in these chapters, designed and implemented them, gathered and analysed the experimental data, demonstrated the concept and wrote the published manuscripts of the chapters (Norasikin et al., 2017, 2018, 2019) with contributions of all authors.



## Chapter 3

# SoundBender: Dynamic acoustic control behind obstacles

### 3.1 Introduction

The ‘Ultimate display’ (Sutherland, 1965) and Ishii’s ‘Radical Atoms’ (Ishii et al., 2012) have encouraged HCI researchers to reconfigure matter at a distance for user interface applications, including the one described in this chapter<sup>1</sup>. Sutherland (1965) imagines a display that can present information by reconfiguring existing matter, and that matter does not necessarily need to follow the physical reality, as an opaque screen must, which that a display can be made of transparent materials. Meanwhile, Ishii et al. (2012) envisioned digital information manifesting physically.

A number of contactless approaches exist for reconfiguring matter in the air (i.e., light-scattering particles), such as aerodynamics (Alrøe et al., 2012), magnetophoresis (Lee et al., 2011), ultrasound (Ochiai et al., 2014; Omirou et al., 2015; Marzo, 2016), and optical traps (Smalley et al., 2018b). Among these approaches, ultrasound has received particular attention, for two essential reasons. First, by using non-audible sound waves, the approach provides specific affordances (i.e., levitation and tactile feedback), without interfering with audio modalities (e.g., no parasitic noise). Second, ultrasound only depends on the acoustic pressure of the sound field, and in the case of levitation, on the object’s density. No other physical properties, such as magnetic or electrical properties, are required. These benefits

---

<sup>1</sup>The preliminary study of this chapter was presented at the 24<sup>th</sup> International Congress on Sound and Vibration ICSV24 (<https://iiav.org/icsv24/>). The final study was published in the Proceeding UIST ‘18, Proceedings of the 31<sup>st</sup> Annual ACM Symposium on User Interface Software and Technology, pp.247–259 (<http://doi.acm.org/10.1145/3242587.3242590>)

allow acoustic levitation to be applied to materials ranging from polystyrene beads to coloured liquid (Foresti et al., 2013), and even food (Vi et al., 2017).

The bulk of previous approaches for reconfiguring matter with ultrasound relied on the use of arrays of ultrasonic transducers, either to create standing waves using the nodes and anti-nodes of sound waves for levitation (Sahoo et al., 2016; Williamson et al., 2017), or to create more complicated fields, such as multi-point feedback (Long et al., 2014), where the sound waves are focused at several points in space for providing tactile feedback (i.e., focal points), or the use of acoustic tweezers (Marzo, 2016), which create a physical pincer using sound field that are capable of trapping an object in free air. However, the physical size of the transducers limits the resolution of the sound fields that can be created. According to Nyquist (1928), reconstructing the sound field of a specific frequency requires the sound sources to be separated by less than half of the wavelength ( $\lambda$ ) of said frequency (modulator pitch  $< \lambda/2$ ). However, the size of commercially available ultrasound transducers easily exceeds this threshold (e.g., transducer at 40 kHz is 10mm  $\varnothing$ ;  $\lambda/2 \approx 4.3$  mm).

Acoustic metamaterial (MM) can avoid this limitation, as it allows for a much smaller modulator pitch compared to commercial transducers. Acoustic MM are assemblies of unit cells, each inducing a local change in the phase and/or intensity of the incoming acoustic waves. Since MM can be 3D printed with ease, the size of each cell can be designed to offer the required modulator pitch (i.e., cell size  $< \lambda/2$ ), even in the ultrasonic frequency range. These have been used to reconfigure vibrations (Ion et al., 2017) and sound (Li et al., 2016). Ion et al. (2017) proposed a reconfigurable MM structure that has the capability to perform a task with vibration propagation, for example, to lock and unlock a doorknob. This is achieved through cells of bistable springs. Meanwhile, Li et al. (2016) proposed a modular sound filter that is able to improve the sound quality of an audio output device for any given geometry of the physical structure. The primary benefit of acoustic MM is that it can encode complex fields. However, they are generally static in nature (i.e., they do not change over time), and their application for creating interactive features, remains unexplored.

This chapter presents SoundBender, a hybrid ultrasound modulator that reconfigures matter in free air, by combining the benefits of acoustic MM and PAT. The MM encodes a complex but static sound field (e.g., an acoustic hologram), while the PAT adds dynamic and real-time control (e.g., it can move/stretch the sound field in 3D, and switch between levitation and tactile functionalities). The first part of this chapter reviews relevant literature of PATs and acoustic MM, and describes a preliminary study of the hybrid

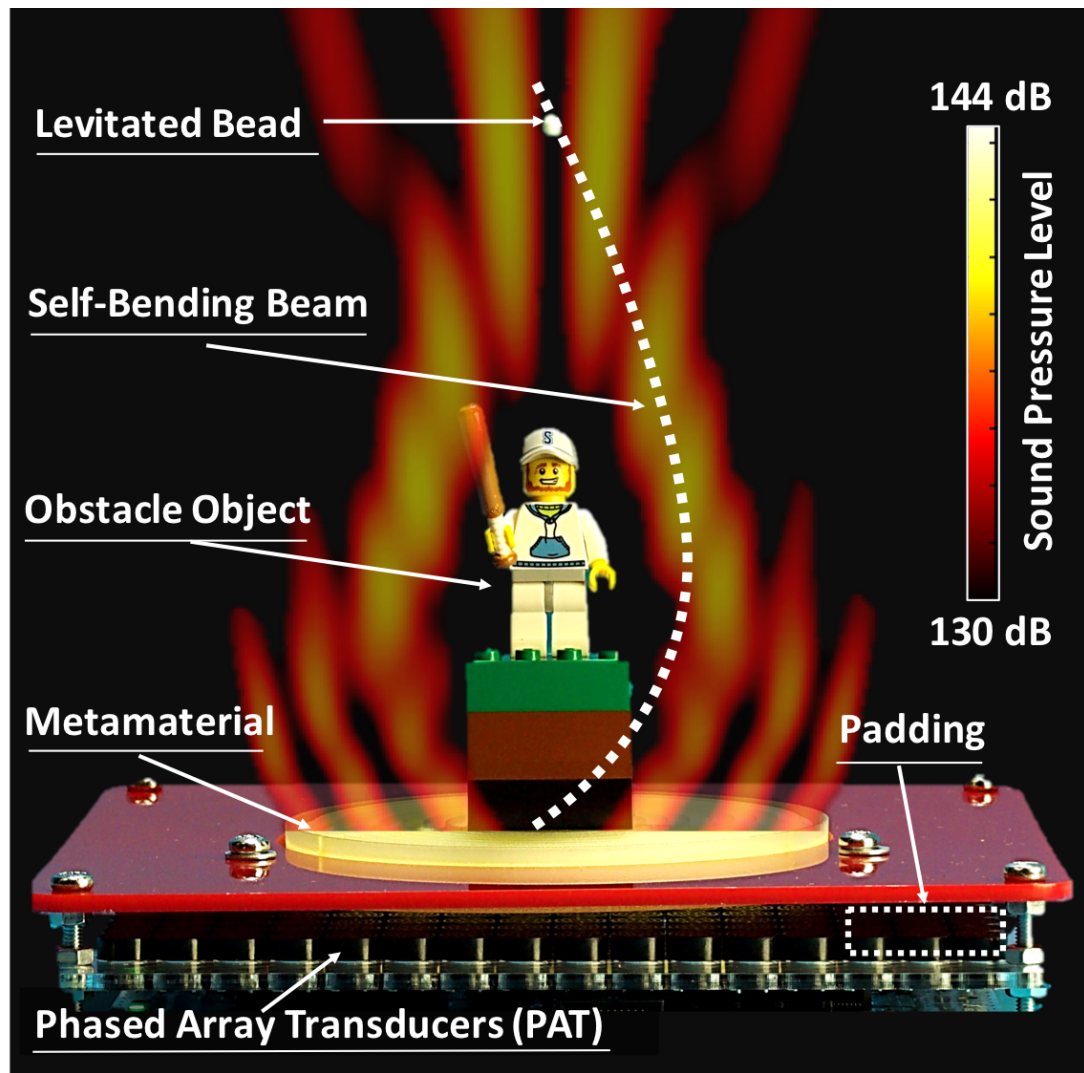


Figure 3.1: SoundBender combines ultrasound transducer arrays and acoustic MM to create a complex sound field (i.e., self-bending beams). The self-bending beam allows for dynamic features (e.g., levitation) above passive props, while the phased array allows interactive 3D control of the position of the features.

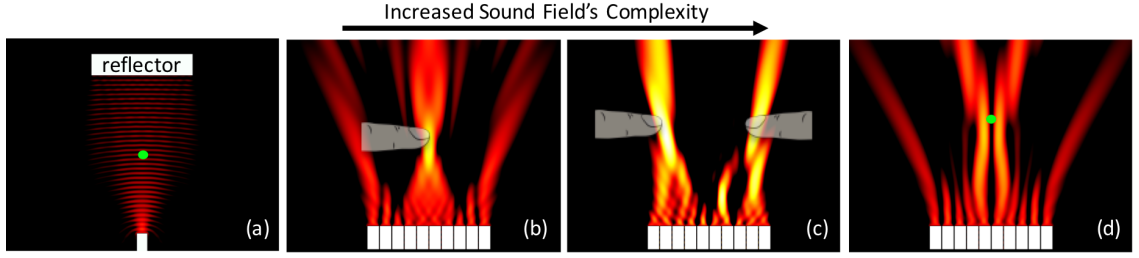


Figure 3.2: Example sound fields of increased complexity, created using PAT: (a) Standing wave (using a transducer and a reflector) (Omirou et al., 2015; Sahoo et al., 2016); (b) single focal point (Carter et al., 2013); (c) multi-focal points (Long et al., 2014); and (d) acoustic tweezers trap for one-sided levitation (Marzo et al., 2015).

modulator, SoundBender, where it provides a technique to exploit a combination of PAT and MM to manipulate a complex sound field (i.e., self-bending beams), and reveals the potential of such a hybrid modulator to reconfigure matter in mid-air.

The second part describes the final study and presents the capabilities of the hybrid modulator. The modulator utilises the complex sound field (bent beam) to bend around static objects on top of a modulator and create interactive features (e.g., levitating and controlling light scattering particles, steering non-solid matter light scattering particles around the static object, and creating dynamic tactile points). Figure 3.1 illustrates how the hybrid technique creates the bent beam, levitates matter, and reconfigures it in a 3D space. This chapter also presents an evaluation of the technique used for recreating the intended sound fields (i.e., self-bending beams) and reconfiguring matter in mid-air, and discusses the application scenarios enabled by SoundBender, highlighting potential areas of further research for the HCI community in future.

## 3.2 Related work

This section reviews relevant research pertaining to matter manipulation and reconfiguration in mid-air using ultrasound approach. The technique can be classified into two types: transducers-based and acoustic MM-based. This section evaluates their strengths, limitations and the key techniques in relation to SoundBender.

### 3.2.1 Transducer-based acoustic modulators

The ultrasound approach offers interesting capabilities in levitating and manipulating substances in the air, and has a profound significance in biomaterial (Vasileiou et al., 2016),

pharmaceutical (Weber et al., 2012), and microparticle (Hertz, 1995) studies. Acoustic levitation was first observed more than 150 years ago, with small dust particles being trapped in the low-pressure lobes of a standing wave (Poynting and Thomson, 1906). This inspired the first example of particle levitation using a setup consisting of a transducer and an opposing reflector plate set-ups (Brandt, 2001) (as in Figure 3.2 (a)).

This transducer–reflector technique has been exploited to levitate and manage different substances in the air, including living organism such as insects (Xie et al., 2006) and fish embryos (Sundvik et al., 2015). The principle behind this technique, using either a transducer and reflector or a pair of opposing transducers, is reliable and leads to strong trapping forces, which is why it is at the core of advanced graphics and display applications and recently has been extensively used within the HCI community (Ochiai et al., 2014; Omirou et al., 2015; Sahoo et al., 2016; Omirou et al., 2016).

PixieDust (Ochiai et al., 2014), for example (see Figure 3.3), used two pairs of opposing PATs for acoustic levitation. It created a reconfigurable floating display system of light scattering particles, which exploited a repeated lobe pattern in standing waves to levitate and reconfigure a group of light scattering particles (i.e., polystyrene beads). It projected static and dynamic graphical information onto the beads with a light projector, and shifted the phase of the transducers to move those shapes in 3D space. LeviPath (Omrou et al., 2015) used the same technique to allow for 3D displacements of light scattering particles, but constrained the displacement to specific directions according to a motion sensor (i.e., leap motion). Floating Charts (Omrou et al., 2016) later adapted the technique to create a module of levitated display. It was capable of reconfiguring each light-scattering particle in mid-air as free-floating charts. JOLED (Sahoo et al., 2016) further improved the technique and presented a concept of a levitated game and bistable display. It was capable of reconfiguring the rotation of the levitated particles, with control achieved by first coating the two hemispheres of the particles with two different materials. One hemisphere was coated with an electric charging material (i.e., titanium dioxide ( $\text{TiO}_2$ )), while the other hemisphere was covered with colour paint. The system used a dielectric polarisation mechanism to rotate the particles, where it changed the charges of the polarity of the particles by modulating the voltage through transparent electrodes. Consequently, this technique presented the different physical properties of the particles to users. However, this technique starts to fail when more control on the individual levitated matter is desired (e.g., movement): not only is the spacing between the traps is limited to half-wavelength  $\lambda/2$ , but the entire standing wave needs to be shifted for a single trap to be displaced.

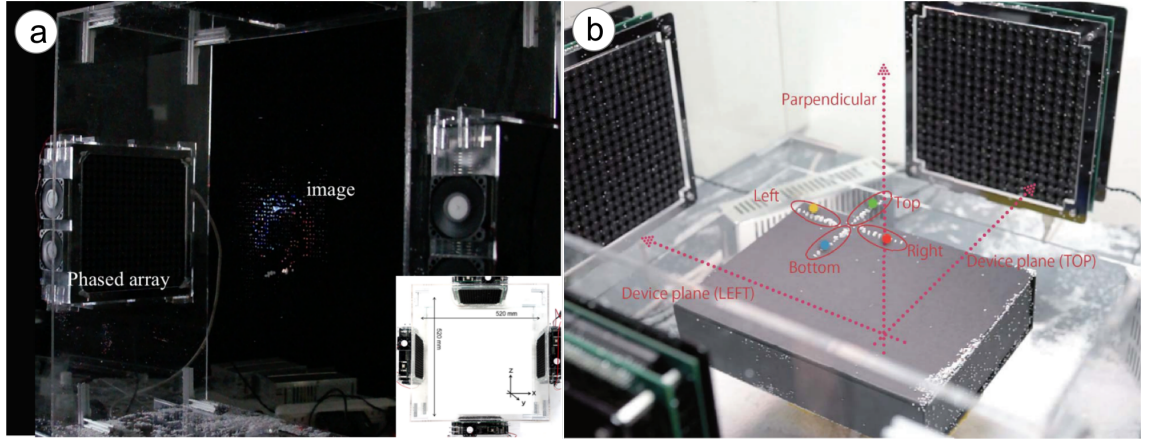


Figure 3.3: A mid-air display of levitated particles (Ochiai et al., 2014).

The typical solution is to use transducer arrays, as in ‘acoustic tweezers’ technique (Lee et al., 2005; Lee and Shung, 2006; Baresch et al., 2016) (see Figure 3.2 (d)), where precise control of the phase of each transducer allows for dexterous control of one or multiple traps. Typically, at least two pressure focal points are used to levitate substances against gravity. A variation of this technique (i.e., ‘tractor beam’) even achieved manipulation of substances in the air using a single-sided transducer array (Marzo et al., 2015, 2017b).

Levitate (Williamson et al., 2017) introduced path-tracing algorithms to animate multiple voxels in 3D space. This technique has also been used for tools (Marzo et al., 2017b) or gloves (Marzo, 2016). Using this one-sided technique, other works have exploited sound interference and have achieved greater control over the sound field. Carter et al. (2013) used constructive interference at a focal point (see Figure 3.2 (b)) with this technique, and modulated the ultrasound wave at 200 Hz to allow skin receptors to perceive acoustic radiation, thus enabling mid-air tactile sensations. Long et al. (2014) extended this method for the multi-point technique (see Figure 3.2 (c)). However, this technique has three main limitations: the forces are relatively small in the plane perpendicular to gravity, the size of the levitated particles is limited to half the wavelength (due to diffraction), and when transducers are larger than  $\lambda/2$ , they are subject to energy losses due to aliasing effects.

The literature reports two other interesting techniques for acoustic levitation: a tripod-like technique, which was used to levitate a large polystyrene sphere (50 mm in diameter) (Andrade et al., 2016), and a  $\lambda/2$  trap technique, which was used to levitate a compact disk on top of a 19 kHz transducer (Zhao and Wallaschek, 2011). Despite these two techniques successfully levitating large objects, the distance between the transducer(s) and the levitated object was approximately half-wavelength. Additionally, in the case of the levitated CD, a rod was being used to stabilise the levitated object in the acoustic



field, thus decreasing the versatility of the system.

The techniques above offer excellent control in terms of phase and amplitude. However, they rely on PATs, and the size of existing ultrasound transducers exceeded the minimum pitch requirement (i.e., the separation between its sources/transducers) for regenerating the maximum frequency of a sound field. For example, to recreate a sound field at 40 kHz with a commercial PAT that has 16 x 16 transducers, where each transducer has a 10 mm diameter (e.g., Ultrahaptics, version 2.0.0, pitch 10 mm), the maximum temporal frequency that can be reconstructed from a fast Fourier transform (FFT) analysis is  $\sim 15$  kHz (Press et al., 1988). This does not mean they cannot reproduce any sound field at 40 kHz; however, it limits their application to sound fields with a higher spatial resolution (i.e., high-fidelity sound fields).

A similar 16 x 16 arrangement, but with sources spaced  $\lambda/2$ , will allow reconstruction at  $\sim 35$  kHz. A higher number of sources can marginally increase these limits, but only a pitch less than  $\lambda/2$  will allow reconstruction at full 40 kHz. Thus, the limiting factor for PATs is the size of its transducers. Transducers require a parabolic plate, to help direct and focus the acoustic pressure, but the size of the radiating area ( $D$ ) of the parabolic plate must remain larger than  $\lambda$  ( $D \gg \lambda$ ) (Waanders, 1991), which practically limits the minimum size of focused transducers (and the minimum pitch of a PAT) in terms of being larger than  $\lambda$ . Non-focused, flat-mounted transducers (Kota and Nakatera, 1996) allow for smaller sizes ( $\sim 6$  mm) but they are still larger than  $\lambda/2$ , and their lower radiating pressure also renders them unsuitable for HCI use, e.g., for levitation (Waanders, 1991).

Spatial aliasing effects will occur when transducer size is greater than  $\lambda/2$  (Hertz, 1995; Weber et al., 2012; Sundvik et al., 2015). This effect happens due to insufficient sampling of a data along a space axis and is a universal problem. To solve this problem, this thesis refers to work by Nyquist (1928), which suggests sampling two points per wavelength,  $\lambda/2$ . A preliminary exploration of spatial aliasing was carried out in this study. Figure 3.4 (a) shows that the spatial aliasing effect occurred when a commercial PAT of 40 kHz transducers (transducer's diameter = 10 mm, half of a wavelength  $\lambda/2 = 4.3$  mm) was used to reconstruct a complex sound field (i.e., bending beam). Figure 3.4 (b) shows that bending beam successfully reconstructed of closely packed transducers, which each of the transducer has half of wavelength diameter ( $\lambda/2 = 4.3$  mm). When the study of SoundBender was carried out, a commercial phased array with 4.3 mm transducers was not present. To achieve such a small source, a low-cost 3D printed labyrinthine MM bricks (Memoli et al., 2017) with a lower pitch were designed and assembled in front of the 40

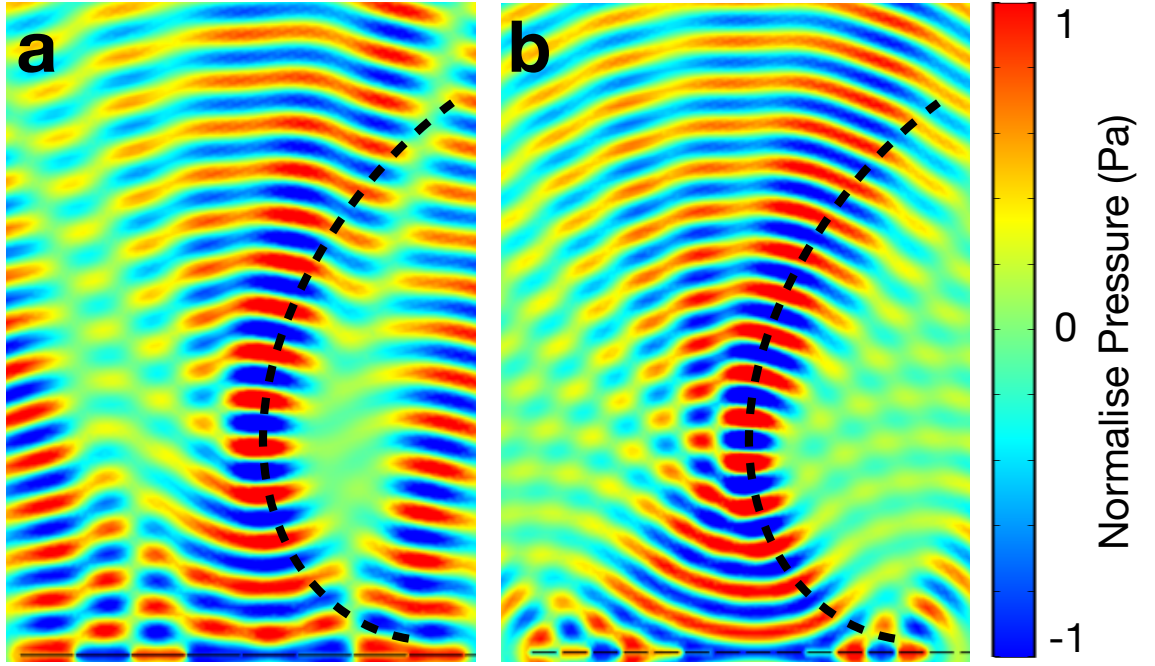


Figure 3.4: A simulated self-bending beam with transducer arrays of different sizes and spacing: (a) transducer's diameter = 10 mm, spacing 10.5 mm; (b) transducer's diameter is 4.3 mm, spacing is 6.3 mm spacing.

kHz ultrasound array, acting as a lens for the high-fidelity sound field. The array was later is used to modify (e.g., steer or stretch) the sound field. The next section will review the works related to MM-based acoustic modulator techniques.

### 3.2.2 Metamaterial-based acoustic modulators

Prior research in acoustics explored acoustic MM, a technique that produces a high-fidelity sound field beyond the transducer's limits. Acoustic MM are elements specially designed to manipulate the phase and amplitude of the incoming wave to create and control the sound field (e.g., by directing a focal point).

The MM technique has been successfully used to manipulate a sound field to create negative diffraction (Wang et al., 2016), self-bending beams (Li et al., 2014a), acoustic holograms (Melde et al., 2016), 2D letters made of sound (Xie et al., 2016), structures to deviate seismic waves (Colombi et al., 2016), and also for acoustic levitation (Memoli et al., 2017). It can be easily 3D printed, and is able to provide sound fields with higher spatial resolution than transducers alone can provide (Wang et al., 2016). Melde et al. (2016) used the MM technique to reconfigure water with sound, and to demonstrate the drawing of a 2D image, or to control the trajectory of matter, both on the water's surface.



The work first defines the 2D image and computes its 2D phase profile. Next, the distance between the reconstructed image on the water’s surface and the MM is defined. When the MM is placed in front of a planar ultrasound source in the water, it will modify the 2D phase profile, drawing the target image on the water’s surface.

[Xie et al. \(2016\)](#) designed an optimised MM technique, reconfiguring a complex sound field to draw images – the letter ‘A’, for example. The work modified the Weighted Gerchberg-Saxton (GSW) algorithm to obtain optimal phase distribution for the sound field. The work designed a set of twelve 3D printed unit cells of optimised labyrinthine, made of acrylonitrile butadiene styrene (ABS) plastics, operated at a frequency of 4,000 Hz (i.e., a frequency within audible range frequency) with  $180^\circ$  – of relative phase delay coverage and with constant transmission amplitudes. The work found strong agreement between the measured and simulated sound field of the target image reconstruction.

[Memoli et al. \(2017\)](#) then explored the use of the MM technique in the ultrasound region (40 kHz). The work demonstrated that high-fidelity sound fields could be created from a discrete set of 16 phased-delay bricks (pitch  $\approx \lambda/2$ ) with a constant amplitude, which highlights the advantage of MM over PATs, i.e., a high density of sources.

The main drawback of the MM technique is that MMs are static. Thus, they are tailored to one specific function and have no dynamic control over phase and amplitude. Some designs, use moving parts ([Chen et al., 2014](#); [Popa et al., 2015](#)), but only allow for minor changes to the created sound field, a limit that opens up a new exploration in reconfiguring matter through hybrid acoustic MM.

SoundBender draws on a hybrid technique based on the limits and strengths of both MMs and PATs above. SoundBender uses the strength of MM (i.e., high-density source) to create a complex sound field, and overcomes the limit of the static MM with sound field reconfiguration through the PAT, creating a hybrid sound modulator. SoundBender incorporates a complex sound field (i.e., bent beam) derived from the work of [Zhang et al. \(2014\)](#), which projects acoustic energy along a predetermined curve for the beam (as can be seen in Figure 3.4 (b)). This curved beam is hardly done by using PAT of larger than the said wavelength (as in Figure 3.4 (a)). The following section discusses a preliminary study on how to design the complex sound field (i.e., self-bending beams) with MM, and a technique for reconfiguring the sound field.

### 3.3 Preliminary study of a self-bending beam and reconfiguration method

The concept of self-bending beams (used in this chapter to illustrate the technique in SoundBender) was initially used in engineering applications, to blanket buildings from noise (Maldovan, 2013) or to protect areas from earthquakes (Colombi et al., 2016). Such beams can produce a focal point at the end of the curve (Li and Assouar, 2015; Gao et al., 2016) and act as single beam acoustic tweezers (Lee et al., 2009; Zheng et al., 2012; Li et al., 2014b). With the ability to circumvent obstacles and self-heal (Zhang et al., 2014; Zhao et al., 2014; Li and Assouar, 2015; Gao et al., 2016), self-bending indicates a promising method for allowing obstacle avoidance (Siviloglou and Christodoulides, 2007; Greenfield et al., 2011).

The first practical realisation of self-bending in acoustics (Zhang et al., 2014) utilised PATs of 16 mm diameter transducers that emitted audible sound (10 kHz;  $\lambda \approx 34.4$  mm). It is important to note that Zhang et al. (2014) managed to reconstruct self bending beams only by using transducers smaller than half of the wavelength. The work demonstrates how the curved trajectory is designable from any uniformly curved arc, but it is inappropriate for HCI purposes, as it produced an audible and constant high pitch sound at 10 kHz. Li et al. (2014a) implemented self-bending beams using MMs, but these were still limited to the audible frequency range (3.4 kHz).

SoundBender, extends prior work, as shown in Table 3.1, by demonstrating a hybrid technique (a combination of a static MM and a PAT) at 40 kHz frequency, which is beyond the audible sound range for humans, and features three advanced functions: 1) the creation of either levitation or tactile points beyond occluding objects; 2) the dynamic 3D reconfiguration of the sound field (using the phased array to reconfigure the points); 3) a structured method to create such hybrid modulators.

Following the technique described by Zhang et al. (2014), this chapter designed a curve  $x = f(z)$  using the cubic Bezier function with four control points (see Figure 3.5). If  $(x_i, z_i)$  are the coordinates of the Bezier points and  $t \in [0, 1]$ , the curve in parametric form was determined as in Equation 3.1 and 3.2 below:

$$x(t) = h(t) = (1 - t)^3 x_0 + 3t(1 - t)^2 x_1 + 3t^2(1 - t)x_2 + t^3 x_3 \quad (3.1)$$

$$z(t) = g(t) = (1 - t)^3 z_0 + 3t(1 - t)^2 z_1 + 3t^2(1 - t)z_2 + t^3 z_3 \quad (3.2)$$

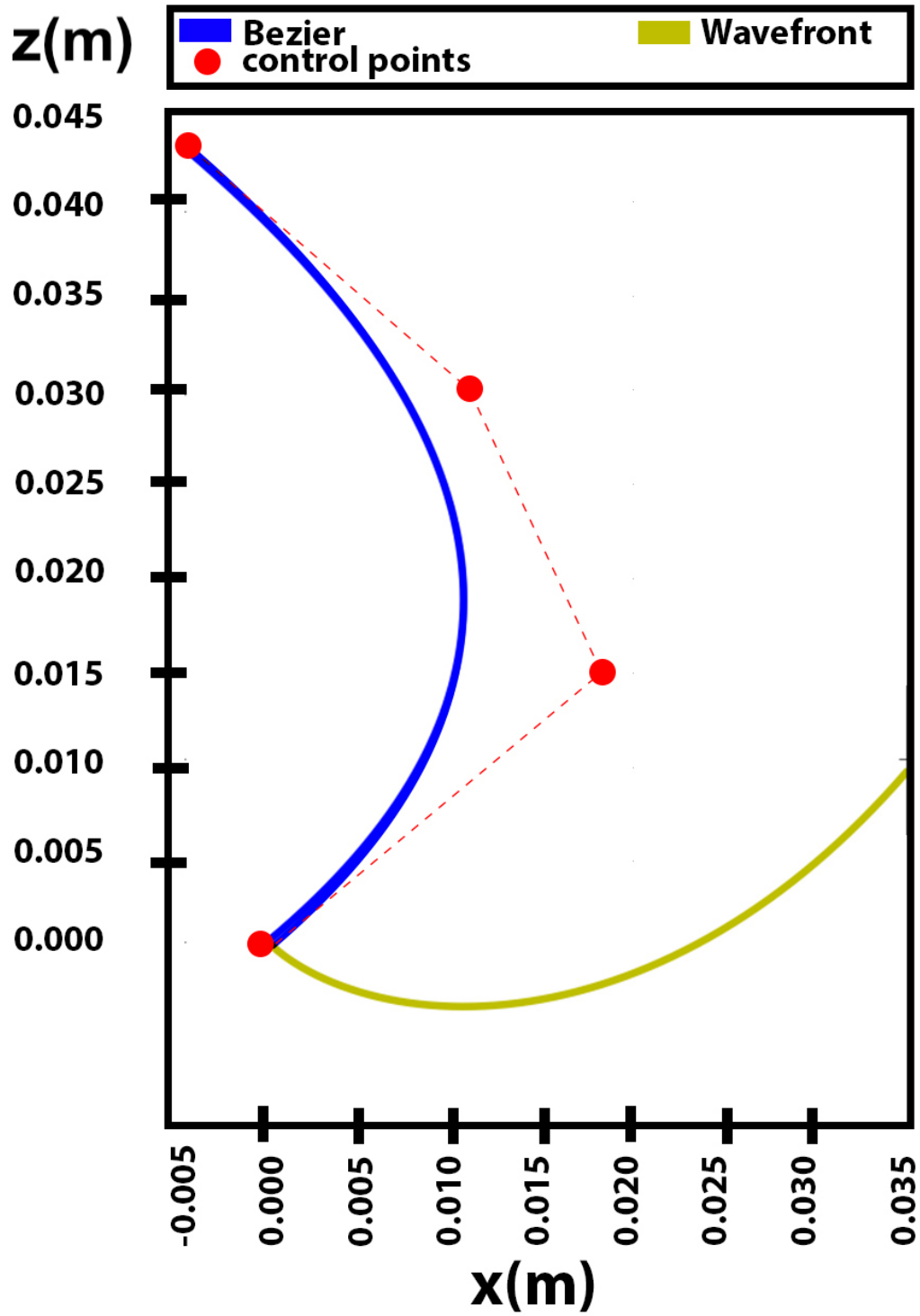


Figure 3.5: Pre-designed Bezier curve. Highlighted in the image are the four control points (red dots), the parametric Bezier (blue line), and the wavefront necessary to achieve it (yellow line). Acoustic radiation propagated towards the Z-axis direction.

Table 3.1: Related approaches and relevant features.

Transducers Arrangement	Field Control	Spatial Resolution	Obstacle Avoidance
Transducer pair (Brandt, 2001; Ochiai et al., 2014)	Dynamic (reduced)	Low	N/A
Transducer array (Long et al., 2014; Omirou et al., 2015, 2016)	Dynamic	Low	N/A
Metamaterial (Memoli et al., 2017)	Static	High	N/A
Hybrid approach (SoundBender)	Dynamic	High	Dynamic

Consequently, the function  $f$  is defined as in Equation 3.3 below:

$$f = h(t) \cdot g(t)^{-1} \quad (3.3)$$

After computing  $f'(z)$  and  $f''(z)$  using the quotient rule, the approximation of the geometrical wavefront  $(u(x, z), v(x, z))$  perpendicular to the acoustic source was computed using ray acoustics theory, as shown in the equations below:

$$u(z) = \frac{I(z) + C(z_0)}{\sqrt{1 + f'(z)^2}} - \frac{f'(z) \cdot (f(z) - z \cdot f'(z))}{1 + f'(z)^2} \quad (3.4)$$

$$v(z) = \frac{f'(z) \cdot I(z) + C(z_0)}{\sqrt{1 + f'(z)^2}} + \frac{f(z) - z \cdot f'(z)}{1 + f'(z)^2} \quad (3.5)$$

where

$$I(z) = \int \frac{(f(z) - z \cdot f'(z)) \cdot f''(z)}{(1 + f'(z)^2)^{\frac{3}{2}}} dz \quad (3.6)$$

$$C(z_0) = \frac{z_0 + f'(z_0) \cdot f(z_0)}{\sqrt{1 + f'(z_0)^2} - I_0} \quad (3.7)$$

Equation 3.8 then mapped x-coordinates for the wavefront onto a plane at  $z = 0$ , and Equation 3.9 was employed to compute the phase delay associated with the x-coordinate.

$$x = v + u \frac{du}{dv} \quad (3.8)$$

$$\phi(x) = \frac{ku}{\cos(\arctan(-\frac{du}{dv}))} \quad (3.9)$$

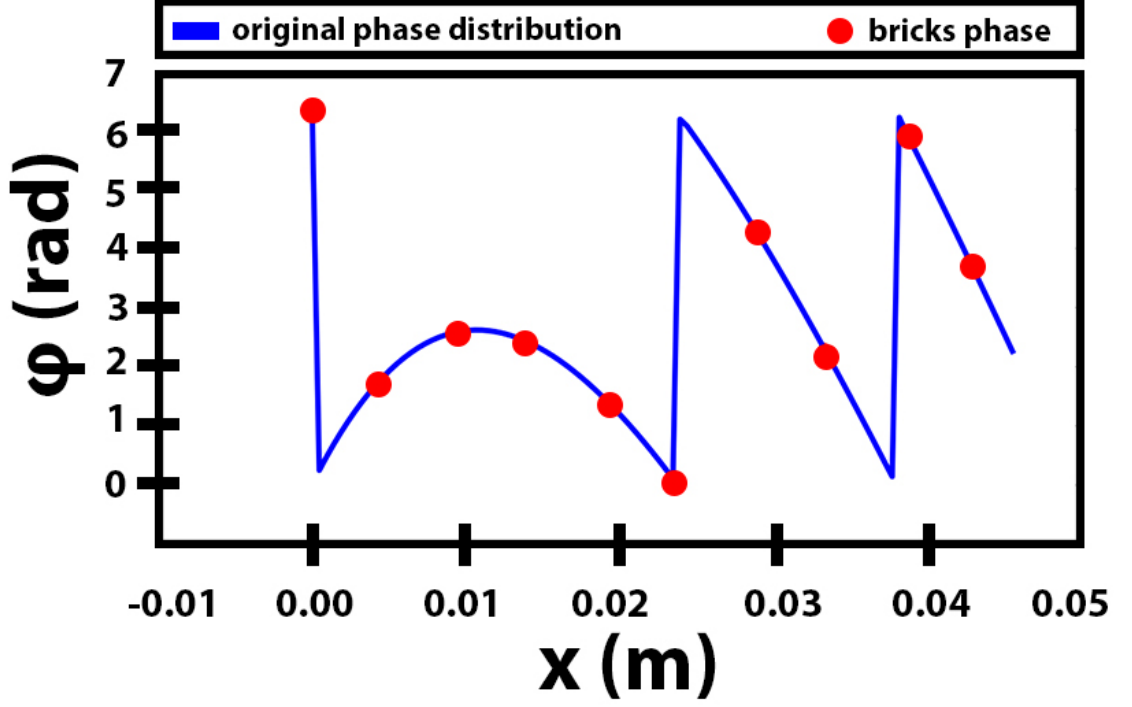


Figure 3.6: Phase distribution and sampled phase of the bending sound field.

where  $k = \frac{2\pi}{\lambda}$  is the wavenumber.

Since  $\lambda/2$  was the fundamental limit for sampling and reconstructing data without losing its original shape, therefore, x-coordinates were sampled based on their association to the phase based on the Nyquist theorem suggestion (Nyquist, 1928),  $\lambda/2$ . An example of the sampling data is shown in Figure 3.6.

Zhang et al. (2014) used back-propagation to Fourier-transform the phase  $\phi(x, 0)$  into  $\phi(x, -z_0)$ , in effect moving the Bezier curve at a distance from their transducer array, and assigning on it a more complex phase distribution. This study decided instead opted to exploit a formula already known by its use in holographic optical tweezers and Fresnel lenses (Salter et al., 2013; Pesce et al., 2015), as denoted in Equation 3.10. It encodes the phase distribution for each transducer  $(i, j)$  after the Fresnel lens shifts a reference point  $z$  to a new  $z$  value, denoted as  $\Delta_z$  in the equation. This cause the sound field to expand up or down. In the equation below,  $\lambda$  is the wavelength of the sound, and  $x_i$  and  $y_j$  are the Cartesian coordinates on the phased array.

$$\phi(i, j) = \underbrace{\frac{\pi \cdot \Delta_z}{\lambda \cdot z^2} (x_i^2 + y_j^2)}_{\text{Fresnel lens}} \quad (3.10)$$

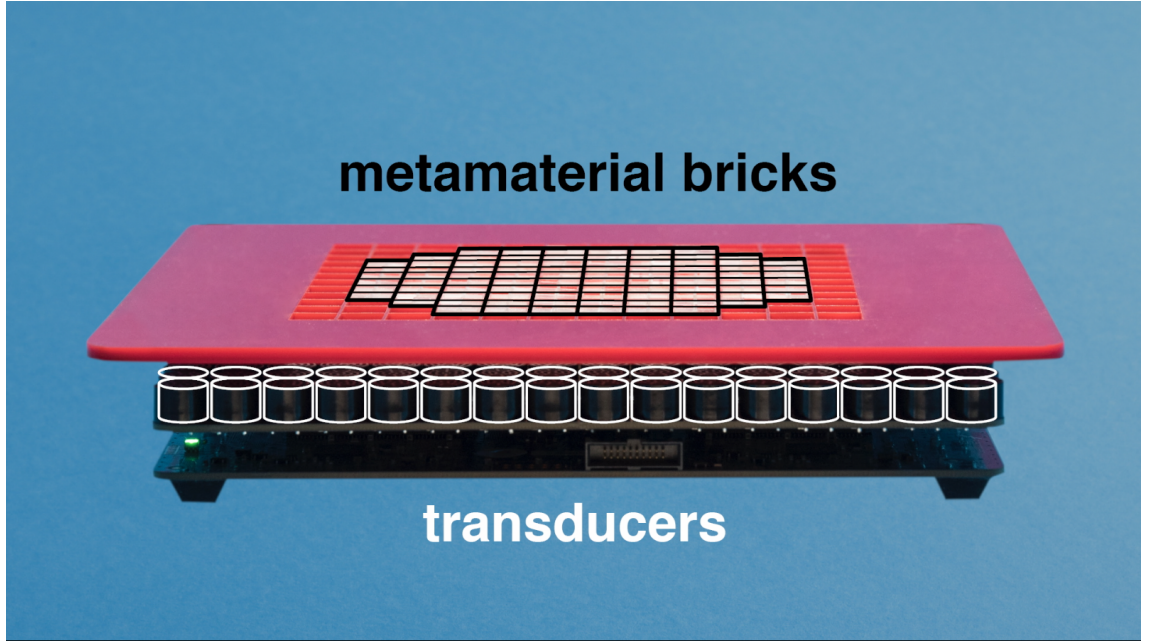


Figure 3.7: The experimental setup used in this study.

### 3.3.1 Materials and method

The initial SoundBender setup (see Figure 3.7) consists of two main parts: an array of MM bricks, assembled as a metasurface, and a PAT, operating at 40 kHz. In this setup, the static MM bricks will create the complex sound field (i.e., self-bending beams), just on top of the metasurface, and the PAT will reconfigure the sound field by shifting a reference point up or down. The PAT used in this study is an Ultrahaptics board (Ultrahaptics, Bristol, version 2.0.0) consisting of 16 x 16 of 40 kHz close-packed transducers (radius: 5 mm, lateral separation: 10.5 mm, nominal emission: 120 dB). The board was programmed with SDK version 1.2.4., using an in-house control software, written in C++ language (programmed using xCode version 8.3.2). Figure 3.8 provides a closer look at the transducers array.

There are no transducers with a size of half the wavelength of 40 kHz (4.3 mm). This study therefore refers to a work that produced phase delays similar to half-wavelength transducers through acoustic MM bricks (Memoli et al., 2017). Memoli et al. (2017) studied 16 types of bricks, all optimised for high transmission at 40 kHz, and each encoding a different phase delay between 0 to  $2\pi$  (Memoli et al., 2017). The bricks were produced by rapid prototyping (ProJet HD 3000 Plus printer), and the labyrinthine features inside them were at the resolution limit of the printer. A laser-cut acrylic was used to hold a 24 x 24 grid of the bricks, as in Figure 3.9, using Universal Laser System VSL version 2.3

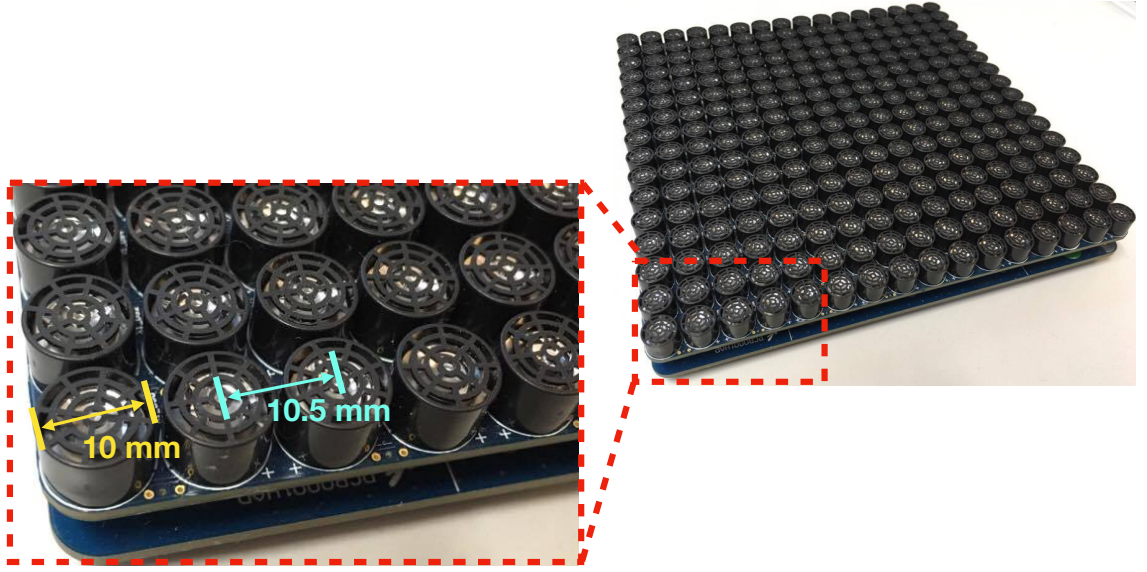


Figure 3.8: Phased array transducer spatial spacing.

A customised Python program (written in Python 2.7) was used to compute the phase delay and bricks samples required to create the self-bending beam. Figure 3.6 shows a sampling output. In order to design a radial curve, a distance between the the central axis of the grid in Figure 3.9 was computed and assimilated to the  $x$ -coordinate in Figure 3.6. The quantisation of the metasurface in the phase domain was achieved by selecting the brick with the nearest phase to the desired phase. This arrangement produced an axisymmetric self-bending beam sound field, as shown in Figure 3.10.

### 3.3.2 Results

#### 3.3.2.1 Simulations and measurement

This study carried out a 2D sound field simulation in COMSOL Multiphysics (COMSOL, Cambridge, UK, version 5.2a). The simulations ran on an iMac workstation (3.4 GHz Intel Core i5 processor, 16GB DDR3 RAM, macOS Sierra version 10.12.5). Figure 3.11 A1 specifically shows the simulated SPL of the phase distribution in Figure 3.6. Simulations were verified using a scanning system built in-house, based on a commercial 3D printer setup and piloted by a C++ custom code. Measurements were taken, with readings acquired using a B&K microphone (model 4138-A-015) via a conditioning amplifier (NEXUS, final gain of the chain: 3.16V/Pa), using a PicoScope (Pico Instruments, model: 5444b) that employed the following: preamplifier(Amp) = -20 dBV; mic sensitivity(S) = -60 dBV/Pa;  $P_{ref} = 20\text{e-}6$ . For each step (j), this study recorded  $N = 4,096$  mV samples, then computed the pressure (denoted as  $P_j$  in Equation 3.11) and its SPL, denoted as



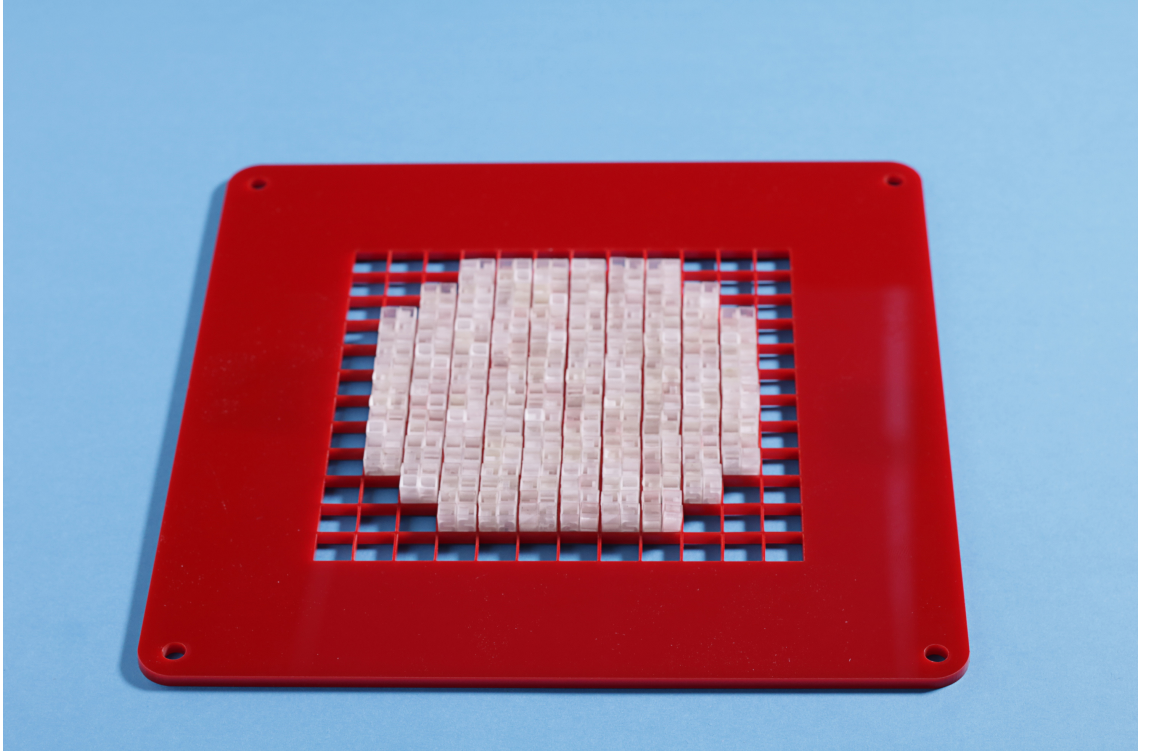


Figure 3.9: MM arrangement for encoding the self-bending beam sound.

$SPL_j$  in Equation 3.12.

$$P_j = \frac{V_{rms_j}}{Amp} \quad (3.11)$$

$$SPL_j = 20 \cdot \log_{10} \frac{P_j}{P_{ref}} \quad (3.12)$$

where

$$Amp_{(dB)} = 10^{\frac{|Amp|}{20}} \quad (3.13)$$

$$S_{(mV)} = 10^{\frac{S}{20}} \cdot 10^3 \quad (3.14)$$

$$V_{mean_j} = \frac{\sum_i^N V^2}{N} \quad (3.15)$$

$$V_{rms_j} = \frac{\sqrt{V_{mean_j}}}{Amp} \quad (3.16)$$

Figure 3.10 provides scans (4 mm resolution) across the  $XY$ -plane at different heights ( $z=20$  mm, 30 mm, and 40 mm, respectively) for a quick comparison. All the three sliced



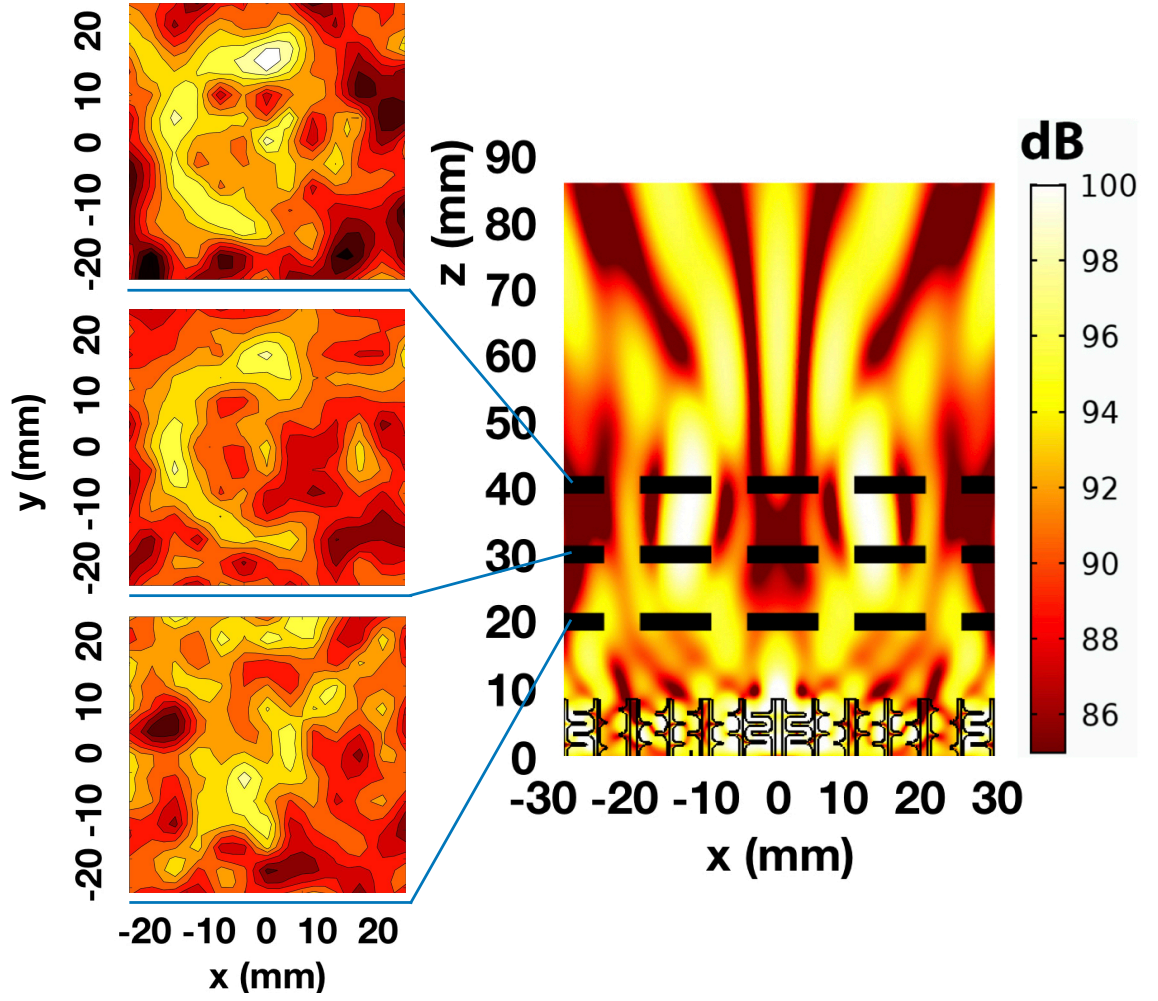


Figure 3.10: Bent beam simulation and measurement results of the present study: (right) simulation result of an axisymmetric bent beam on the  $XZ$ -plane; (left) scans (4 mm resolution) of the bent beam were taken across the  $XY$ -plane at different heights:  $z = 20$  mm(bottom left),  $z = 30$  mm (middle left), and  $z = 40$  mm(top left).

plane confirmed the desired bending, but also indicated leaking of acoustic energy along the axis. This leaking issue occurred as a result of the parallelism problem between the transducer array and the planar structure that holds the bricks. Another cause was the axisymmetric holding structure itself; some of the bricks were slightly misaligned due to manufacturing errors. Figure 3.12 shows a quick visualisation of the acoustic field using solid  $CO_2$  (i.e., dry ice). The vapours produced during sublimation highlighted the lines of the field, which was particularly useful when the Bezier curve was reconfigured using the transducer array.

### 3.3.2.2 Experiments with levitated object displacement

Figure 3.11 reports a summary of experiments on the sound field of the axisymmetric self-bending beam. The experiments showed that the axisymmetric beam resulted in a high-pressure region at the end of the bent beam trajectory, and that an object could be trapped on top of the high-pressure region (as in Figure 3.11, row (1)). The region was able to levitate objects due to the surrounding high-intensity sound field. The following section presents the results of the reconfiguration algorithm (i.e., stretching the bent beam), which was observed from the successful levitation. Since the algorithm included only Fresnel lens (as in Equation 3.10), there was an expectation that this experiment would note changes in the vertical displacements of the levitated objects.

The results includes both simulated and its experimental measurements, which can be seen in Figure 3.11. Figure 3.11, row (1) (column A–C) shows that the Bezier curve endpoint (i.e., the intensity of the high-pressure region) moved upwards from  $z = 10$  mm to  $z = 20$  mm. This simulation was confirmed by the measurements in Figure 3.11, row (2) (column A–C), where the Bezier curve endpoint also moved upwards. Figure 3.11, row (3) (column A–C) demonstrates the reconfiguration of matter in the mid-air using the proposed algorithm.

### 3.3.2.3 Levitation of various objects

To test the capability of the ultrasonic approach to reconfigure different types of matter in free air, this study tested the levitation object of various materials, as shown in Table 3.2. The experiment used paper, cardboard and ABS, all with a common weight of 5 mg, and the setup managed to levitate the objects of one wavelength length. This study also observed that, as the volume of the levitated object increased, the height of the object in the air decreased. This behaviour was anticipated. The pressure needed to levitate

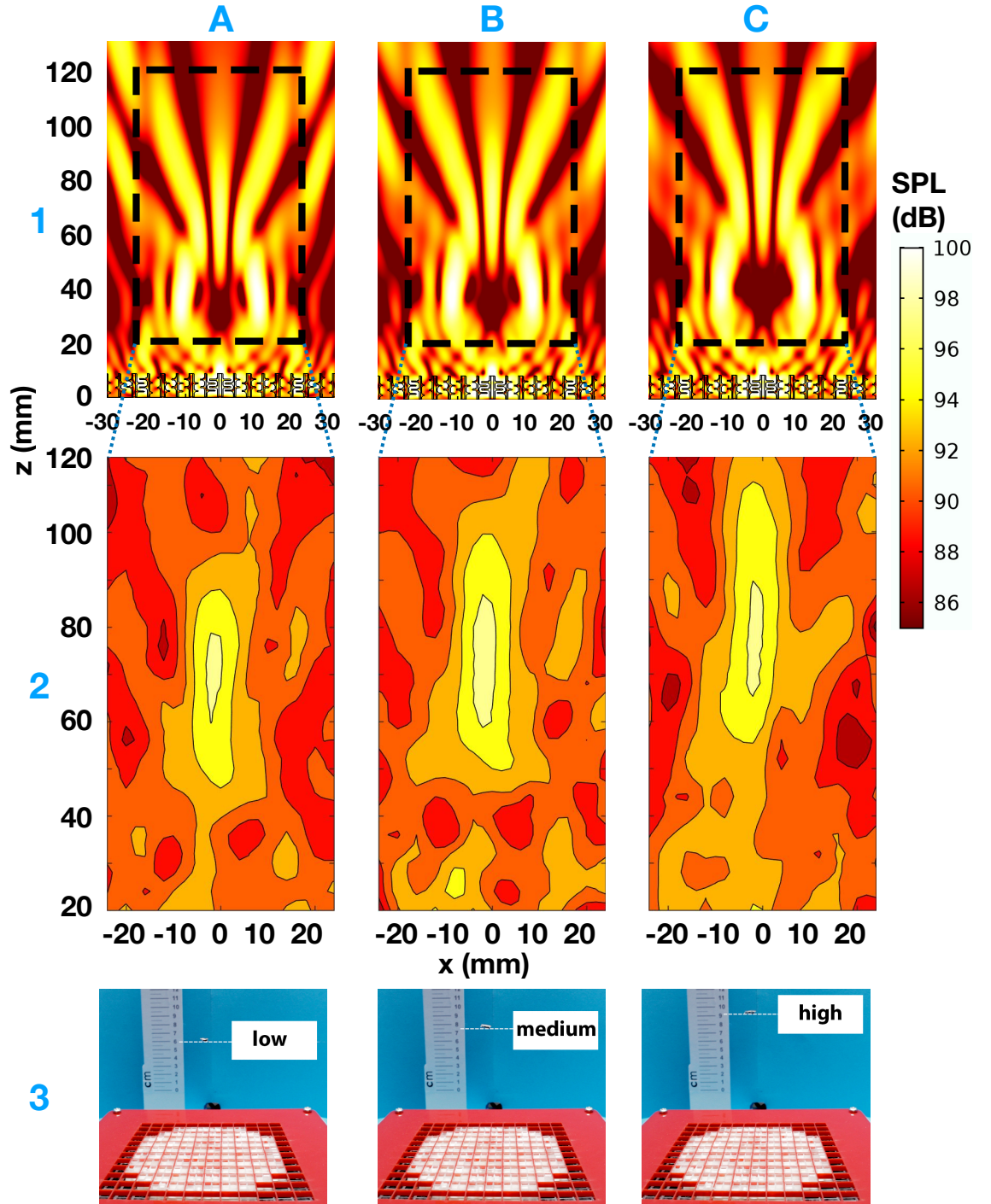


Figure 3.11: Simulation and measurement of trap displacement by using Equation 3.10, row (1) shows simulation results of trap displacement; row (2) shows the measurement results of the trap displacement; row(3) shows actual tests for the levitation trap. Column (A) is the initial position of the trap; column (B) is the trap displaced to positive 5 mm in the  $Z$ -axis direction; column (C) is the trap displaced to positive 10 mm in the  $Z$ -axis direction.

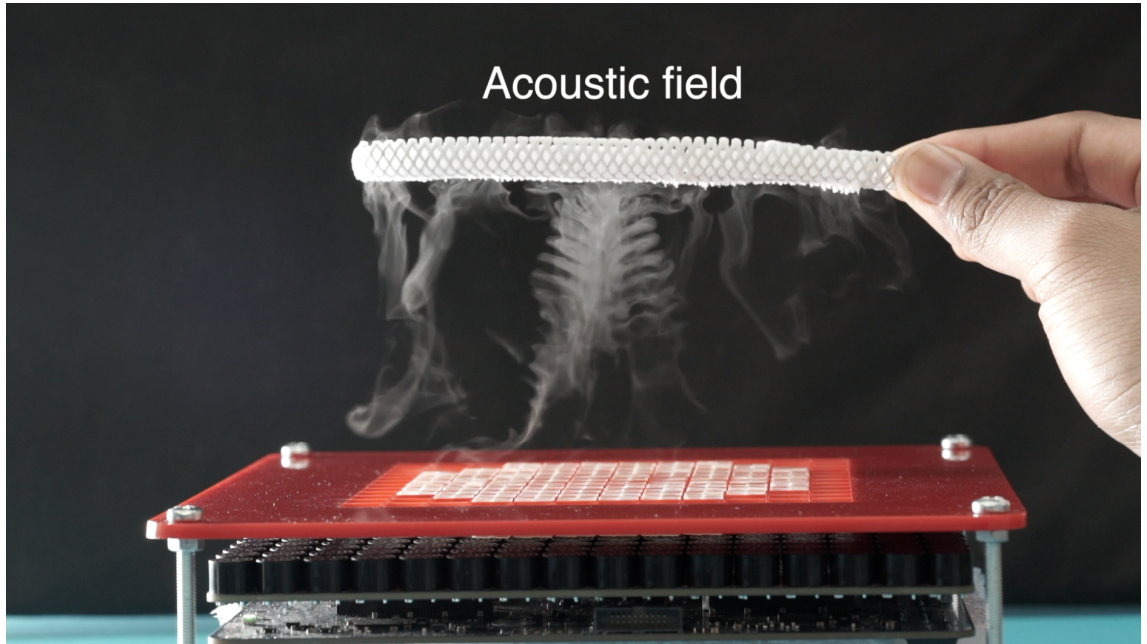


Figure 3.12: Visualisation of a self-bending beam using dry ice.

an object depends primarily on its density; therefore, objects with higher pressure moved closer to the high-pressure core below the trap, where the acoustic force was large enough to balance their density.

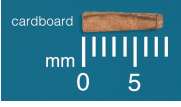
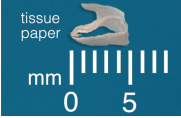
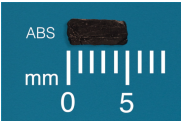
This preliminary work presented a hybrid ultrasound technique that combined a PAT and MM. The work undertook numerical simulations and experimental measurements of matter reconfiguration through a hybrid technique, a combination of PAT and MM, and demonstrated an ability to reconfigure different types of matter in mid-air. However, the preliminary work only described object reconfiguration in a single axis (i.e., the  $Z$ -axis or height) in free air. The following sections will describe the study in full, including a description of the formula used to reconfigure matter in all three axes. Furthermore, the misalignment of the MM and PAT was found to be a factor that impacted the acoustic field, thereby caused instability during levitation. Consequently, the full study will also include a description of better control over this factor.

### 3.4 SoundBender: Hybrid sound modulators and dynamic self-bending beams

This section presents SoundBender (illustrated in Figure 3.1) in a study of a hybrid modulator that combines a PAT and acoustic MM, which employ a novel technique to reconfigure matter in mid-air. The MM provides a smaller modulator pitch, which although static, is



Table 3.2: Various levitated materials

Object	Dimension (mm)	Estimated Density ( $\text{kg m}^{-3}$ )	Weight (mg)	Levitation Height (cm)
 cardboard	8 x 2 x 2	156	5.0	88
 tissue paper	5 x 2 x 2	250	5.0	80
 ABS	5 x 2 x 2	286	5.0	78

key to creating high-fidelity sound fields. The PAT adds dynamic amplitude/phase control of the field at a higher pitch.

The main contributions of this study includes its description of a technique for implementing such hybrid modulators and its reconfiguration algorithm, which drawn on acoustics and MM techniques. The following subsections describe the primary steps of the hybrid technique: *(i)* computation of the self-bending curve; *(ii)* computation of the transducers' phases to recreate the sound field; *(iii)* discretisation into 3D printable bricks and fabrication of the metamaterial; *(iv)* modulator spacing and coupling; *(v)* the PAT: algorithms employed for dynamic control. The following subsections detail each of these five steps. Please note that the study illustrates the proposed technique by encoding a self-bending beam into the MM. This allowed the technique to place passive props (such as decorative features and toys) on top of the hybrid modulators, while still creating dynamic control points (e.g., movable levitation traps or tactile points) above the prop. The first two steps described below are specific to self-bending beams. However, the other steps can be applied in other scenarios, and step *(ii)* provides suggestions for aiding in application to other sound fields. These steps have been tested and were successful at precisely reconfiguring different sound fields, as described in the Chapter 4.

### 3.4.1 Step (i): computation of the self-bending curve

The self-bending beam must wrap around the passive prop located on the MM (see Figure 3.13 (a)) to avoid disruption such as energy scattering from the prop's surface, and distortion of the sound field. To achieve this, a convex hull was computed to fit the prop.

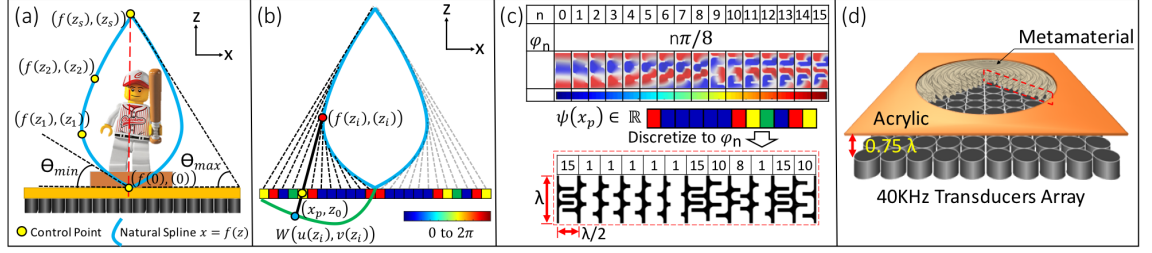


Figure 3.13: Method summary: (a) the technique first identified a small number of points around the prop and computed a curve/spline; (b) the technique computed the phases producing a self-bending beam from this spline; (c) the technique discretised phases using a set of MM bricks; (d) final MM and the SoundBender setup.

Each point of the convex hull had to be at least  $\lambda/2 \approx 4.3$  mm away from the prop, due to the thickness of the beam itself. Additional space was allowed when the beam was dynamically changed (e.g., if tactile/levitation points were moved up or down or sideways), as described later in step (v).

Later, a natural splines technique (Catmull and Rom, 1974) was used to compute the desired curve ( $x = f(z)$ ) from the  $S$  points on the convex hull ( $f(z_i), z_i$ ), as shown in Figure 3.13 (a). It should be noted that both the starting and end points must lie on the central axis of the material ( $xy = 0$ ). The convex hull must avoid points lying less than  $\theta_{min} = 30$  degrees from the horizontal plane (i.e., outside of the directivity pattern of the transducers used). This  $\theta_{min}$  was used as the orientation for clamping the starting point ( $f(z_0), z_0$ ) of the spline. The end point ( $f(z_s), z_s$ ) was clamped at an angle connecting the point to the final cell in the MM ( $\theta_{max}$ ). In addition, the projection of the curve tangents on the MM (the black lines in Figure 3.13 (b)) had to be injective (i.e., two tangents could not reach the same point  $x_p$ ).

### 3.4.2 Step (ii): computation of phases to recreate the sound field

Step (i) allowed the computation of a spline path that closely wrapped the object's shape. This step simplified the equation by Zhang et al. (2014)<sup>2</sup> for computing the phases of a self-bending beam following such a path. Equations for computing the phases are reported below. First, the phase delays for the self-bending beam were computed and encoded by

<sup>2</sup>The simplified equations are still equivalent to those in (Zhang et al., 2014). Simplification is possible as the first point is  $P(0, 0)$ , resulting the term  $C(z_0)$  becoming zero. All derivatives were made relative to  $z$ , using the chain rule. First order and second order derivatives (e.g.,  $f'(z)$  and  $f''(z)$ ) were easily numerically approximated using central differences.

the sound sources along the  $X$ -axis on a 2D plane ( $XZ$ ) (see Figure 3.13 (b)). Next, it revolved the one-dimensional (1D) phase profile and became as phases of the 2D MM (see Figure 3.13 (d)).

Let  $x = f(z)$  be the spline path and let  $P(f(z), z)$  be points along this spline ( $z \in [0, z_s]$ ). For each spline point  $P(f(z), z)$ , a matching point  $W(u(z), v(z))$  on the wavefront producing a caustic tangent to the spline was computed:

$$u(z) = \frac{I(z)}{\sqrt{1 + f'(z)^2}} - \frac{f'(z) \cdot (f(z) - z \cdot f'(z))}{1 + f'(z)^2} \quad (3.17)$$

$$v(z) = \frac{f'(z) \cdot I(z)}{\sqrt{1 + f'(z)^2}} + \frac{f(z) - z \cdot f'(z)}{1 + f'(z)^2} \quad (3.18)$$

$$I(z) = \int \frac{(f(z) - z \cdot f'(z)) \cdot f''(z)}{(1 + f'(z)^2)^{\frac{3}{2}}} dz \quad (3.19)$$

Then, the caustic wavefront  $W$  (Figure 3.13 (b)) was projected onto the MM plate. The points  $W(u(z), v(z))$  were then projected to a position  $x_p(z)$  with phase  $\psi(x_p(z))$  as follows:

$$x_p(z) = v(z) + u(z) \cdot \frac{u'(z)}{v'(z)} \quad (3.20)$$

$$\psi(x_p(z)) = \frac{2\pi}{\lambda} \cdot \frac{u(z)}{\cos(\arctan(\frac{u'(z)}{v'(z)}))} \quad (3.21)$$

Note that each point of the curve  $P(f(z), z)$  resulted in a position  $x_p(z)$  and phase  $\psi(x_p(z))$  along the  $X$ -axis. This explains the need for the projected tangents to be injective (i.e., no two tangents projected to the same  $x_p$ ).

The next step transformed the current 1D profile (phases along the  $X$ -axis) into a 2D plane. This was achieved by revolving the profile along the  $Z$ -axis, creating an enclosed self-bending volume. Thus, the phase for any point  $(x_p, y_p, 0)$  on the MM plate is computed in Equation 3.22 as follows:

$$\psi(x_p(z)) = \psi(\sqrt{x_p^2 + y_p^2}) \quad (3.22)$$

Although steps (i) and (ii) above were specific for the recreation of self-bending beams, the hybrid modulators could be created with the MM encoding other sound fields (e.g., a multipoint field, as by Long et al. (2014), or generic holographic approaches, as by Okada

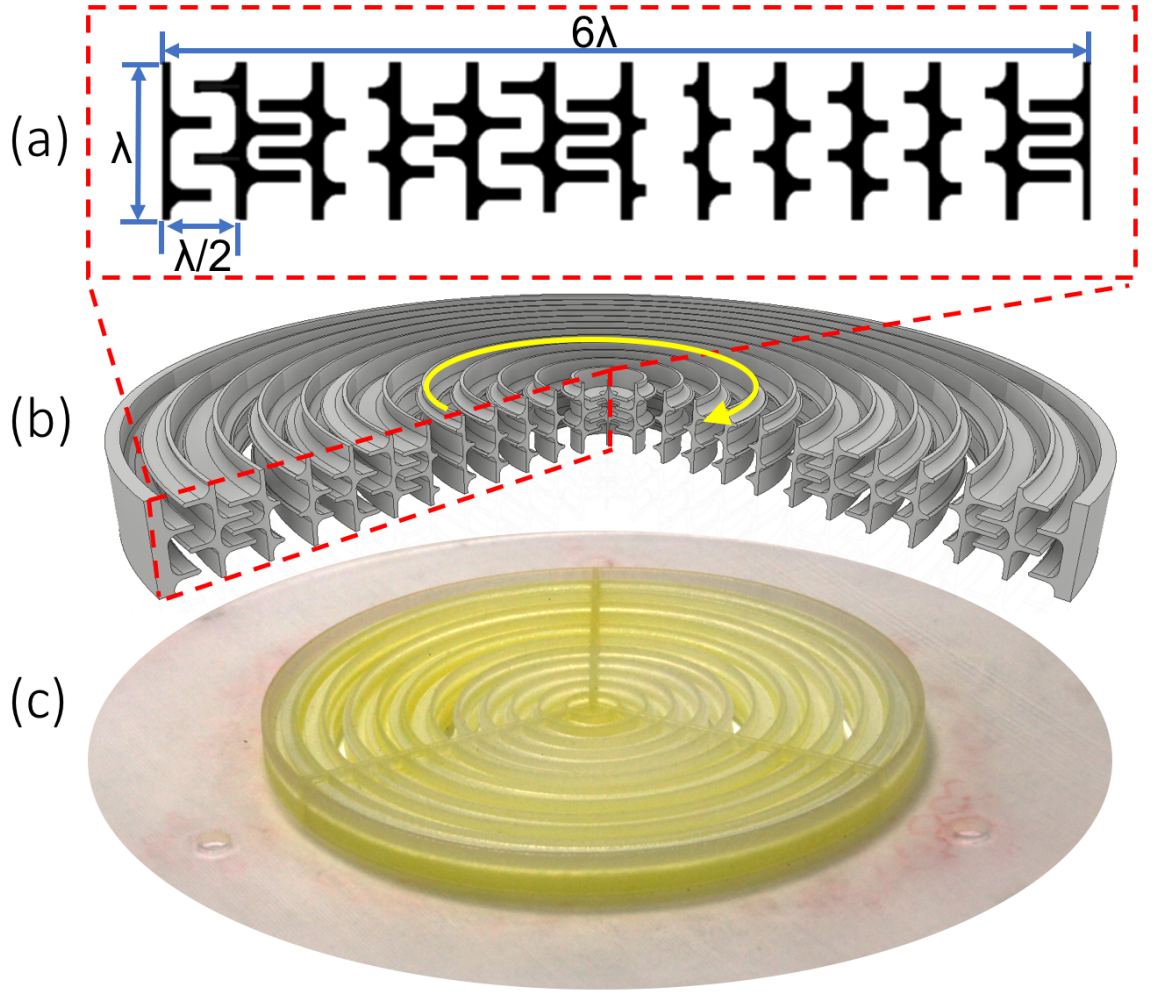


Figure 3.14: Metamaterial 3D Printing Model: (a) 2D drawing of encoded metamaterial bricks; (b) 3D Sliced view of metamaterial model after revolving the 2D drawing sketch; (c) Final 3D printed metamaterial (with support base).

et al. (2013). Regardless, the following steps can be reused with other sound fields, as long as the phase  $\psi(x_p, y_p)$  for any point on the MM surface is known.

### 3.4.3 Step (iii): discretisation and fabrication of the metamaterial

The phase distribution  $\psi(x_p, y_p)$  above, describes the phase required at each point  $(x_p, y_p, 0)$  on the modulator's surface (i.e., the MM surface). To encode the MM surface, this step then discretise  $\psi(x_p, y_p)$  using the set of 16 MM bricks ( $\phi = 16$ ) proposed by Memoli et al. (2017). These bricks are optimised for high transmission at 40 kHz, and each one encodes a different phase delay (between 0 to  $2\pi$ ) as shown in Figure 3.13 (c). Such bricks have a thickness of  $\lambda$ , and a lateral dimension (i.e., pitch) of  $\lambda/2 \approx 4.3$  mm, fitting the size requirements of the present study. To discretise the continuous phase distribution  $\psi(x_p, y_p)$ ,



this step sampled the 2D plane using a separation of  $\lambda/2$  (i.e., the size of a brick), and rounded the phase to the closest value in the brick set  $\phi$  16 (bricks and phase values can be seen at the top of Figure 3.13 (c)).

This step is generic and applicable to any sound field distribution. For axisymmetric phase distributions (such as the self-bending beams), a more accurate alternative is to encode the phase from the original 1D profile  $\psi(x_p)$  by revolving it (the red outline in Figure 3.13 (d)) around the  $Z$ -axis. This will provide a continuous approximation to all points on the same ring, reducing discretisation to the radial direction.

This was done as shown in Figure 3.14 (a). First, the encoded bricks were aligned MM without gaps, shown in a 2D sketch. Second, this sketch was revolved (see Figure 3.14 (b)) in a 3D modelling software, (e.g., Autodesk Inventor Professional 2017). Finally, the 3D model from the revolve process was fabricated into a 3D print model using a high-precision 3D printer (e.g., ProJet HD 3000 Plus printer) and VisiJet EX200 material (high-tensile strength). The precision of the 3D printer is critical for reproducing the original phase distribution, as the size of the bricks required by the Nyquist theorem (Nyquist, 1928) (4.3 mm) is at the limit of the possible printing resolution. High-tensile strength ensures acoustic radiation is transmitted (and not absorbed) by the MM. Figure 3.14 (c) shows the final MM, including a support base for ease of assembly.

#### 3.4.4 Step (iv): modulator spacing and coupling

A gap will exist between the MM and the PAT, and the size of this gap will impact the performance of the hybrid modulator, as described and analysed below. A small gap will produce an uneven distribution of acoustic pressure across the MM surface, stronger for bricks directly in front of a transducer, but weaker for bricks between transducers. In contrast, a larger gap will provide a more even distribution, but the thickness of the modulator will increase, and power will be lost due to the sources are farther apart, and each brick will receive contributions from more transducers (i.e., the phase of a brick is not ruled by the phase of the closest transducer, but by a group of them). This final issue can affect the effectiveness of the dynamic control techniques described in the next section.

This step analysed the effect of various gap sizes, as illustrated in Figure 3.15 (all pressure values relative to the transducer's pressure at 1 m ( $P_{ref}$ )). First, this step modelled the pressure distribution created by a section of 5 x 5 transducers at various distances above the PAT (from  $0.5 \lambda$  to  $1.5 \lambda$ ). This step considered directivity extracted from Kota and Nakatera (1996) work and attenuation with distance, and computed total pressure

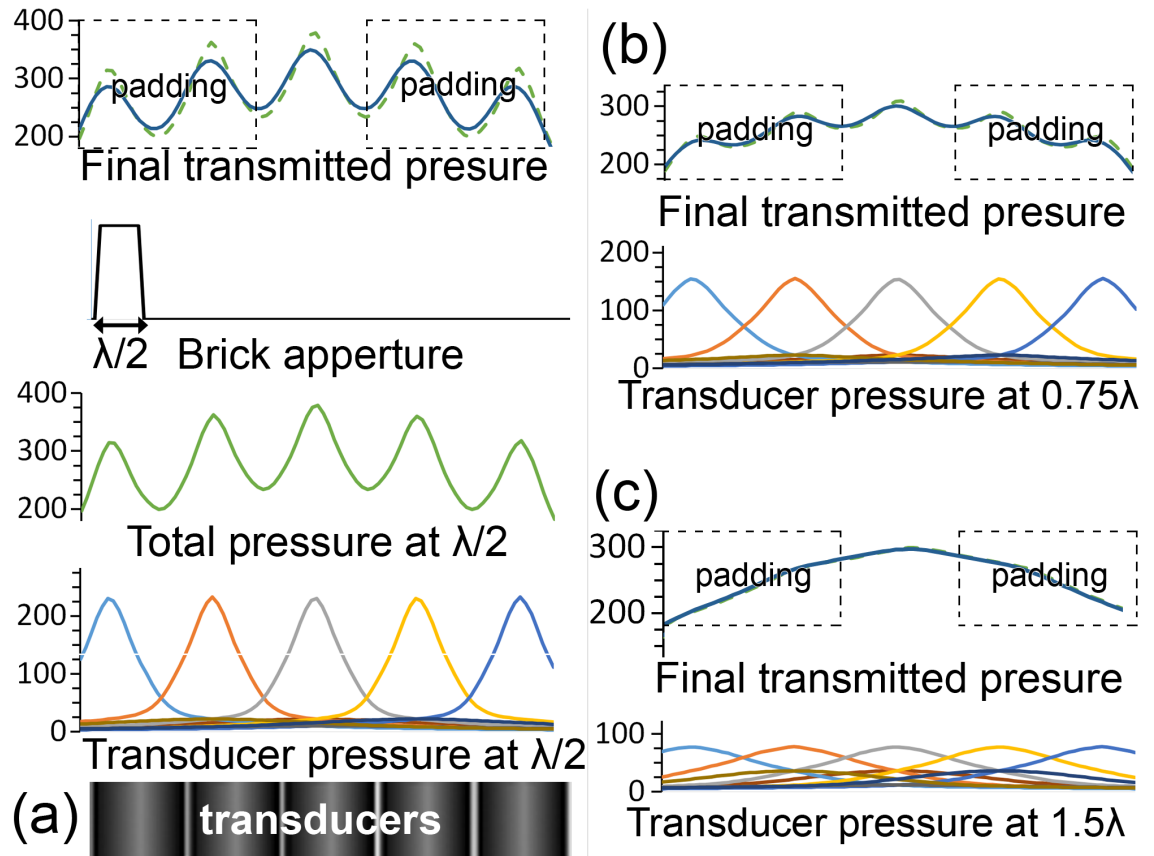


Figure 3.15: The effects of spacing between the PAT and MM: (a) pressure transmitted through the bricks with a  $\lambda/2$  gap, considering directivity, attenuation, and bricks' aperture size. A comparison follows of pressure with  $0.75 \lambda$  gaps (b) and  $1.5 \lambda$  (c).

distribution from the transducers used here at the target distance. This step could not assume specific positions for the bricks in front of the transducers, as the size of a brick is not a multiple of the transducer size; thus, it modelled the aperture of a brick as a rectangular function of size  $\lambda/2 \times \lambda/2$  (i.e., the size of a brick), computing the pressure transmitted through the brick as the convolution of the signal and its aperture.

This analysis illustrates the tendencies introduced earlier. Figure 3.15 (a) illustrates a gap of size  $\lambda/2$  (i.e., the minimum distance for the acoustic wave to be transferred as a plane wave). Pressure across bricks varied unevenly, between 248 and 349  $P_{ref}$  (13 % coefficient of variation). This spacing, however, maximised the coupling of the phases of the array to the MM. In a best-case scenario, with the brick in front of a transducer, 66 % of the pressure will be derived from the closest transducer. In a worst-case scenario, with the brick in the gap between four transducers, 65 % of the pressure will be derived from the four transducers (i.e., the phase will receive contributions from the closest  $2 \times 2$  transducers). A bigger gap of  $1.5 \lambda$  (Figure 3.15 (c)) will provide a more even distribution (282–297  $P_{ref}$ ,  $\sim 1.6$  % variation). However, only a 27 % of the pressure will be derived from the closest transducer in a best case scenario, and at worst, only 58 % from the closest  $2 \times 2$  transducers. This analysis revealed that a gap of  $0.75 \lambda$  (Figure 3.15 (b)) will provide a good general solution to this trade-off; amplitude variation across the plane will remain homogeneous (265–300  $P_{ref}$ , 4.5 % variation), and amplitude contribution will remain focused, with 51 % being derived from only the closest transducer in a best-case scenario, and 68 % from the closest  $2 \times 2$  transducers at worst (i.e., between transducers).

Relevant insight can be gained from this analysis, which will be useful for designers exploring the use of hybrid modulators. First, the gradual change in the transducer’s contribution to each brick indicate that the gap will behave as a smoothing function, interpolating intermediate phase values from the lower resolution PAT. This indicates that phase distributions on the PAT should only use low frequency distributions, as sharp changes may be lost due to smoothing. While this is not an issue for the algorithms in step (v) (i.e., diffraction and the Fresnel lens represent low frequency functions), practitioners using control algorithms that require higher frequencies will likely need to minimise this gap. Second, a loss of power was observed at pressure distributions in front of the two leftmost and rightmost transducers (see ‘padding’ areas in Figure 3.15), which failed to receive contributions from transducers further to the left and right). To avoid this, it is recommended that a PAT larger than the MM plate be used, and ‘padding’ it with two extra rows of transducers. The central transducers will receive minimal contribution from

additional transducers. Thus, by padding with two extra transducers, distributions can be assumed to be periodical for the entire plate.

### 3.4.5 Step (v): algorithms for dynamic control through a PAT

The previous steps described the creation of the hybrid modulator; however, these steps will only allow for the recreation of the static sound field encoded in the MM. This step here describes the technique for reconfiguring this field dynamically, by using a PAT. Two types of reconfigurations were enabled: 1) the global displacement of the sound field; 2) switching between tactile feedback and levitation traps.

#### 3.4.5.1 Global displacement of the sound field

This reconfiguration exploited a combination of a diffraction grating and a Fresnel lens algorithm, similar to those used in the control of holographic optical tweezers (Salter et al., 2013; Pesce et al., 2015).

Let  $(i, j)$  be one of the transducers in the array, and let  $(x_i, y_j, 0)$  be its 3D position. Let  $P(0, 0, z_s)$  be the reference point in the sound field (e.g., see the top of the self-bending beam, in Figure 3.16). Let  $(\Delta x, \Delta y, \Delta z)$  be the displacement for application to this point. Then, each transducer phase  $\psi(i, j)$  was computed as follows:

$$\phi(i, j) = \underbrace{\frac{2\pi}{\lambda \cdot z} (x_i \cdot \Delta x + y_j \cdot \Delta y)}_{\text{Diffraction grating}} + \underbrace{\frac{\pi \cdot \Delta z}{\lambda \cdot z^2} (x_i^2 + y_j^2)}_{\text{Fresnel lens}} \quad (3.23)$$

The reconfiguration formula in Equation 3.23 is an extension of Equation 3.10. It adds a shearing function into stretch the stretch function in Equation 3.10. While correct for use in planar fields, as by Okada et al. (2013), the Fresnel lens effect will squash or stretch the sound field (Figure 3.16 (b)), and the diffraction grating will cause a shearing effect (Figures 3.16 (c) and (d)). Spline definition (as described in step (i)) must consider the following changes: the obstacle must fit inside the beam, even after steering/stretching effects.

#### 3.4.5.2 Switching between tactile feedback and levitation points

The proposed hybrid technique allows for the dynamic creation of both levitation traps and tactile feedback. Levitation traps can be created by overlying a signature as described by Marzo et al. (2015). For a square array of  $N \times N$  transducers, this can be easily

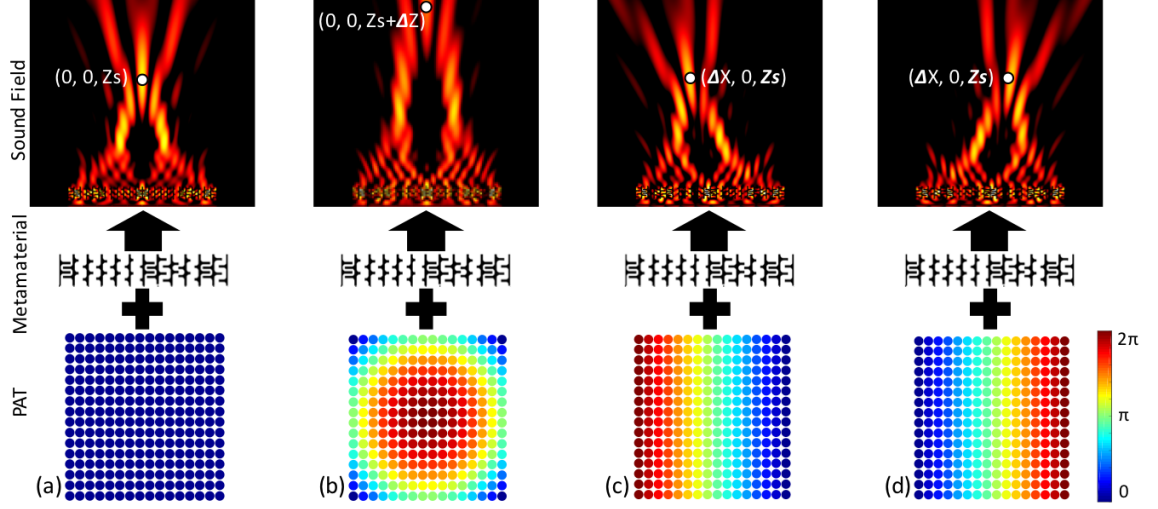


Figure 3.16: Using the proposed control algorithm for several displacements  $(\Delta x, \Delta y, \Delta z)$ : (a) no displacement; (b) vertical displacement,  $(\Delta z = 1 \text{ cm})$ ; (c) steering left  $(\Delta x = -1 \text{ cm})$ ; (d) steering right  $(\Delta x = 1 \text{ cm})$ . Note that all operations relied on smooth phase distributions.

implemented as an additional phase delay added to that in Equation 3.22, producing the final phase  $\psi_{lev}(i, j)$ :

$$\psi_{lev}(i, j) = \begin{cases} \psi(i, j) + \pi, & A_i \in [0, N/2). \\ \psi(i, j), & A_i \in [N/2, N - 1). \end{cases} \quad (3.24)$$

In addition, tactile effects can be created as described by [Carter et al. \(2013\)](#), by modulating the emitted signal (40 kHz) at 200 Hz. It must be noted that, when using this technique, all high pressure points in the field (i.e., points along the self-bending beam) will become simultaneously noticeable, unlike results found by [Long et al. \(2014\)](#). Coincidentally, the tests in this study revealed that both techniques can be applied simultaneously. The technique successfully levitated an object on top of an obstacle while modulating the signal. However this was achieved at the expense of halving both the strength of the levitation trap and tactile points, due to the levitation signature (i.e., only active 50 % of the time).

### 3.5 Experimental setup

The following sections will describe the evaluation of the approach to implement interactive features above the passive props placed on the sound modulator. These evaluations include

finite element method (FEM) simulations and real measurements, using an experimental setup. This section introduces both setups here and discusses the results obtained in the evaluation (section 3.6).

### 3.5.1 Finite element method simulation

The hybrid modulator was simulated using a commercial FEM software (COMSOL Multiphysics 5.2a) to observe the field they would recreate. In the simulations, the transmission medium was air (i.e., density  $1.21 \text{ kg/m}^3$ ; speed of sound  $343 \text{ m/s}$ ). The mesh elements of the models used were less than  $\lambda/8$  in diameter. To simulate the properties of a commercial transducer array (Ultrahaptics board, version 2.0.0), the simulation is included with a  $16 \times 16$  array of transducers (10 mm in diameter). The properties of each transducer were obtained from the manufacturer's description (muRata MA40S4S); was approximated as a cylindrical piston source emitting sine waves at 40 kHz, with sound pressure levels of 120 dB at 30 cm.

To simulate the 16 different types of discrete MM bricks, the shape of each brick as provided by Memoli et al. (2017) was replicated. Finally, the simulation fixed the MM (built as a combination of individual bricks) on top of the PAT, using a gap of 6.4 mm ( $0.75 \lambda$ ), as described in the previous section. Simulations were conducted on an iMac workstation (3.4 GHz Intel Core i5; 16 GB DDR3 RAM; NVIDIA GeForce GTX 780M).

### 3.5.2 Sound field measurement system

In order to measure the actual sound fields generated, a 3D sound field scanner system (see Figure 3.17) was built. A commercial 3D printer (Velleman k8200) was modified, in which the extruder was a fixed arm, holding a microphone. A PAT (Ultrahaptics board, phase controlled using Ultrahaptics SDK, version 2.2.1) and the MM were placed onto the measurement system, as described in step (iv) previously. It was important to ensure that the plate was parallel to the floor and the microphone is correctly aligned to the axis of the modulator (i.e., perpendicular to the MM).

Finally, G-code commands were used to control the printer's arm position, where the microphone was fixed. A custom-made C++ program was built to receive and record sound samples, and a delay of 0.5 s was included between the displacement end and the sampling, to keep displacement vibrations from affecting measurements. The setup captured samples of pressures by using a B&K microphone (model 4138- A-015), a conditioning amplifier (Nexus, final gain of -20 dB), and a PicoScope data acquisition unit, (Pico Instruments,

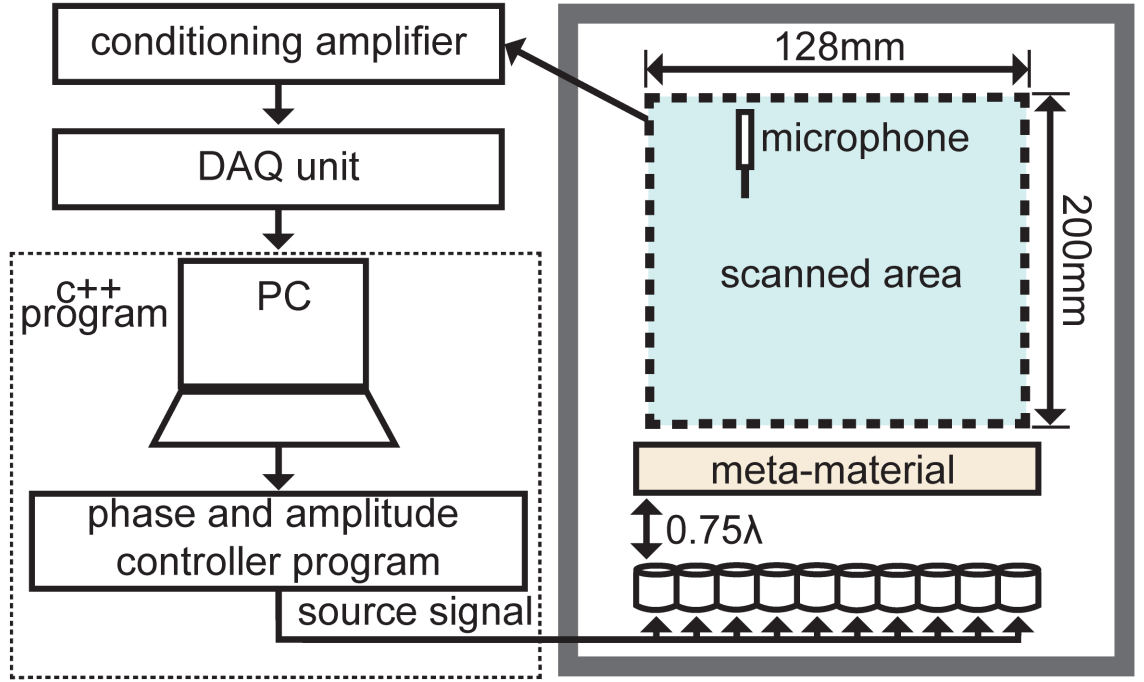


Figure 3.17: Schematic of the sound measurement system.

model: 5444b). Equation 3.12 was employed to compute the SPL, in dB, of the sound field pressures.

## 3.6 Evaluation

The validity of the proposed hybrid technique is considered in two stages. The first is an evaluation of the feasibility to recreate the intended sound field (i.e., the self-bending beam) at ultrasound frequencies (40 kHz). This was effected on both a commercial PAT and SoundBender. Second, is the evaluation on the reconfiguration ability of the proposed control algorithms, to dynamically modify the complex sound field (i.e., to stretch and steer the self-bending beam or to levitate) was evaluated.

### 3.6.1 Self-bending beam reconstruction

In order to test the need for the proposed hybrid technique, and as preliminary steps in this research, this section evaluates the feasibility of implementing the intended outcome (e.g., levitation/tactile feedback above a passive prop placed on top of the modulator) with simpler approaches. Figure 3.18 (a) shows a COMSOL simulation of the field resulting from the creating a focal point (similar to the one in Figure 3.2 (b)) in the presence of an obstacle (i.e., the passive prop). The simulation and measured tests showed that the

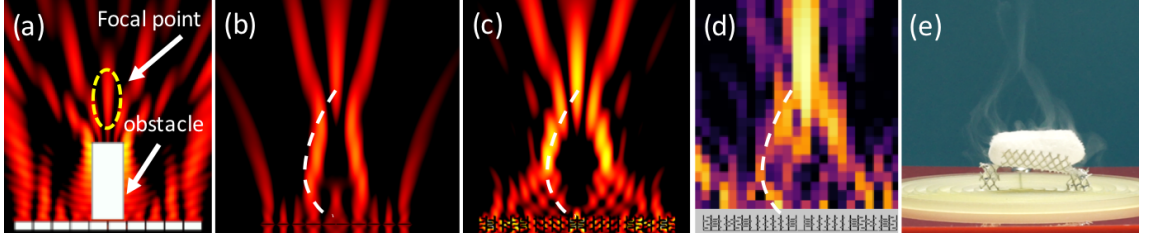


Figure 3.18: Sound field representation evaluation methods (a) an FEM simulation of PAT with an marked obstacle area where the control point should be; (b) an FEM simulation of a PAT attempt to create a curve (in white, dashed); (c) an FEM simulation of the hybrid SoundBender, showing the created curve (in white, dashed); (d) measurements of the SoundBender reproducing a self-bending curve; (e) a visualisation of the SoundBender creating self-bending beam with dry ice.

occlusion from the prop did not allow for a large amount of acoustic pressure to be focused at the intended location. Figure 3.18 (b) illustrates attempts to recreate self-bending beams using only a PAT where it shows how the PAT failed to reproduce a complex field (i.e., self-bending beams), even without the passive prop. First, due to aliasing effects (related to the larger modulator pits found in PATs) cause the created field to present low-fidelity acoustic pressure along the curvature beam, resulting in an inability to levitate objects in mid-air. This confirmed the predictions by Westervelt (1951), which states that the acoustic radiation force along the curvature beam will be insufficient for allowing levitation using a PAT only. Second, high pressure levels were detected inside the self-bending beam volume, where the passive prop should be located (near  $(0,0,0)$ ). This will result in scattering from the object's surface and further distortion of the field generated.

Figures 3.18 (c) and (d) show the sound field generated by SoundBender, as a FEM simulation and as directly measured by the measurement scanner, respectively. The generated field revealed significantly higher acoustic pressure levels along the curve, and also on top of the object. The area inside the convex hull also showed minimum acoustic pressure, effectively reducing scattering interference due to the presence of a passive prop. Finally, Figure 3.18 (e) shows a visualisation of the field generated, using solid CO<sub>2</sub> (i.e., dry ice). The vapours helped to identify the lines of the field, providing a quick evaluation tool for informally testing different experimental conditions, such as implementing stretching/steering behaviours. Similar situations to that shown in Figure 3.18 (a) (field in the presence of the prop) were also simulated for a PAT, as can be seen in Figure 3.19 (a), and for SoundBender, as shown in Figure 3.19 (b). These further illustrate the need for hybrid modulators to create complex fields (i.e., self-bending beams). The PAT clearly failed to



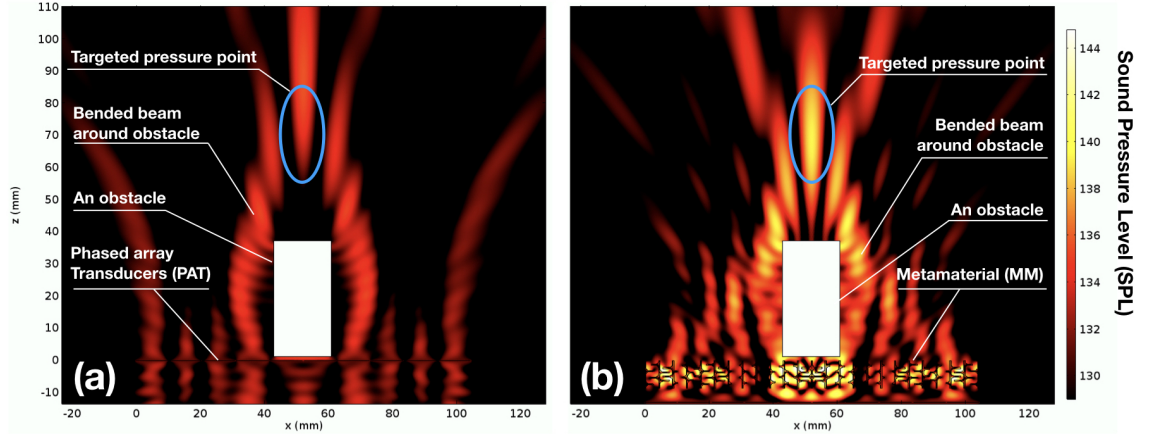


Figure 3.19: A Comparison of bent beam made with the occurrence of an obstacle using a PAT and SoundBender: (a) the PAT failed to bend sound beams to create a focal point at a target position; (b) SoundBender made use of MM and successfully bent the sound beam to create the focal pressure point at the target position.

reconstruct the bended beam flowing around an obstacle to create a focal pressure at a target point, while SoundBender successfully create such a beam.

### 3.6.2 Dynamic control of the self-bending beam

This section examines the ability of the proposed technique to dynamically adjust the shape of the static field encoded in the MM. This study first created a levitation trap on top of an obstacle, then tested its performance by stretching the bent beam to various stretching values (i.e., displacement in the  $Z$ -axis) as shown in Figures 3.20 (a) and (b). The study also tested performance by steering the beam at different values, as in Figures 3.20 (c) and (d) (i.e., displacements in the  $XY$ -plane). The study found that the technique allowed for maximum displacements of  $\approx 2$  cm in the  $X$ - and  $Y$ -axis, and up to 8 cm along the  $Z$ -axis. These extreme scenarios are illustrated in Figure 3.20, which indicates the results of the FEM simulations (top row) and actual measurements of the field (bottom row).

The possibility of creating tactile feedback was also empirically tested, by modulating the carrier wave (40 kHz) with an envelope at 200 Hz (i.e., within skin receptors' response range). This resulted in a force of 2.3 mN behind the obstacle, perceivable to more than 90 % of the users, according to related studies (Ochiai et al., 2016a; Korres and Eid, 2016). The tests also revealed that the tactile sensation remained vivid in  $\approx 3$  cm displacement in the  $X$ - and  $Y$ -axis, and  $\approx 10$  cm in the  $Z$ -axis. It is also worth noting that even when the tactile feedback is most perceivable above the object, the space around it (i.e., along

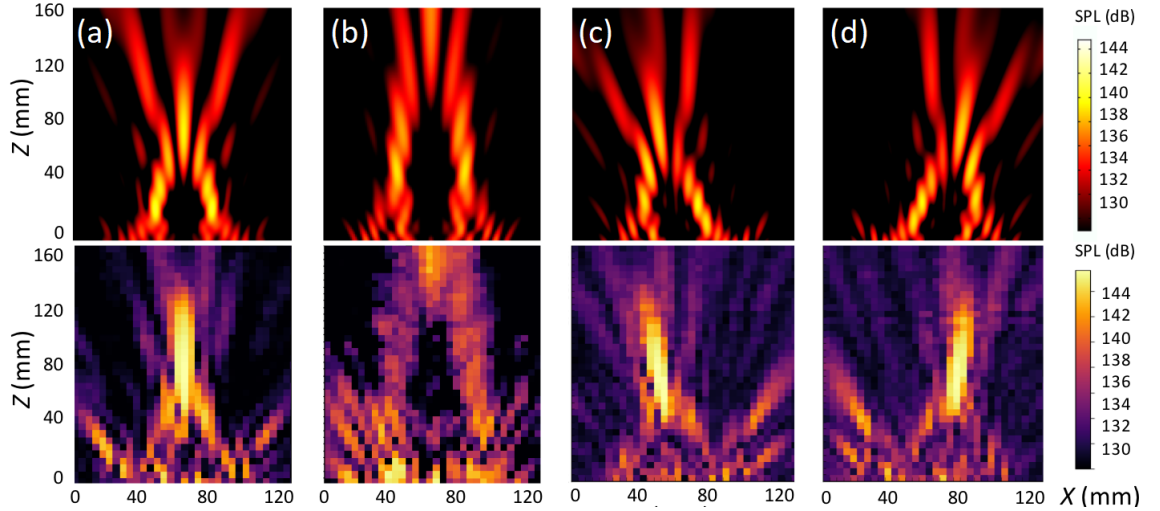


Figure 3.20: Evaluating the proposed control mechanisms for extreme cases allowing levitation. The top row shows the simulation results made using (COMSOL), while the bottom row shows actual measurement results: (a) a static sound field generated using a standing wave signal through passive MM; (b) a dynamically-stretched sound field ( $\Delta z = 8$  cm); (c) shearing to the left ( $\Delta x = -2$  cm); (d) shearing to the right ( $\Delta x = -2$  cm).

the self-bending beam) can also produce tactile feedback. This allows for feedback along the continuous surface created by the self-bending beam.

### 3.7 Example applications

This section explores some of the applications enabled by the SoundBender, using the example of the self-bending beam, where it provides a means for creating the dynamic reconfiguration of a point beyond occluding objects. The exploration is structured around three basic types of interactive features that can be dynamically reconfigured using SoundBender: a) modulated high-pressure points (i.e., tactile feedback); b) levitated objects; c) non-solid elements. This exploration is restricted to a small form factor (as demonstrated in the chapter), but also to formats that allow for free placement (or removal) of passive props or obstacles on top of SoundBender.

#### 3.7.1 Around-object tactile feedback

Figure 3.21 (a) shows a basic example that modulates the self-bending beam at 200 Hz, to create a tactile field. Such a field will show maximum radiation pressure above the object, but also high pressure along the entire surface of the curve (i.e., around the sides



Figure 3.21: An exploration of the applications of reconfiguring three types of interactive features: (a) haptic feedback behind an obstacle; (b) levitation around the obstacle; (c) reconfiguration of non-solid objects, (e.g., changing the fire’s angle).

of the object). The presence of tactile feedback prior to actually touching the object (on top and/or around it) can be used to provide users with a feed-forward, informing them of the outcome of their actions before starting the interaction with the tangible passive prop. The dynamic adjustment of the feedback provided can enrich the granularity of the contextual information delivered. For example, changing the modulating frequency can produce different tactile sensations, each with a particular meaning. Moving the beam (i.e., steering or stretching it) can guide a user’s hand towards the object, facilitating eyes-free interaction.

### 3.7.2 Around-object levitated objects

The combination of replaceable props and levitated objects on top of these props (as shown in Figure 3.21 (b)) easily lends itself to the creation of interactive decorative elements, interactive visualisations and toys of different types. For example, in the context of a board game, passive props can be used to represent various characters and creatures, while the levitated elements can be used to represent spells or power ups affecting them. The speed or trajectory of the levitated bead can indicate the current status of the power-up, letting it fall as its effect diminishes. Additional sensors (e.g., a proximity sensor) on the passive prop can enable the prop react to the levitated element (e.g., by illuminating the eyes or detecting an active power-up), while also extending interactivity to the passive prop also. The need to manually place the levitated objects will add an element of skill and uncertainty to the game (i.e., a player can fail to summon a power-up, if the object falls). In a learning environment such as museum, combining different props and levitated beads that are differently coloured can lead to exploratory interactions that will allow the user to learn about different aspects of the prop object. For example, placing a green bead on top of a country might reveal the percentage of its surface covered by forests, a black

bead can reveal its carbon footprint, while dynamically changing the height of the bead can reveal its evolution over time. Other materials, e.g., food and liquid, have previously been used for levitation before ([Foresti et al., 2013](#); [Ochiai et al., 2014](#); [Vi et al., 2017](#)), and may also be applicable to SoundBender.

### 3.7.3 Around object non-solid features

Pressure fields from SoundBender can also affect non-solid elements such as the flame of a candle (see Figure 3.21 (c)), or smoke, e.g., the dry ice used in Figure 3.18 (e). This can extend on the range of animated elements that can be added on top of the passive prop. In the first case, the direction of the flame in Figure 3.21 (c) aligns to the steering direction of the sound field, while the intensity of the flame is affected by the intensity of the field (i.e., it is brighter at lower pressures). In the case of a cupcake with a lit candle on it for instance, the direction of the flame can be synchronised to an external source (e.g., a happy birthday song). A source such as incense can be employed to implement smell delivery devices, with SoundBender reconfiguring the direction of the flow. Such flow control can provide non-solid displays with additional approaches for reconfiguring the trajectory of the diffuser, which is acknowledged as one of the aspects constraining the format, and which could be a scenario where non-solid diffusers could be applied ([Sahoo et al., 2015](#)).

## 3.8 Limitations and discussion

This chapter represents an effort to draw from techniques in related fields (i.e., acoustics and optics) into a reproducible technique, to allow HCI practitioners to explore application that controlled high resolution sound fields with a hybrid sound modulator, which not reproducible with PAT. However, this does not imply an absolute superiority on the part of hybrid modulators in comparison to PATs. PATs provide significant versatility, while hybrid modulators (like SoundBender) will only be useful in scenarios where a sound field with high spatial resolution is needed and only smaller dynamic changes are required. Even so, the spatial configuration of the modulator (i.e., its shape and spatial arrangement) will be just as relevant as the type of modulator itself. For example, both a flat PAT or SoundBender will struggle to recreate a standing wave pattern, while this is trivial, with simply two transducers. Thus, any type of modulator must simply be considered as a technique, with both strengths and limitations. This chapter proposes that the hybrid

technique provides a tool for the HCI community with which to explore new applications and more complex sound fields, with the technique helping designers to identify and address the primary challenges and pitfalls related to the use of these hybrid modulators.

The exploration of this research focused on self-bending beams. This focus assisted in the exploration of many practical aspects related to the creation of hybrid modulators, the two most important being: 1) the greater relevance of the modulator pitch compared to phase or amplitude; 2) the feasibility of delegating dynamic phase and amplitude control to the PAT, even if this only allows for a lower spatial resolution on the sound field.

However, the exploration with self-bending beams was limited to phase control, which governs the geometry of the sound field. Control of the amplitude using the PAT may be capable of enabling other effects. For example, the injective mapping in Figure 3.13 (b) identifies the points on the hybrid modulator that contribute to the intensity of each part of the curve. Dynamically adjusting the amplitude of transducers contributing to specific parts of the curve (i.e., the part they are ‘tangent’ to) may provide more control and dynamic effects. For example, reinforcing a section of the curve could potentially create a ‘ring-like’ field, while rapidly moving intensity along the curve (e.g., from the top of the beam downwards) may create a tactile feedback similar to pressing a button.

The exploration of the influence of the gap between the MM and the PAT also revealed a smoothing effect on the phases used on the PAT. This limits the type of dynamic effects that the PAT can create, indicating that such operations must avoid high frequency changes. This needs to be considered when exploring new algorithms for dynamic control of this type of hybrid modulators. Other aspects, such as the phase distribution across this gap, or even the use of coupling layers between the MM and the PAT should be explored for further control. It is also worth noting that, although the levitation signatures can be applied successfully, other levitation signatures, such as bottle beams (Marzo et al., 2015), resulted in high pressure inside the self-bending volume. This type of levitation was still possible without obstacles, because obstacles will result in sound field scattering.

The proposed technique in this chapter can also be applied to sound fields other than self-bending beams, opening up contexts for further exploration. For example, MM can be used to encode specific tactile patterns (e.g., a multipoint pattern, representing a tactile icon). The designer can then focus on creating different modulation schemes, beyond the usual modulation at 200 Hz, with a 50 % duty cycle (Carter et al., 2013), to test various tactile experiences. This technique has also been applied to finely reconfigure a different type of sound field, which will be described in Chapter 4. Replacing the MM with

another one (i.e., encoding a different location for the points/tactile icon) can assist in rapidly exploring tactile stimuli. This may also allow for interactive scenarios beyond those explored in this chapter, with the user replacing either the MM, the passive prop, or the levitated beads to achieve different effects. This can encourage new ways of thinking about tangible user interfaces, with MM, obstacles, and levitated objects working as modifiers of the tangible element.

### 3.9 Conclusion

This chapter presented SoundBender, a hybrid technique for sound modulation that combines acoustic MM and PAT. The MM was employed to encode complex sound fields that cannot be created using PATs only. The PAT allowed for dynamic real-time control of the sound field. This technique was illustrated using self-bending beams, which allowed for including interactive artefacts, including passive props located on top of the modulator, and interactive elements (i.e., tactile points, levitated matter and non-solid features) above the prop. Five steps were described to guide the creation of such interactive artefacts, starting from the basic shape of the passive prop, and detailing the fabrication of the hybrid sound modulator and the control algorithms to enable interactive features above and around the prop. This chapter demonstrated the feasibility of the hybrid technique, and compared it to alternative approaches (focused points and self-bending beams implemented with a single phased array). It also demonstrated the dynamic reconfiguration of interactive features such as tactile points and levitated object, and provided several novel interactive experiences enabled by SoundBender at the end of the chapter that can potentially be achieved by SoundBender. These findings may be useful to the HCI community in terms of further exploration of dynamic control over other complex sound fields. Although this chapter described precise control of non-solid particles, a study aimed at reconfiguring permeable mid-air display using an ultrasound manipulation algorithm has yet to be written. Therefore, the following chapter presents the study of a tool for such a system. It first describes the design parameters, followed by verification of the proposed system and its performance evaluation, before conclude it with a demonstration of various applications enabled by the proposed system. The thesis author conceived the idea in this chapter and the following chapter, designed and implemented the system, gathered experimental data, demonstrated the concept, analysed the data and wrote the published manuscript of the chapters (Norasikin et al., 2017, 2018, 2019), with contributions from all authors.

## Chapter 4

# SonicSpray: a technique for reconfiguring permeable mid-air displays

### 4.1 Introduction

This chapter<sup>1</sup> presents a reconfigurable display of permeable materials, conceived, implemented and analysed by the thesis author. Although predominately the work of the thesis author, the published manuscript of this chapter (Norasikin et al., 2019), contains contributions from all authors.

Imagine a display that is as shapeless as water, that can be reconfigured without physical contact, and that is interactive and computationally reconfigurable to form shapes in mid-air. This type of display has been illustrated in science fiction films such as Iron Man (Black, 2013), and today, many such mid-air displays have been demonstrated using proof of concept; for example, PixieDust (Ochiai et al., 2014), HoloVect (Ruiz-Avila, 2016), MistForm (Tokuda et al., 2017), and Luciola (Qiu et al., 2018). These types of display have consistently attracted the attention of the imaginative community, primarily as it relates to the interactive graphics of HCI.

Despite technological advancements in these permeable, reconfigurable mid-air displays, they remain bulky (Ochiai et al., 2014; Sahoo et al., 2015; Lam et al., 2015b; Qiu et al., 2018), and generally involve a high price point, which is acknowledged as one

---

<sup>1</sup>This chapter was published in Proceedings of ISS '19, Proceeding of the 2019 ACM International Conference on Interactive Surfaces and Spaces, pp. 113–122 (<https://doi.org/10.1145/3343055.3359704>)



of primary obstacles to their commercialisation (Smalley et al., 2018a). The ability to provide a sharp resolution in their reconfiguration while retaining a minimal form factor is recognised as another major challenge (Alexander et al., 2018), a solution to which is even more crucial for permeable displays dealing with aerosols, where the ability to control the shape and trajectory of aerosols in mid-air – while retaining a laminar flow – is accepted as a factor limiting their potential form factors (Sahoo et al., 2015). As a result, existing permeable, reconfigurable mid-air displays are not commonly found for minimal form factors, which result in these displays not being reconfigurable (Rakkolainen and Sand, 2013; Suzuki et al., 2016; Alakärppä et al., 2017) and not portable (Freeman et al., 2018), or both (Ando et al., 2017; Otao and Koga, 2017).

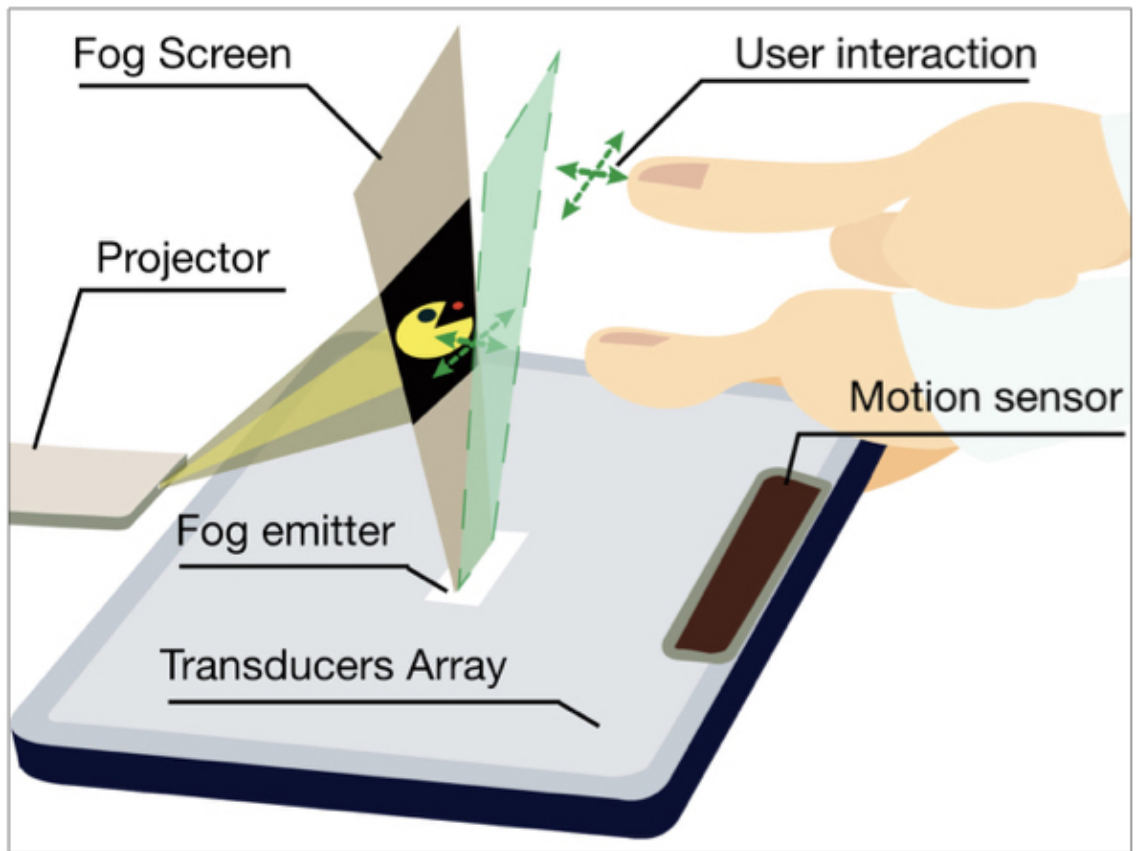


Figure 4.1: A concept for SonicSpray.

As a key contribution, this chapter describes SonicSpray, an innovative technique for reconfiguring permeable mid-air displays using ultrasound Bessel beams (the concept for which is shown in Figure 4.1). SonicSpray is developed around two key properties: 1) it enables mid-air display control through a minimal form factor (Alexander et al., 2018) and is constructed using low cost, off-the-shelf components (Smalley et al., 2018a); and 2) it maintains laminarity of the flow during reconfiguration, thus retaining display qual-

ity (Rakkolainen, 2008b). These properties enable four key advantages: 1) it removes enclosures (i.e., transparent electrodes) like those by Sahoo et al. (2015); 2) it is silent, thereby avoiding fans and other noisy moving parts (Tokuda et al., 2017); 3) it allows for simple and precise real-time control of the laminar airflow, using only one control point on the  $XY$ -plane; 4) it has a minimal form factor. The work in this chapter leverages these benefits to enable the creation of novel mid-air displays, which are explored in this chapter. The SonicSpray technique can also be combined with other existing techniques (e.g., the work of Rakkolainen and Sand (2013), Lam et al. (2014), Sahoo et al. (2015), Suzuki et al. (2016)) to enable additional form factors.

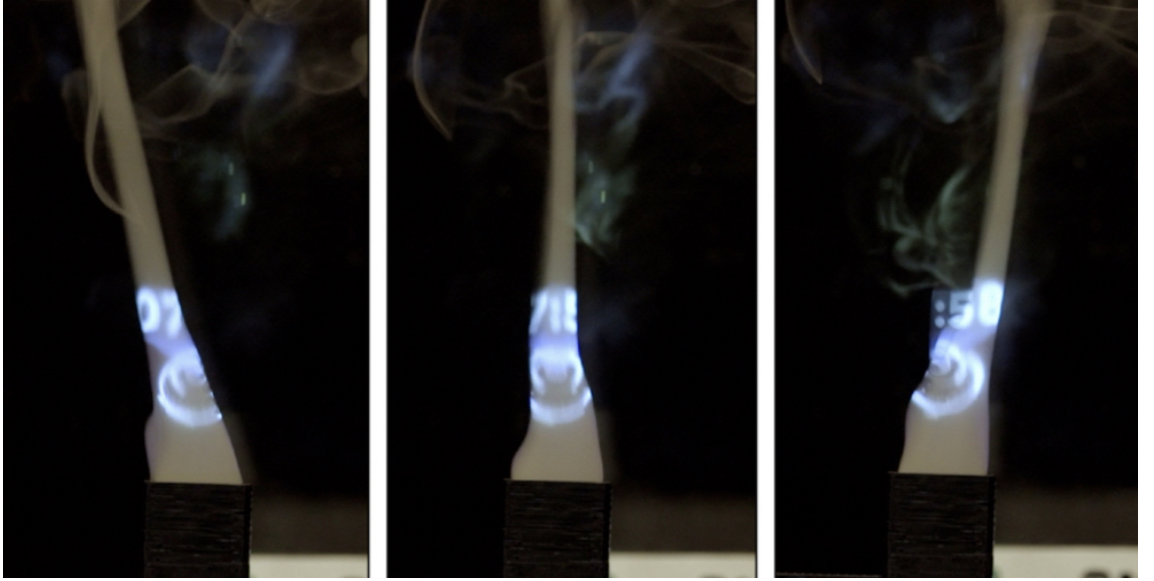


Figure 4.2: SonicSpray is visualising a graphical clock in mid-air by laterally oscillating its narrow mist.

This chapter first describes the SonicSpray technique, which uses an elongated Bessel beam to create laminar aerosol flows, and diffraction gradients that allow for their real-time reconfiguration. The technique is compatible with PATs and hybrid modulators of MM (Norasikin et al., 2018) and, in all cases, the direction of the flow can be easily and precisely be controlled by redirecting the beam towards a user-defined control point. This chapter explores the potential of the SonicSpray technique (beyond the prototype in Figure 4.2) in two steps. First, it describes the principle and explores the effects of varying PAT sizes (from  $16 \times 16$  to  $2 \times 2$  transducers), identifying minimum operational form factors for SonicSpray, based on sound field simulations, conducted using COMSOL Multiphysics, wind speed tests, and laminar airflow tests. Second, it verifies the spatial control algorithm of the proposed technique via careful analysis of the sound field using

COMSOL Multiphysics, and evaluating it in terms of lateral oscillation, which is reported as the most significant issue for mid-air displays ([Lee et al., 2011](#)). In particular, this chapter studies the effects of lateral oscillation on the quality of the laminar aerosol, as well as the effects of varying the number of transducers used. Finally, it demonstrates a selection of the working applications enabled by the SonicSpray, such as its ability to create and accurately direct aerosols while retaining the laminarity of the flow required for display purposes. This chapter concludes with a discussion on the limitations of SonicSpray, and also on the novel designs that it enables, both as a stand-alone control technique, and in combination with other existing techniques.

## 4.2 Related work

This section reviews two groups of reconfigurable mid-air displays in HCI, i.e., permeable and impermeable, in relation to the challenges identified above, including their capacity for mid-air aerosol control ([Sahoo et al., 2015](#)) and their ability to retain laminar flow ([Rakkolainen, 2008b](#)), as well as their potential for small form factors and precise control ([Alexander et al., 2018](#)).

### 4.2.1 Impermeable mid-air displays

There are many techniques available for reconfiguring impermeable mid-air displays. SensaBubble ([Seah et al., 2014](#)) used computer-controlled fans to direct a fog-filled bubble that contained graphical projected contents (e.g., letters and icons), but only allowed very coarse control of the bubble’s trajectory. The system used fans to control the horizontal distance of the bubble to its emitter, as well as the vertical level of the bubble in relation to the floor, in order to lengthen the life of the bubble. In addition to the control being coarse, air turbulence was unavoidable, which limited the ability of the system to be used as mid-air display. [Sahoo et al. \(2015\)](#) improved trajectory control of the fog-filled bubble using electric fields created by an array of high-voltage transparent electrodes. The system first filled bubbles with charged fog. Then, the system let the bubbles pass through an array of transparent electrodes. To reconfigure the trajectory of the bubble, the system modulated the voltage with the electrodes. However, the electrodes in the prototype hindered user interaction, because of their large size. The improvements came at the expense of hindering user interaction (i.e., the presence of electrodes or the use of high voltages) and, in both cases, the bubble burst when touched. This problem did not

occur in a prototype developed by [Lam et al. \(2014\)](#). The authors described a 2D array of small and flat fog emitters that were able to create small fog displays at discrete positions across a table top. However, the affordance of screen continuity could only be ensured across display elements when the emitters were in a line with one another.

Levitation approaches have also been explored. ZeroN ([Lee et al., 2011](#)) presented a mid-air display by levitating a magnetic ball that has graphical image projected onto it. However, this magnetic levitation display system, was bulky and costly, as it required the combination of two systems to control the levitated ball, i.e., a magnetic system for controlling the object in vertical position, and a mechanical system for controlling object's lateral displacements.

Aerial Tunes ([Alrøe et al., 2012](#)) used Bernoulli's effect to control mid-air displays on a vertical axis. This work combined Bernoulli's the effect and sensors to create a floating soundscape slider of a ball. The ball floats  $\sim 2\text{--}30$  cm above its base. Floatio ([Yui and Hashida, 2016](#)) improved such control, again by including a second mechanical system. Although it can be integrated between its own modules to enable the movement of balls across a larger space, the integration still resulted in a bulky display system. In addition, these systems demand prolonged engagement due to the instability of the floating balls, and the challenges presented by understanding the system.

Other works have create reconfigurable mid-air displays, using ultrasonic levitation and PAT arrays (e.g.,  $16 \times 16$  transducers). Pixie Dust ([Ochiai et al., 2014](#)) used four PATs and demonstrated the manipulation of objects of different material and density (e.g., paper models and washers). Other works used opposing PATs ([Qiu et al., 2018](#)) or a single PAT with a flat reflector ([Kono et al., 2014](#)), and have been used to demonstrate precise 3D positioning of particles in space ([Omrou et al., 2015](#)), as well as rotations and multi-point levitation ([Marzo et al., 2015](#)). This technique has also been implemented for small form factors. For example, JOLED ([Sahoo et al., 2016](#)) used a  $30 \text{ mm} \times 80 \text{ mm}$  PAT and demonstrated control of a bistable display in mid-air, by coating the voxels with titanium dioxide ( $\text{TiO}_2$ ), and using electric fields to flip them. Point-and-Shake ([Freeman et al., 2018](#)) used  $80 \text{ mm} \times 40 \text{ mm}$  PATs to create and select mid-air buttons. FloatingCharts ([Omrou et al., 2016](#)) created mid-air point charts, reconfigured in real-time through compositions of smaller PATs, designed in a round shape (PAT  $\varnothing 30 \text{ mm}$ ). However, in all of these cases, displays were made of sparse particles, and a physical touch will eventually disturb the stability of these particles ([Freeman et al., 2018](#)). This issue limits their use as interactive display systems.

### 4.2.2 Permeable mid-air displays

Permeable displays allow users to reach into and interact inside the display volume, with the display reconstructing itself around the user’s hands and body. However, this involves the use of free flowing aerosols, making their control more challenging and limiting the number of applicable techniques and form factors. The most prominent technique is fog screen ([Rakkolainen, 2008b](#); [Rakkolainen and Sand, 2013](#)), which employed fans to create a laminar flow, but resulted in permeable displays constrained to a flat form factor. Works by [Lam et al. \(2015b,a\)](#) illustrated a volumetric mid-air display by using a 2D array of static fog nozzles. This fog emitter array was static and required a big numbers of emitters module for a larger working volume. The number of emitters can be reduced by replacing standard nozzles with mechanically actuated nozzles ([Lam et al., 2014](#)). This nozzles can be adjusted according to the depth of the parts of the display. This concept was extended to a larger form-factor by MistForm ([Tokuda et al., 2017](#)), which combined mechanical actuators and fog nozzles mounted on a flexible PVC pipe, thereby achieving an adaptive shape changing fog screen display. However, in all cases described above, the use of fans to achieve laminar flows resulted in noise, and the direction of the aerosol flow could not be changed once it had exited the nozzle. In the case of MistForm, the form factor was also bulky. Therefore, SonicSpray should allow aerosols to be redirected even after the particles had exited the nozzle.

Instead of using mechanical actuators, [Sahoo et al. \(2015\)](#) demonstrated control of the mid-air direction of the fog screen by using high-voltage electric fields, by constraining the display between transparent electrodes. The system allowed a charged fog to pass through an array of electrodes, and the trajectory of the fog screen was changed by adjusting the voltage through the electrodes. However, this display is unlikely to be portable, since it requires a large electrodes and a fog-charging chamber. Gushed Diffusers ([Suzuki et al., 2016](#)) and BreathScreen ([Alakärppä et al., 2017](#)) demonstrate portable form factors, but they still do not allow mid-air reconfiguration, and their displays do not retain a laminar flow. Similarly, [Hasegawa et al. \(2018\)](#) demonstrated mid-air control of the direction of an aerosol for their smell delivery system using PATs; however, unlike SonicSpray, the researchers did not address the laminar properties of the aerosol. Additionally, while they acknowledged the issue of ghost images, which limits the control of the fog, the current chapter of the present research indicates how this issue is linked to the resolution of the modulator employed, and how the use of a hybrid modulator, i.e., a combination of a MM and a PAT ([Norasikin et al., 2018](#)), can avoid this problem, while still allowing the creation

and reconfiguration of Bessel beams, and retaining the laminar airflow of particles.

### 4.3 SonicSpray: technique for reconfiguring non-solid matter in free space

This section describes the basic technique that is used to redirect matter in free air using ultrasound Bessel beams and illustrates its behaviour using COMSOL simulations and actual experiments of a real setup.

#### 4.3.1 Basic Bessel beam creation

This section explains the reconfiguration technique, which is compatible with both PATs and hybrid modulators, and uses Bessel beams to create a stream of air particles (i.e., to move the aerosol), redirect it in real-time (i.e., to allow for mid-air control), while retaining the laminarity of the flow (i.e., for display quality purposes). This technique is related to the work of [Hasegawa et al. \(2017\)](#), in which airflow was generated through construction of a Bessel beam (i.e., a tightly focused, narrow and elongated sound beam). The beam had self-healing properties and did not diffract or spread out over a limited distance. In general, one can produce this Bessel beam using a conical arrangement of sound sources, where the sound waves will converge and concentrate their energy (i.e., ultrasonic radiation force), as shown in Figure 4.3 (left).

To construct the beam, this study used a modulator (PAT or MM) operating at an ultrasonic frequency ( $f = 40\text{kHz}$ ) in air (speed of sound  $c = 343\text{ms}^{-1}$ ). The algorithm included two steps (see Figure 4.3 (right)). First, this work computed the angle  $\theta_z$  in Equation 4.1, given a constant aperture  $A$  (modulator diameter), and  $z_m$  as the maximum height of the beam.

$$\theta_z = \tan^{-1} \left( \frac{A}{2 \cdot z_m} \right) \quad (4.1)$$

Second, this work computed the phase for each element in the proposed modulator, as in Equation 4.2, where  $k = 2\pi/\lambda$  is the ultrasound wavenumber, and  $\lambda = c/f$  is the wavelength, (8.6 mm in this study), and  $d(T_i, 0)$  is the Euclidean distance function. The phase profile  $\phi_i$  of the element can be electronically delivered to a PAT, or fabricated into a MM as in the work of [Norasikin et al. \(2018\)](#).

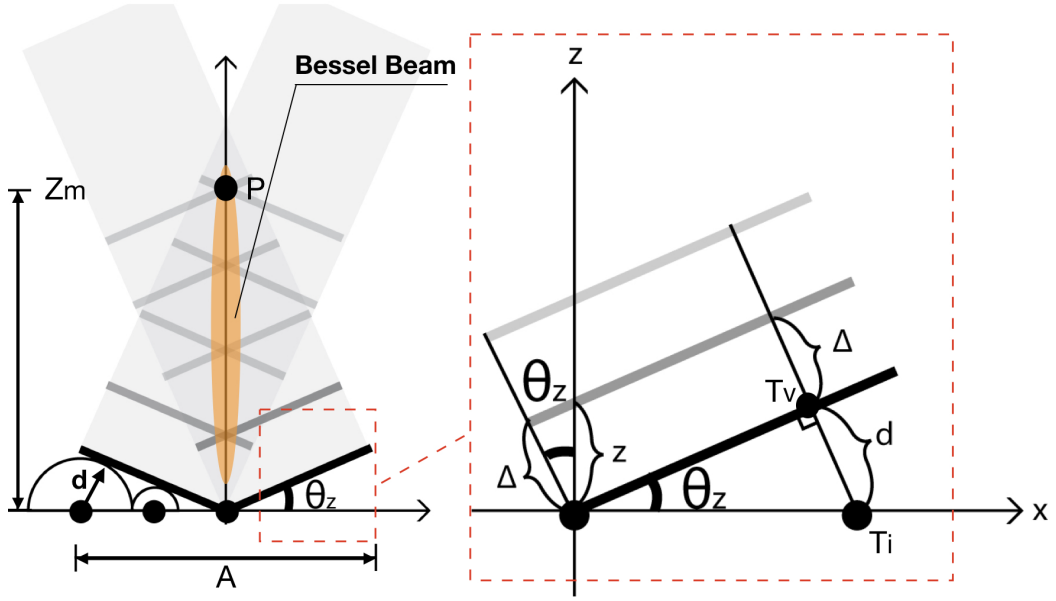


Figure 4.3: A geometrical representation of a Bessel beam: (left) an elongated and slim sound beam (i.e., a Bessel beam) is created as a result of a conical and propagated wavefront; (right) the information needed to create the illustrated wavefront from a transducer in a PAT.

$$\phi_i = -k \cdot d(T_i, 0) \cdot \sin \theta_z \quad (4.2)$$

Figure 4.4 (a) shows a 3D simulation of an example Bessel beam, created on a 16 x 16 PAT, in which the field presents an elongated beam in the middle of the array, while Figure 4.4 (b) shows a horizontal slice,  $z = 100$  mm, demonstrating good focusing of the beam. Figure 4.4 (c) illustrates the SPLs achieved by varying the number of transducers in the PAT, which revealed a decline in SPL as the number of transducers (i.e., sound energy) decreased, highlighting the trade-offs between PAT size, SPL and, in turn, the feasibility of reduced PAT setups to reconfigure aerosols.

### 4.3.2 Lateral reconfiguration of the basic beam

This work introduced diffraction gratings into the methodology used to reconfigure the Bessel beam (i.e., to direct the narrow beam to the sides). This method is as an alternative to that described by Hasegawa et al. (2017), typically used for optical tweezers (Salter et al., 2013; Pesce et al., 2015), and simplifies the integration of the approach with simple PATs or hybrid modulators (Norasikin et al., 2018) as described in Chapter 3. The Equation 3.23 was simplified to Equation 4.3, where it only requires a shearing function



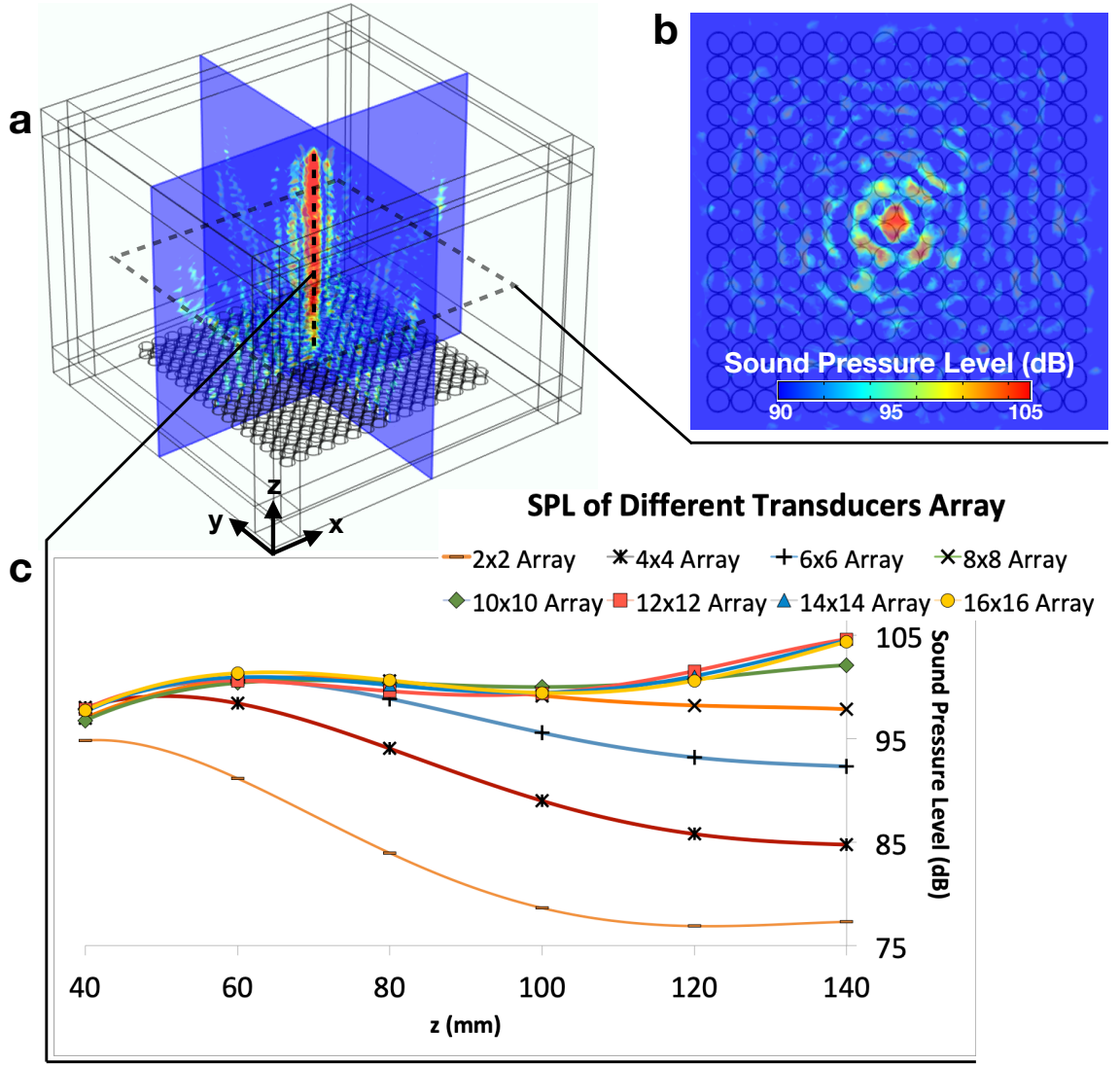


Figure 4.4: Simulation of a Bessel beam using COMSOL Multiphysics: (a) a 3D simulation of Bessel beam sound field; (b) a horizontal slice of a Bessel beam at  $z = 100$  mm; (c) the SPL levels achieved using a different number of transducers.

(i.e., a diffraction grating), rather than a stretch function (i.e., a Fresnel lens).

Given the reference point of the Bessel beam  $P(0,0,z_s)$  (e.g., for an example, see Figure 4.5 (A1) where  $z_s = 60$ mm), and a desired displacement of the Bessel beam in the  $XY$ -plane  $(\Delta x, \Delta y)$ , the position of each  $i$ -th element in the modulator  $T_i(x_i, y_i, z_i)$  should be identified. Then, the diffraction gratings phase  $\psi_i$  is computed for the  $i$ -th element  $T_i$  by using Equation 4.3. In the case of a simple PAT, the final phase delay  $\phi'_i$  for each transducer is simply computed as the phase addition of the Bessel beam and diffraction gratings ( $\phi'_i = \phi_i + \psi_i$ ). Hybrid modulators will instead use  $\psi_i$  to drive the PAT (i.e.,  $\phi_i$  is encoded in the MM).

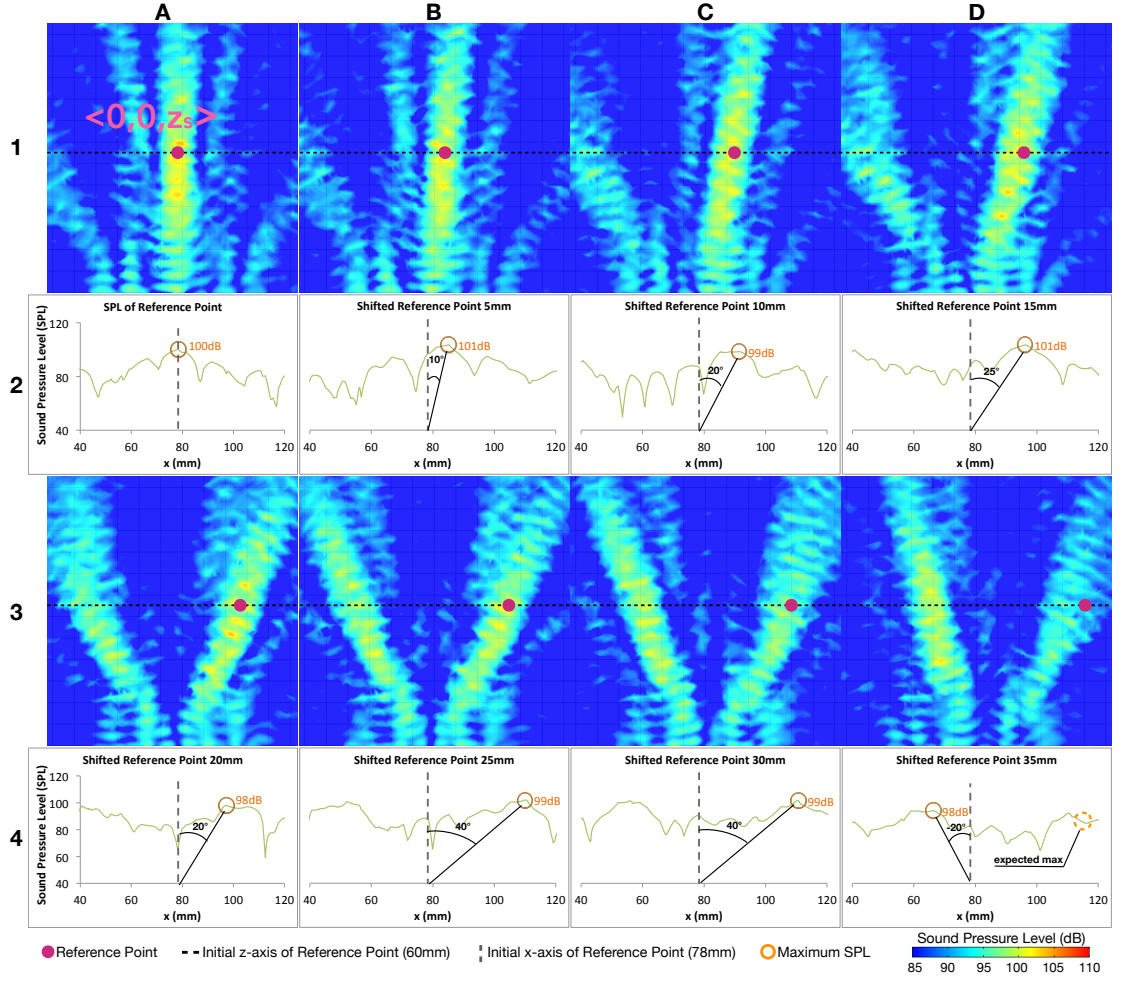


Figure 4.5: Simulation of the beam control algorithm: rows (1) and (3) are sound fields of a different lateral shift, and rows (2) and (4) are graphs of the SPLs of the sound fields.

$$\psi_i = \frac{2\pi}{\lambda \cdot z_s} (x_i \cdot \Delta x + y_i \cdot \Delta y) \quad (4.3)$$

#### 4.3.2.1 Simulation of lateral reconfiguration algorithm

This chapter explores the capabilities of the reconfiguration algorithm (using COMSOL Multiphysics simulations) to laterally shift the reference point ‘P’, highlighting important relationships between the maximum shifting and the type of modulators used. Figure 4.5 shows the simulation results of the algorithm when using PATs. Rows (1) and (3) present the sound fields of different lateral shifts on the  $X$ -axis ( $\Delta x$ ), while rows (2) and (4) are cutline graphs of the sound fields at  $z_s = 60$  mm. To easily note the changes, this work first denoted the initial  $Z$ -axis of the reference point  $z_s$ , using a horizontal dashed-line, as in rows (1) and (3), and the initial  $X$ -axis with a vertical line, as in rows (2) and (4). Following on, it denoted their maximum SPL using a circle, and the angle from its initial

$X$ -axis line was identified. The results verified that the algorithm was able to precisely shifts the reference point ‘ $P$ ’.

Figure 4.5 shows a ghost beam in the generated sound fields (Hasegawa et al., 2017; Hasegawa et al., 2018). It appears on the left side of the intended beams in Figure 4.5 (A3-D3). The intensity of the ghost’s SPL is low, from  $\Delta x = 0$ –15 mm, growing at larger shifts until it supersedes the SPL of the main beam at  $\Delta x = 35$ mm (see Figure 4.5 (D3) and (D4)). This will result in unintended airflow when the beam is laterally shifted more than 15 mm, an inherent limit related to the large size of PATs transducers ( $\phi = 10$ mm) (Norasikin et al., 2018).

This limitation can be solved with hybrid modulators, particularly those using small cell designs. To do this, this chapter adopted the design by Memoli et al. (2017) (i.e., the size of the brick was  $\lambda/2$ , as in Figure 4.6 (b)) and created higher quality Bessel beams. Figures 4.6 (a) and (c) show a comparison of the lateral shifted beam at  $\Delta x = 35$  mm with a PAT and with a hybrid setup.

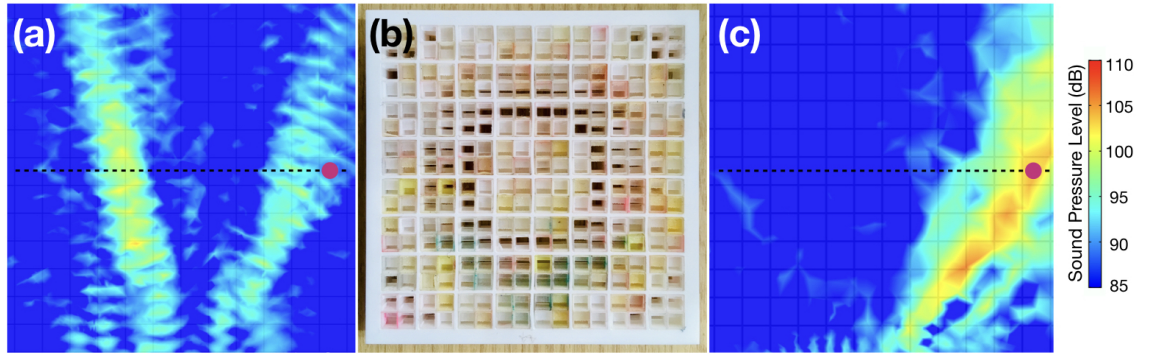


Figure 4.6: A comparison of approaches (bead shifted  $\Delta x = 35$  mm): (a) a PAT (transducer  $\phi = 10$ mm) failed to steer the beam according to the control point, with ghost beam appearing on the left side and superseding the real beam on the right; (b) the equivalent MM, using a smaller cell size ( $\lambda/2$ ); (c) the resulting field using the hybrid setup (i.e., a combination of MM and PAT), in which ghost beam were avoided.

## 4.4 Experimental characterisation

As in the technique outlined above, this section describes experiments and analysis conducted to explore whether SonicSpray can be used in practice to direct and control the aerosol flow, while retaining the laminarity of the flow. The relationships between the number of transducers used, the SPLs achieved, and the resulting wind speed are ana-



lysed here (and are always constrained to the laminar regime). Finally, this work limited its exploration to lateral displacements of up to 35 mm, as a means for deriving useful results, independent of whether a PAT or hybrid modulator is used.

#### 4.4.1 Experimental setup

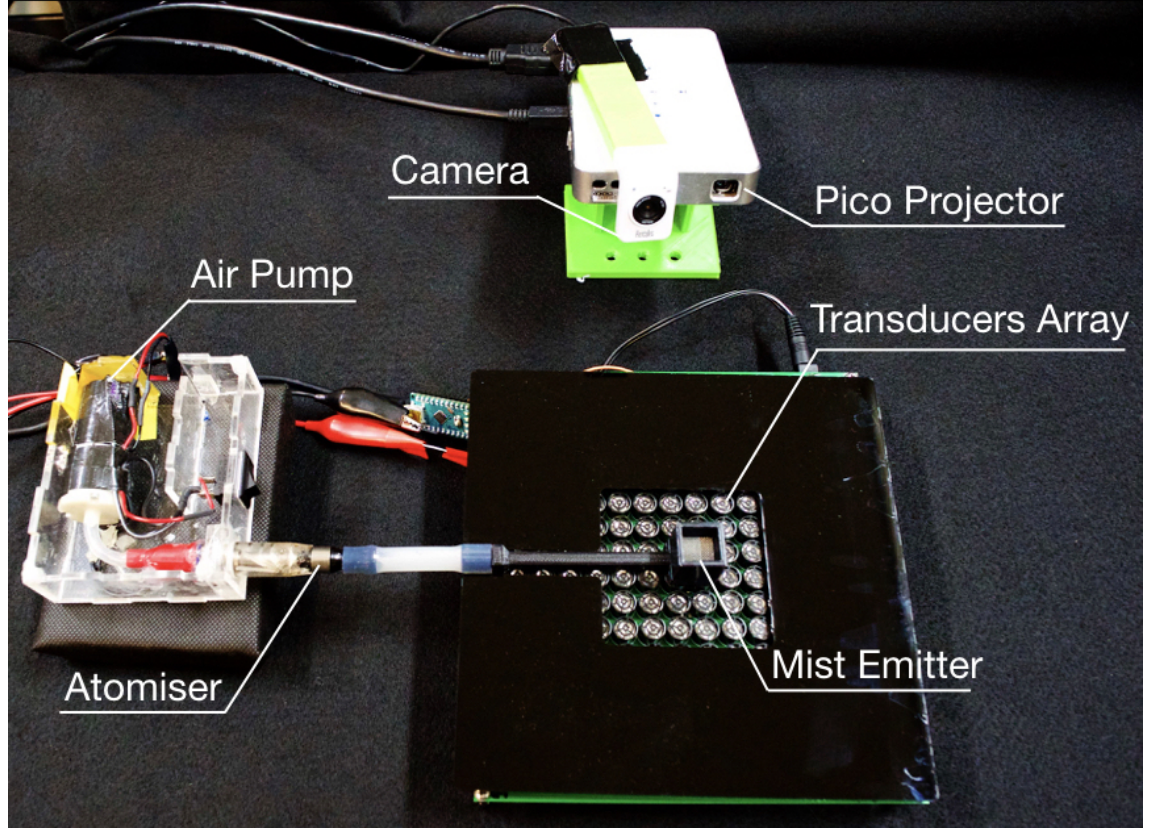


Figure 4.7: A SonicSpray setup consists of a phased array transducer (PAT), a 3D-printed mist emitter, a mist atomiser, an air pump, a camera, and a Pico projector.

This work assembled the prototype as shown in Figure 4.7. It consisted of an off-the-shelf atomiser (manufactured by IMECIG), an air pump (manufactured by SIMILK, operated at 0.75W), propylene glycol and glycerol liquid as for the mist, and a 3D-printed-squared-orifice emitter (with the orifice measuring  $40 \text{ mm}^2$ ). The reason a squared-orifice was to minimise the number of transducers that are blocked by the emitter. A fine metal mesh was packed inside the orifice to reduce airflow velocity from the air pump, and to create even distribution of mist particles over the orifice area. The emitter was aligned to the expected Bessel beam position to ensure the mist responded quickly to the ultrasonic radiation force. Additionally, the resulting emitter provided a near-zero initial speed to the flow (i.e., the mist floated upwards due to buoyancy, but the speed was below a min-

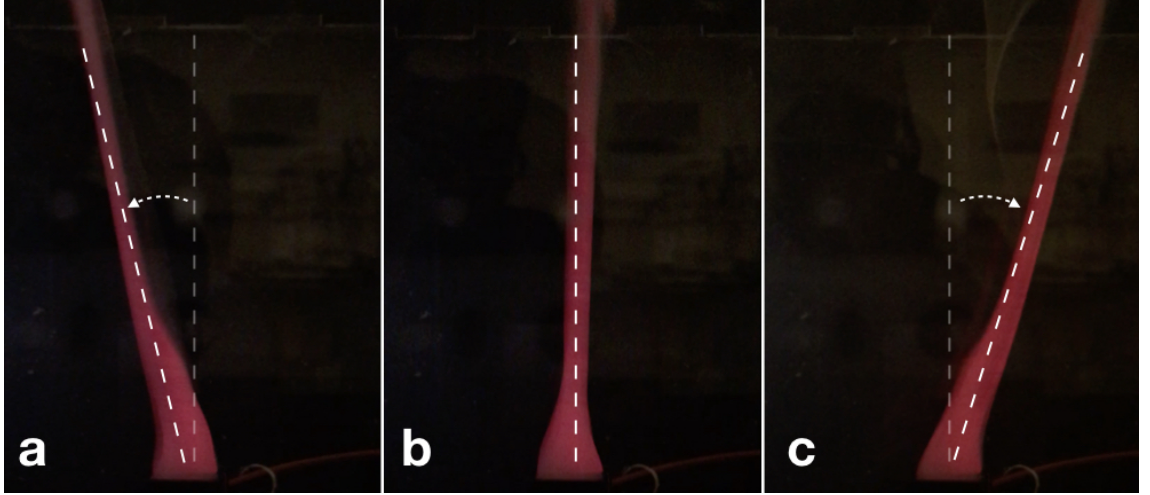


Figure 4.8: A SonicSpray performing lateral reconfiguration: (a) A laminar mist is steered to the left (illuminated by a refracted laser beam); (b) laminar mist is steered to the centre; (c) laminar mist is steered to the right.

imum threshold measurable by an anemometer), ensuring that the tests in this work only measured particle accelerations induced by SonicSpray technique, as a result of acoustic pressure. The 16 x 16 PAT followed the design of [Marzo et al. \(2018\)](#), using transducers from Manorshi Electronics (MSO-P1040H07T,  $\phi = 10$  mm) operated at a 40 kHz frequency, with metal-oxide semiconductor field-effect transistor (MOSFET)s to amplify control signals to 15 V<sub>pp</sub> (MOSFET, Microchip MIC4127), and a field-programmable gate array (FPGA) to control them (Cyclone IV EP4CE6). The array was connected to a personal computer (PC) via universal asynchronous receiver/transmitter (UART) protocol at 250 kbauds ( $\sim 250$  second per update).

#### 4.4.2 Camera-projector calibration

The prototype included a camera–projector system, providing a simple projection mapping for a mid-air display using SonicSpray, which was later used for application examples in this chapter. The system combined a Hercules HD Twist camera (with a resolution of 1,024 x 768 px), and an iCODIS LED mini projector (with a resolution of 854 x 480 px).

A computer program was written in C++, incorporating OpenGL (version 4.6.0) and OpenCV (version 2.4.13.6), to computationally control transducer phase and the mist, calibrate the camera and projector, and map the graphical content onto the laminar mist.

To perform the camera-projector calibration, this work referred to research by [Zhang \(2000\)](#), [Moreno and Taubin \(2012\)](#), and [Din et al. \(2014\)](#), which primarily incorporated

the pinhole model in their calibration algorithms. First, a general equation of the pinhole model was formulated (see Equation 4.4) where  $m'$  is the image plane coordinates,  $A$  is a camera's intrinsic parameters,  $[R|t]$  is camera's extrinsic parameters, and  $M'$  is the world coordinates. The equation was expressed as Equation 4.5. In the equation,  $(X, Y$  and  $Z)$  were the 3D point coordinates in the world,  $(u$  and  $v)$  were image plane coordinate in pixels, matrix,  $(C_x, C_y)$  was a central point of the image plane, and  $f_x$  and  $f_y$  were the focal lengths in pixel units. To calibrate the camera and projector, ten images of a 10 x 7 checkerboard board and ten projected image of that checkerboard (with a resolution of 640 x 480 px) were captured. The calibration<sup>2</sup> procedure was summarised into two main steps: camera calibration, and projector calibration. In the steps, the 'c' subscript was used for camera parameters and the 'p' subscript was used for projector parameters. It is worth noting here that the same equations (Equation 4.4 and 4.5) were used for projector calibration, but they treated the projector as an inverse camera.

$$m' = A[R|t]M' \quad (4.4)$$

$$\begin{bmatrix} u \\ v \end{bmatrix} = 1 \begin{bmatrix} f_x & 0 & C_x \\ 0 & f_y & C_y \\ 0 & 0 & 1 \end{bmatrix} \begin{bmatrix} r_{11} & r_{12} & r_{13} & t_1 \\ r_{21} & r_{22} & r_{23} & t_2 \\ r_{31} & r_{32} & r_{33} & t_3 \end{bmatrix} \begin{bmatrix} X \\ Y \\ Z \\ 1 \end{bmatrix} \quad (4.5)$$

#### 4.4.2.1 Camera calibration algorithm

1. Capture the printed checkerboard and detect its corner points, then define them as the image point coordinates,  $m'_c$ .
2. Define the known point coordinates of the printed checkerboard as the world coordinates,  $M'_c$ .
3. Using the camera intrinsic matrix  $A_c$  and information from steps 1) and 2), compute the camera extrinsic matrix  $[R|t]_c$ .

#### 4.4.2.2 Projector calibration algorithm

1. Place printed checkerboard in the camera view, and capture a photo of it with the same calibrated camera.

---

<sup>2</sup>We refer to calibration OpenCV code retrieved from [https://docs.opencv.org/2.4/modules/calib3d/doc/camera\\_calibration\\_and\\_3d\\_reconstruction.html](https://docs.opencv.org/2.4/modules/calib3d/doc/camera_calibration_and_3d_reconstruction.html)

2. Identify the checkerboard corners and, using Equation 4.4, compute the extrinsic parameters.
3. Use a projector to project the checkerboard at the same position and orientation as the checkerboard in 1).
4. Using the camera intrinsic from step 1) in camera calibration, and the extrinsic value from step 2) of this projector's calibration, compute the  $M'_p$ .
5. Define the coordinates of the known image plane checkerboard used in step 3) as  $m'_p$ .
6. Using the information derived from the steps above, compute the projector intrinsic parameters  $A_p$ .
7. Using the information above and the scale factor, the image plane on the projector can then be used to determine the image plane needed for the real world point coordinates, in this instance, the laminar mist.

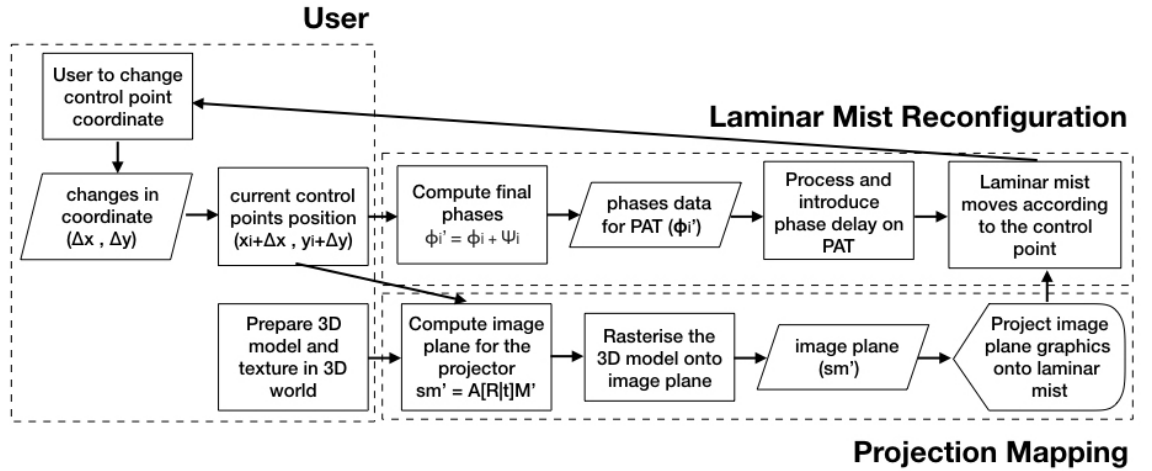


Figure 4.9: Flowchart for SonicSpray contains three main modules which are user, laminar mist reconfiguration and projection mapping.

Once the camera and projector had been calibrated, the graphical contents were mapped to the laminar mist. The process of the reconfigurable mid-air display system (laminar mist redirection and projection mapping) is simplified in a flowchart, presented in Figure 4.9. The flowchart comprised three main modules: user, laminar mist reconfiguration, and projection mapping. The user could reconfigure the direction of laminar mist using one control point in spatial space, for example, following a projection of a butterfly flying in air space as shown in Figure 4.13 (b), which the butterfly moved in



a circle motion. The system had computed the control point to move in a circle in the user module, then the computed control point data was sent to both the mist reconfiguration and the projection mapping modules. The mist reconfiguration module converts the computed control point data into meters and computes the phase delays required for the PAT ( $0-2\pi$ ). Meanwhile, the projection mapping module transform the control point into calibrated pixels coordinate by using Equations 4.4 and 4.5.

#### 4.4.3 Speed and laminar airflow test

To identify whether the Bessel beam produced a laminar or turbulent airflow, the ratio between mist's inertial forces and its viscous forces, known as the Reynolds number (Re), was calculated. The Re is described in Equation 4.6 where  $v$  is the airflow speed ( $ms^{-1}$ );  $L$  is the mist outlet dimension,  $0.0138m^2$ ; and  $\nu$  is the kinematic viscosity of the air, in this case  $10^{-6}m^2/s$ . Low Re number (i.e.,  $Re < 2,300$ ) produced a smooth or laminar type of flow due to dominant viscous forces, while high  $Re$  number (i.e.,  $Re > 2,900$ ) produced turbulent flow due to dominant inertial forces.

$$Re = vL/\nu \quad (4.6)$$

The Re was measured in three steps: First, the mist was emitted; following on, then the transducers array (e.g., a  $16 \times 16$ ) encoded with the Bessel beam was switched on. Next, the produced airspeed at several  $Z$ -axis positions above the emitter outlet, was measured with an anemometer (Kestrel1000). Finally, the Re and their errors were computed.

The three steps above were repeated to measure the Re for a different numbers of transducers, and the results was compared in Figure 4.10. It showed that Re numbers for all cases was lower than 2,300, which indicated the ability of SonicSpray to create laminar aerosol flows. Solutions with a  $4 \times 4$  and a  $2 \times 2$  transducers failed to induce airflows (i.e., speed  $\sim 0$  m/s). Figures 4.8 (a–c) demonstrates the laminar aerosol created by remaining configurations, as well as their ability to shift the beam to the left or right, as in Figures 4.8 (a) and (c), respectively. The path followed by aerosol particles was related to the particle sizes, with ultrasonic radiation dominating the motion of larger particles ( $\phi = 5.0\mu m$ ), and Stokes drag (Barnkob et al., 2012) dominating the motion of smaller ones ( $\phi = 0.5\mu m$ ). Therefore, particle size filtering technique like those suggested by Sahoo et al. (2015) can help improve flow control.

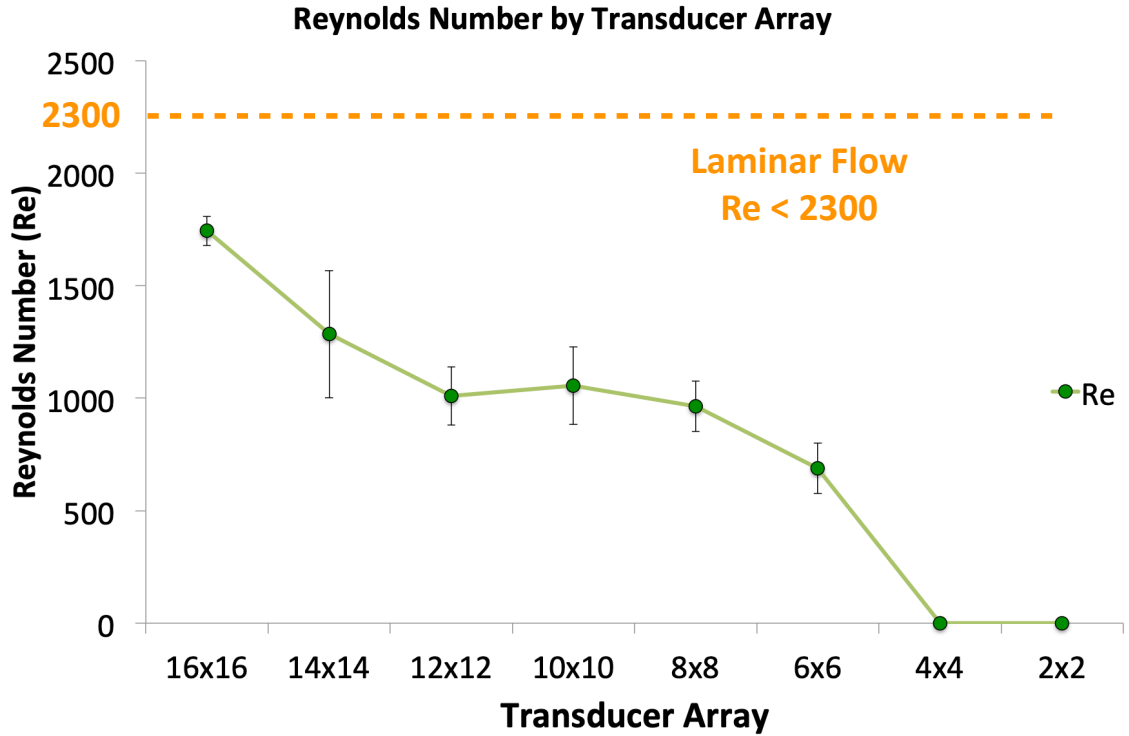


Figure 4.10: Graph of the Reynolds number ( $Re$ ) according to a different number of transducers. The threshold value for the laminar was below 2,300, while turbulent was above 2,300.

#### 4.4.4 Minimum transducers and SPL analysis

This section describes the identification of the minimum number of transducers and SPL required to induce airflow.

##### 4.4.4.1 Minimum transducer array required

To establish the minimum transducer array required for the proposed system, this work studied the  $Re$  and airflow speed. The objective here was to find the smallest transducer array that would satisfy two conditions: 1) it can produce airflow; 2) the airflow is laminar. From the findings, a 6 x 6 array met the required conditions. An array that is lower than 4 x 4 is not able to produce an airflow (airspeed  $\sim 0$  m/s), even though it produces laminar flow. Interestingly, Figure 4.11 (a) shows that the SPL distribution for the 6 x 6 and 4 x 4 arrays diverged at  $z \approx 42$  mm, roughly at SPL value of  $\sim 98$  dB. This behaviour and value suggests that  $\sim 98$  dB is the minimum SPL threshold required to induce airflow (independently of the transducer arrangement).

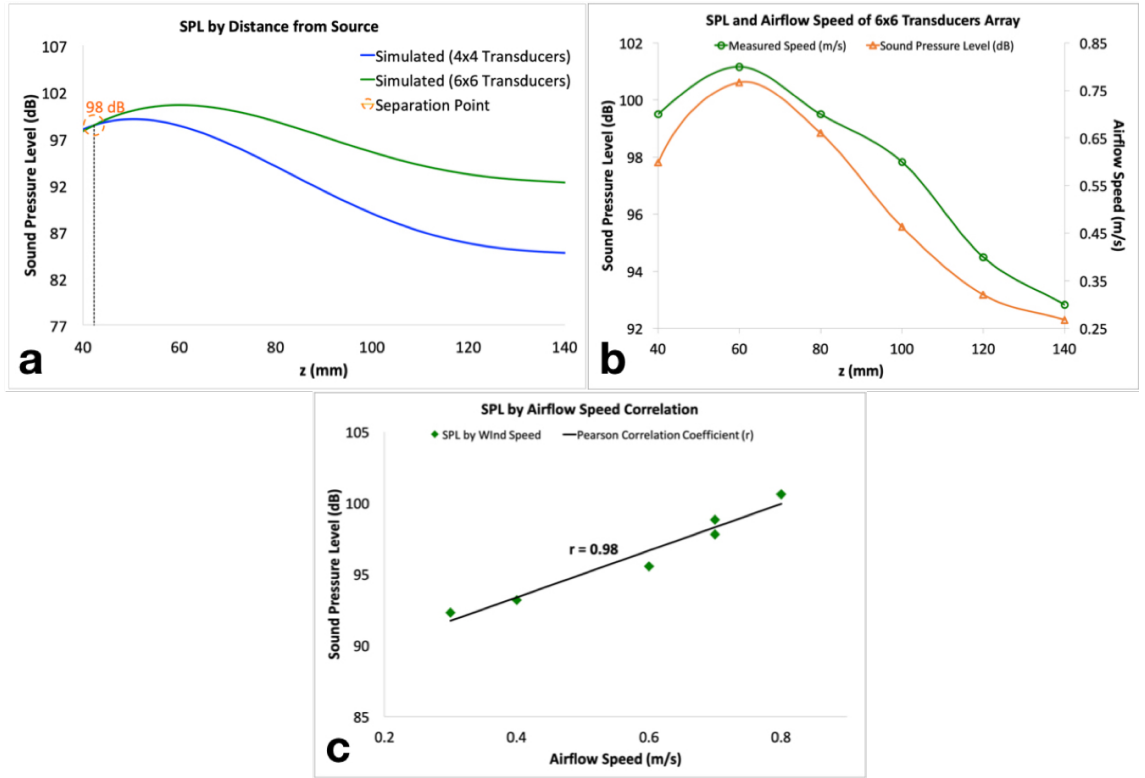


Figure 4.11: Graphs of Sound Pressure Level and its resulting flows: (a) the measured airflow speed by distance from the transducers array – a 6 x 6 array shows the gradual fluctuation of airflow speed while a 4 x 4 array remains constant (0 m/s); (b) a graph of simulated sound pressure level (SPL) by distance from the transducer array, where SPL separation of 6 x 6 and 4 x 4 happened at  $\approx 42$  mm; (c) a graph of simulated SPL and measured airflow speed showed a similar trend; (d) a graph of correlation of simulated SPL and the measured airflow speed for a 6 x 6 PAT.

#### 4.4.4.2 SPL and wind correlation

The correlation between SPL and airflow speed, particularly for a 6 x 6 array, was studied. The graph in Figure 4.11 (b) shows that SPL and airflow speed indicated a similar trend: a peak at 60 mm then a gradual reduction towards 140 mm (the Pearson correlation coefficient method was used to find the relationship between them). Figure 4.11 (c) illustrates this relationship. The correlation value was  $r = 0.98$ , which implied that there is a strong correlation between SPL and airflow speed (i.e., the airflow speed increased as the SPL increased). Therefore, this study suggests that, to increase the airflow speed using ultrasound, one can increase the SPL (e.g., by increase the transducer's voltage).

## 4.5 Evaluation

This section describes and reports the evaluation and the results of the proposed method's performance. It is reported in terms of the lateral mist resolution by oscillation frequency.

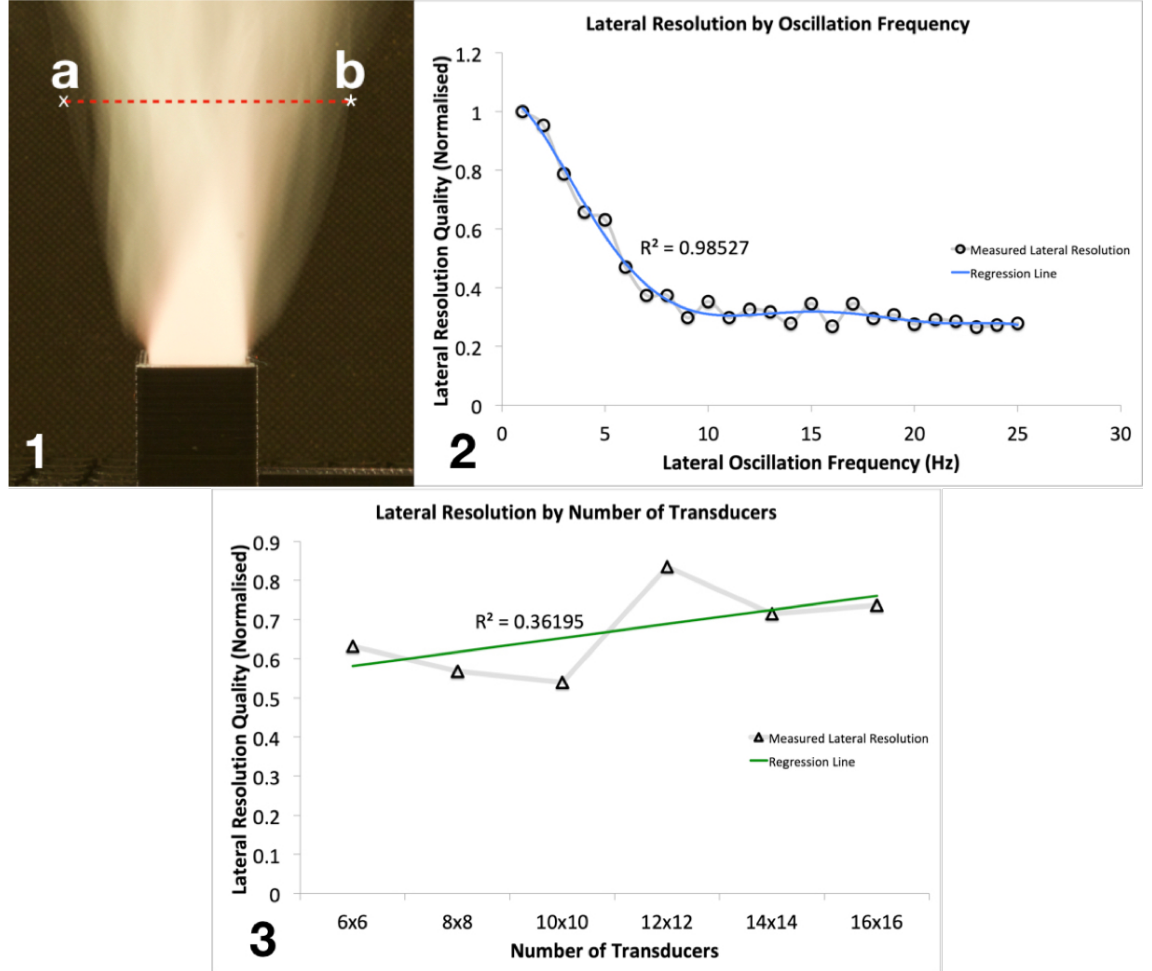


Figure 4.12: Lateral resolution: (1) an example photo that used a long exposure of two seconds to evaluate lateral resolution. (the resolution is measured from (a) to (b)); (2) regression analysis of the laminar mist lateral resolution with different oscillation frequencies; (3) Regression analysis of the mist's lateral resolution using a different quantities of transducers.

### 4.5.1 Lateral mist resolution by oscillation frequencies

To evaluate the lateral resolution of the laminar mist, the following steps were carried out: First, oscillation frequency was defined. One complete oscillation (i.e., 1 Hz) meant that the reference point had moved entirely from the left ( $\Delta x = -15$  mm) to the right ( $\Delta x = 15$

mm)<sup>3</sup>. Second, the reference point was continuously shifted, based on the predetermined oscillation frequency, but within the displacement limit. Third, a camera was fixed 150 mm away from the setup, and ten photos of the mist motion with two seconds exposure were captured (e.g., see Figure 4.12 (1)). Finally, a maximum distance of the aerosol along  $z_s = 60$  mm (denoted as (a) and (b) in the figure) was calculated. These three steps were repeated for a different oscillations of up to 25 Hz. Then, the results were normalised using the result achieved at 1 Hz, and this was denoted as lateral resolution.

Figure 4.12 (2) illustrates the results of lateral resolution according to the oscillation frequency. A regression line throughout the measured data was computed. The regression resulting in a value of  $R^2 = 0.99$ , which indicated that oscillation frequency could be reliably used to predict the lateral resolution. The figure also shows that the lateral resolution of the laminar aerosol decreased gradually when the oscillation frequency was increased from 1 Hz to 8 Hz. The reason for this was that the mist particles had a time delay of  $\sim 30$  ms to adequately respond to the beam (Hasegawa et al., 2018). However, the laminar aerosol lateral resolution remained constant from 9 Hz to 25 Hz. This finding indicates that the lowest lateral resolution was found when lateral oscillation frequency reached 9 Hz.

#### 4.5.2 Lateral mist resolution according to number of transducers

This work also evaluated the effect on laminar mist resolution as a result of reducing the number of transducers. First, the oscillation frequency was fixed to 5 Hz as changes to lateral oscillation are small at higher frequencies. Then, ten photographs per array were recorded and the lateral mist resolution was computed (similar to the previous section). Figure 4.12 (3) shows that the results of mist's lateral resolution in relation to the size of the array. The fitting was poor ( $R^2 = 0.36 < 0.5$ ), implying that even if a tendency can be observed in the data (i.e., lateral resolution increases marginally alongside with the size of the array), it is difficult to confirm such a correlation between mist behaviour and transducer numbers.

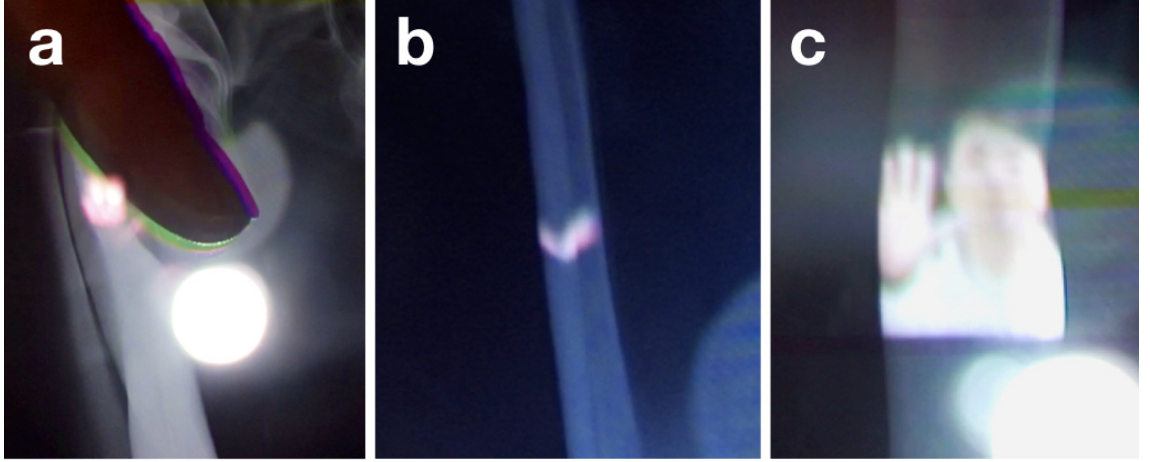


Figure 4.13: Applications enabled by SonicSpray: (a) a game of whack-a-mole; (b) a projection of a butterfly that is moving in 3D spatial space, (c) a visual of a person in a video call application.

## 4.6 Enabling applications with SonicSpray

SonicSpray demonstrate a compact design for aerosol-based mid-air displays, controlled with ultrasound, offering key benefits when compared to other approaches (i.e., a compact form factor, reconfigurable in both  $X$ - and  $Y$ -axes, silent operation, and no enclosures). Although SonicSpray should be considered as a control technique that can complement the capabilities of other aerosol techniques in a number of different cases, its unique features allowed this study to explore novel applications, even when using SonicSpray as the only control technique. By controlling the motion of a 2D stroke on the  $XY$ -plane, SonicSpray enabled applications for experiential learning. For example, a user can touch and follow a point in 3D space onto the reconfigurable laminar aerosol (e.g., the user can draw shapes or letters). This work also explored a game application, for example, whack-a-mole game, as shown in Figure 4.13 (a), here, the flow and acoustic pressure provided additional tactile sensations on the user's finger.

Another innovative application is creating it as a mid-air display. SonicSpray enables a reconfigurable projection that can be controlled spatially and precisely in mid-air. Figure 4.13 (b) shows an animated butterfly is projected and synced with the reconfigured laminar mist. Such mid-air displays can also project a different types of useful content such as a video conference (see Figure 4.13 (c)), where a visual of a user appears in mid-air to have a conversation with the audience. The combination of these screen transformations will

---

<sup>3</sup>This displacement limit ( $\Delta x = \pm 15$  mm) is identified in the section titled, 'Lateral reconfiguration of the basic beam'.

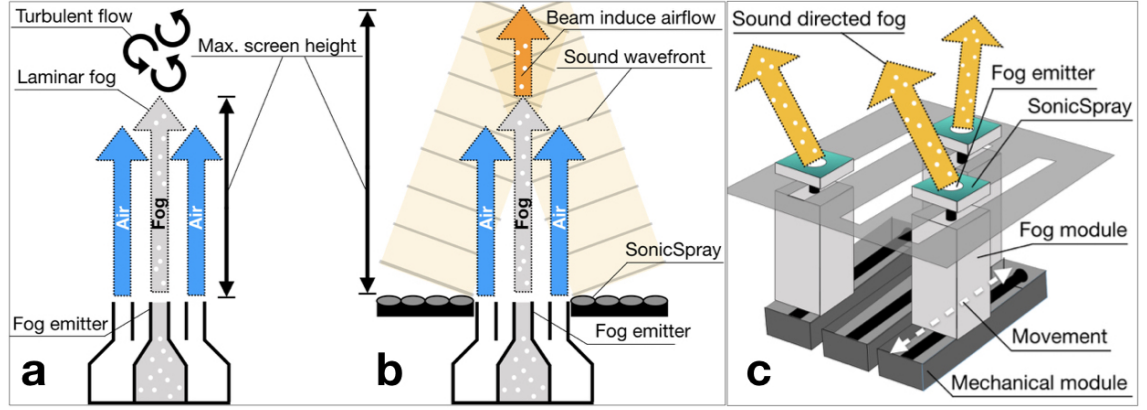


Figure 4.14: SonicSpray can be used as a single permeable mid-air display and can also complement other reconfiguration techniques: (a) in conventional fog screens the protective airflow degrades (slows) as it rises, and the fog display becomes turbulent; (b) SonicSpray can induce flows, even for initially static air/fog and accelerate the air of the protective flow in a fog screen to increase its operational size; (c) SonicSpray is mounted on mechanically moving emitters to provide a wider display and large horizontal displacements.

allow the user to formulate a screen without the need for mechanical features (avoiding noise). SonicSpray can precisely control the laminar flow in mid-air, which is useful for art applications (e.g., airbrush drawing) and light painting applications, as indicated in the work by [Huang et al. \(2018\)](#). The technique can serve as an alternative to the bulky robotic arm that is used drawing work. SonicSpray also can be used to create small display features, e.g., the Fairy Light of femtoseconds laser ([Ochiai et al., 2016b](#)), while retaining a safe touch interface.

## 4.7 Discussion

SonicSpray offers interesting the potential for producing and controlling laminar aerosol flows, which are required for creating permeable mid-air displays. The technique presents clear advantages when compared to other control techniques, such as avoiding moving parts (e.g., fans and mechanical actuators that produce noise), and allowing direct access to the display volume (i.e., by avoiding transparent electrodes), and allowing reconfiguration in mid-air (e.g., MistForm is limited to one axis control, and aerosol always flows vertically). However, as a standalone technique, SonicSpray is only suited to relatively small form factors and small lateral displacements (size depends on the type of modulator -PAT or MM - used). Additionally, the need to retain the laminarity of the flow places limitations on the speed of the actuation achievable (although this is shared by all other approaches).



SonicSpray can contribute to traditional fog screens, which generate a laminar airflow to protect fog and retain display properties. This protective flow degrades (slows) as it rises, and when fully degraded, the fog display becomes turbulent (i.e., the degradation of the protective flow limits the vertical size of the fog screen; see Figure 4.14 (a)). As explored in this chapter, SonicSpray can induce flows of (0.3–0.8 m/s) from low SPLs (92–101 dB), even for initially static air/fog. This can be used to continue to accelerate the air of the protective flow in a fog screen, thereby increasing their operational size (see Figure 4.14 (b)). SonicSpray can also potentially serve work as an excellent complement to other aerosol control approaches and form factors, such as those created by Lam et al. (2014, 2015b,a). For example, by mounting Sonic Spray around the array of emitters (Lam et al., 2015b,a) or on the mechanically moving emitters (Lam et al., 2014) (see Figure 4.14 (c)), the moving emitters can be used to provide a wider display and larger horizontal displacements, and the proposed technique can be employed to enable further mid-air control (steering in the  $XY$ -plane, as the fog raises). The electrode array in the work by Sahoo et al. (2015) can only control fog in one axis (to or from the electrodes), while SonicSpray can provide control along an additional axis and/or the initial direction of the flow (i.e., towards the electrodes) for further control of fog trajectories.

These combinations, however, will come at the expense of sacrificing other benefits with SonicSpray (i.e., introducing fans will result in noise, introducing electrodes will result in enclosures, and larger formats will require larger arrays), but they illustrate the potential of SonicSpray as an enabling technology for exploring novel mid-air display formats.

## 4.8 Conclusion

This chapter presented SonicSpray, a technique that employs steerable ultrasound Bessel beams to create and control laminar flows, with significant potential for being a control technique for permeable, mid-air displays. This chapter described the control techniques to produce such beams, and explored their potential application to both for PATs and hybrid modulators. This chapter explored achievable form factors (e.g., sizes) and the resulting laminar flow speeds, as well as the PATs levels required to create them (e.g., 0.8 m/s at 60 mm and 98 dB). SonicSpray can be as a sole technique (i.e., no initial air flow) or as technological compliment to the current permeable mid-air displays, enabling compact and mobile experiences. It can serve as an interesting additional control technique and enable exploration of new reconfigurable and permeable mid-air displays.

## Chapter 5

# Final conclusion and future work

This chapter describes the final chapter of this thesis.

### 5.1 Recapitulation of research purpose and findings

This thesis addressed the difficulties involved in reconfiguring permeable mid-air displays through the experimental investigations of three interactive prototypes: MistForm, SoundBender, and SonicSpray. Each of the prototypes include their own specific reconfigurability techniques. Chapter 2 described a straightforward technique used by MistForm to coarsely and mechanically reconfigure permeable mid-air displays. Throughout the investigation, MistForm was capable of turning problems into solutions; for example, a concave display (see Figure 2.10 (C)) can be used as a shared screen. However, the investigation found the initial prototype of MistForm to be large and noisy. These challenges have led to an experimental investigation of SoundBender in Chapter 3.

Chapter 3 described an investigation of SoundBender, a hybrid technique that reconfigured non-solid diffusers. The technique was precisely manipulating any given complex sound field, encoded by a MM mounted on PAT. The force from the sound affected the surrounding particles. The technique was able to reconfigure matter such as paper, mist, and flame in air space. However, this chapter did not focus on how to coordinate its use specifically for permeable mid-air displays. Therefore, this thesis carried out another investigation into SonicSpray, as presented in Chapter 4.

Chapter 4 investigated SonicSpray, a technique that reconfigured a permeable mid-air display through a minimal form factor device (a PAT and a hybrid setup). It featured a technique that was capable of reconfiguring non-solid diffusers without any physical contact or physical guidance, while the diffused matter remained laminar in air. It can be

used as a standalone technique or as a secondary technique to complement other current reconfiguration techniques. In the case of latter, this thesis suggests how SoundBender may be able to increase the operational capabilities of these techniques, for example, by redirecting aerosols of mechanically-controlled fog emitters.

## 5.2 Contribution to the body of knowledge

This thesis contributes three reconfiguration techniques for permeable mid-air displays with sufficient reconfigurability (both coarse and fine manipulation). The techniques were investigated through three interactive prototypes, MistForm, SoundBender, and Sonic-Spray. This thesis described the design of the proposed techniques, investigated their performance, and coordinated their use for HCI applications.

## 5.3 Implications of the findings

Three papers have been published that were created as part of this thesis (two in the HCI field, one in the acoustic field), and one of which was fully accepted to an HCI conference proceeding. Therefore, to demonstrate the implications of this thesis, this section looks at citations made by other researchers, regardless of their field.

Chapter 2, which discusses MistForm, indicated the system's capability of coarsely reconfiguring permeable mid-air displays with a mechanical approach. Although the work has found critical limitations of the technique, such as its bulk and noise, the work is capable of being used as adaptive and interactive fog screen. This unique capability has inspired researchers to explore and extend their research towards the interactions display (Yamada et al., 2018; Popovici et al., 2019). Yamada et al. (2018) acknowledged MistForm as an intuitive 3D display based on fog screens. MistForm is one of the works that inspired Yamada et al. (2018) to develop a real-time 3D interactive display for holographic display. This is done through graphic's parallel processing. It is capable of reconfiguring (e.g., scaling and rotating) a holographic image made from a 4,096-point light source in real-time, instructed by the movement of the user's finger (e.g., pinching and swiping). Meanwhile, Popovici et al. (2019) acknowledged MistForm as one of the display prototypes that has advanced the technology of today's displays. MistForm inspired Popovici et al. (2019) to create a concept for an active TV interface, a concept that uses the spatial locations of hands in free air as shortcuts to TV channels.

Meanwhile, SoundBender (as described in Chapter 3), inspired the researchers to ex-

plore mid-air displays with other physical objects (Freeman et al., 2019), and to shape a sound field for audible displays with the use of the MM (Memoli et al., 2019). Freeman et al. (2019) acknowledged that SoundBender offers benefit to mid-air displays' visibility. SoundBender uses only a single sound emitter that allows matter to be manipulated in the air, even in the presence of obstacles, while the work by Freeman et al. (2019) uses an opposed emitter and emitter-reflector setup that limits the visibility of the display. The key difference is that Freeman et al. (2019) studied an acoustically transparent object that was included on top of their emitter, creating an interactive display of the static physical object. Memoli et al. (2019) highlight the same key problems, as stated in Chapter 3, i.e., the problem of a bulky and expensive system in HCI that includes a phased array, and the static condition of the 3D printed MM. Memoli et al. (2019) has referred to the generic steps suggested by SoundBender to produce an audio spotlight. The proposed audio spotlight is more cost-effective compared to expensive audio spotlights currently used in the HCI community.

While this thesis was being written, SonicSpray (Chapter 4) was fully accepted in the 2019 ACM International Conference on Interactive Surfaces and Spaces (ISS 2019), which suggests that the chapter is highly relevant and can contribute its benefits, such as precisely reconfiguring mid-air displays through a minimal form factor, to the HCI community.

## 5.4 Research strengths and limitations

This section discusses the strengths and limitations occurred of the study.

### 5.4.1 Strengths

This thesis outline the strengths pertaining to reconfiguring the mid-air displays of three interactive prototypes: MistForm, SoundBender, and SonicSpray. MistForm, is the first mid-air display that offers the advantages of interaction between the reconfigurable display of permeable particles and real hands, without the need to switch focus between the display and the user's hand, as the case for displays using the light-converging concept (e.g., optical combiners and concave mirrors), alongside another conventional display system. Consider the example of users who only be able to directly interact with 3D objects using their hands in front of the CAVE wall, with a proxy (i.e., a virtual hand) being necessary for interaction beyond this area (so that they can focus on the wall and ignore their real

hands). Benefits also apply in training scenarios such as those involving surgery, where tools (e.g., scalpels) are central to the task at hand. In this context, MistForm allows hands, scalpel, and organs to remain in focus, in the virtual environment.

Since they will not need to wear HMD, a trainee will be aware of their surroundings and able to engage with other users as in the real world (e.g., nurses in an operation theatre). Other technologies will require need virtual reconstructions as mediators, such as avatars, tools, and virtual hands. Transparent HMDs for example, have an image plane (usually at 3.5 m) and there is no optical overlap with the clients hand. Hands can be reconstructed in VR, but designers will miss on client’s facial expressions. In contrast, MistForm dynamic ZoC allows both hands and content to remain in focus throughout the entire manipulation range (the range increases from 7 to 30 cm), unleashing the full dexterity of the user’s real hands for interaction (assuming required sensing technology), and recognising gestures (e.g., the client pointing of an object) and facial expressions. MistForm has the ability to reconfigure screen shapes to control the fog’s visibility (i.e., brightness, blending, visibility and focus). It is able to change the shape of the fog screen, mitigating common issues in fog screens such as blending and uneven brightness. It can create areas of shared visibility, personalised views, or a tailored location of view zones. It is also capable of enabling entirely new possibilities for the dynamic ZoC through its reconfigurable features.

The most relevant strength of SoundBender is that it is the first to introduce the first systematic exploration of a hybrid system to recreate high-fidelity (i.e., complex) sound fields, not otherwise available using PATs. The main reason for that is that PATs miss higher frequencies that lead to aliasing when reconstructing a complex sound field. SoundBender refines the exploration into a structured method that can be used by the HCI community. The sound field reconfiguration in SoundBender can be used in application beyond those affecting visual display (e.g., haptics, sound, and smells). To the best of my knowledge, prior to the paper on SoundBender being published, there was no other technique that could recreate complex sound fields (e.g., self-bending beams) or enable applications to control non-solid matter behind obstacles, or facilitate the applications envisioned in the discussion of Chapter 3, which demonstrated SoundBender’s capabilities in enabling three novel modalities around an obstacle: levitation, haptics, and non-solid features. Chapter 3 also discussed the potential of some of these applications, such as haptic feed-forward for interacting with a tangible object, the creation of interactive toys, and smell delivery mechanisms.

SonicSpray, provides an innovative technique for laminar flow reconfiguration, which was the main primary limitation of previous systems (Sahoo et al., 2015). This is achieved through a minimal form factor device that retains laminar flow while providing significant benefits, i.e., avoid enclosures (Sahoo et al., 2015), no noisy mechanical parts (Lam et al., 2014, 2015b,a; Tokuda et al., 2017), and precise mid-air control (Seah et al., 2014). As means for testing the potential of this technique, the chapter described the design for creating a prototype that solely relied on this technique (i.e., no fans and no electric fields), and that has already demonstrated examples (such as butterfly in 3D space) beyond the capabilities of previous approaches (i.e., it was silent, allowed movement in 3D space, and had no enclosures). In addition, it had the ability to avoid ghost beams found in prior research (Hasegawa et al., 2017). The technique presented in this chapter is valid for practitioners reusing it with either MM or PATs.

In the case of SonicSpray, while the generated aerosol remained laminar, it offered clear advantages in comparison to other reconfiguration techniques. For example, it can avoid moving parts such as fans and mechanical actuators that produce noise, allows direct access to the display volume (i.e., it avoids the use of transparent electrodes), and allows the reconfiguration of aerosols in mid-air (e.g., MistForm is limited to one-axis control, and aerosol always flows vertically). Furthermore, SonicSpray can also complement other aerosol control approaches, for example, by mounting SonicSpray around the array of static or mechanically-moving fog emitters. This can provide a wider display and large horizontal displacements, and enable further mid-air control of the aerosols by steering in the  $XY$ -plane. Traditional fog screens generate a laminar airflow to protect fog and retain laminar display properties. However, this protective flow degrades (i.e., slows) as it rises, causing the fog display to become turbulent and no longer laminar, which will limit the vertical size of the fog screens. As explored in Chapter 4, SonicSpray can induce flows of (0.3–0.8 m/s) from low SPLs (92–101 dB), even for initially static air/fog. This can be used to continuously accelerate the protective flow and increase the operational size of the fog screens.

This thesis also explored the minimum number of transducers required to reconfigure a narrow mist for display purposes (a 6 x 6 PAT). The minimal concept offered in this thesis can be used as an alternative technique to provide additional non-visual informations (e.g., haptics, parametric sound, odours, and hot air) in HCI applications. One work that demonstrated the provisioning of such information is the one by Nakajima et al. (2018), where it provided a cool sensation as feedback to a user by using a Bessel beam remotely.

This can be used as an alternative to an air jet, which was previously used by [Suzuki and Kobayashi \(2005\)](#) to provide haptic feedback in a VR application. However, [Nakajima et al. \(2018\)](#) did not study a minimal form factor for the system. The research in this thesis had the advantage of incorporating the minimal concept into the system.

### 5.4.2 Limitations

Three critical limitations were found in this thesis. The first concerns the noise and bulky design of MistForm (Chapter 2). Although MistForm’s fog screen is reconfigurable and enables novel interactive features, it is noisy (66 dB at the user’s position, slightly louder than an air conditioning system). This problem, however, was solved in another study, as detailed in Chapter 4, where a technique is that is capable of finely reconfiguring matter in free air silently, and in a minimal form factor. This study is described in Chapters 3 and 4.

The second limitation is the hard-coded phase shifts that produce a high-fidelity sound field, as discussed in Chapter 3. The phase was encoded by through MM, which is a static 3D printed structure. However, it is this hard-coded element that allows the recreation of complex sound-fields, which cannot be done by PATs, and enables new applications of displays even in the presence of obstacles (e.g., levitation around a passive object, haptic feedback above passive object, and control of non-solid around a passive object)

The third limitation was found through the investigation of SonicSpray in Chapter 4, where fog particles suffered from poor response to low ultrasonic energy. In the study, the airflow speed of the particles was found decreased proportionally to the number of transducers used. In the future, researchers can improve the response rate of the particles by using a source with greater sound power.

## 5.5 Future work

This section explains possible research directions and interesting applications beyond the scope of this thesis.

### 5.5.1 Reconfigurable volumetric displays of permeable materials

This thesis offers the concept of a minimal mid-air display that steers aerosols, where the shape of the display is changeable and touchable. This advantage will inspire work on making swept-volume displays more minimal and touchable in comparison to current



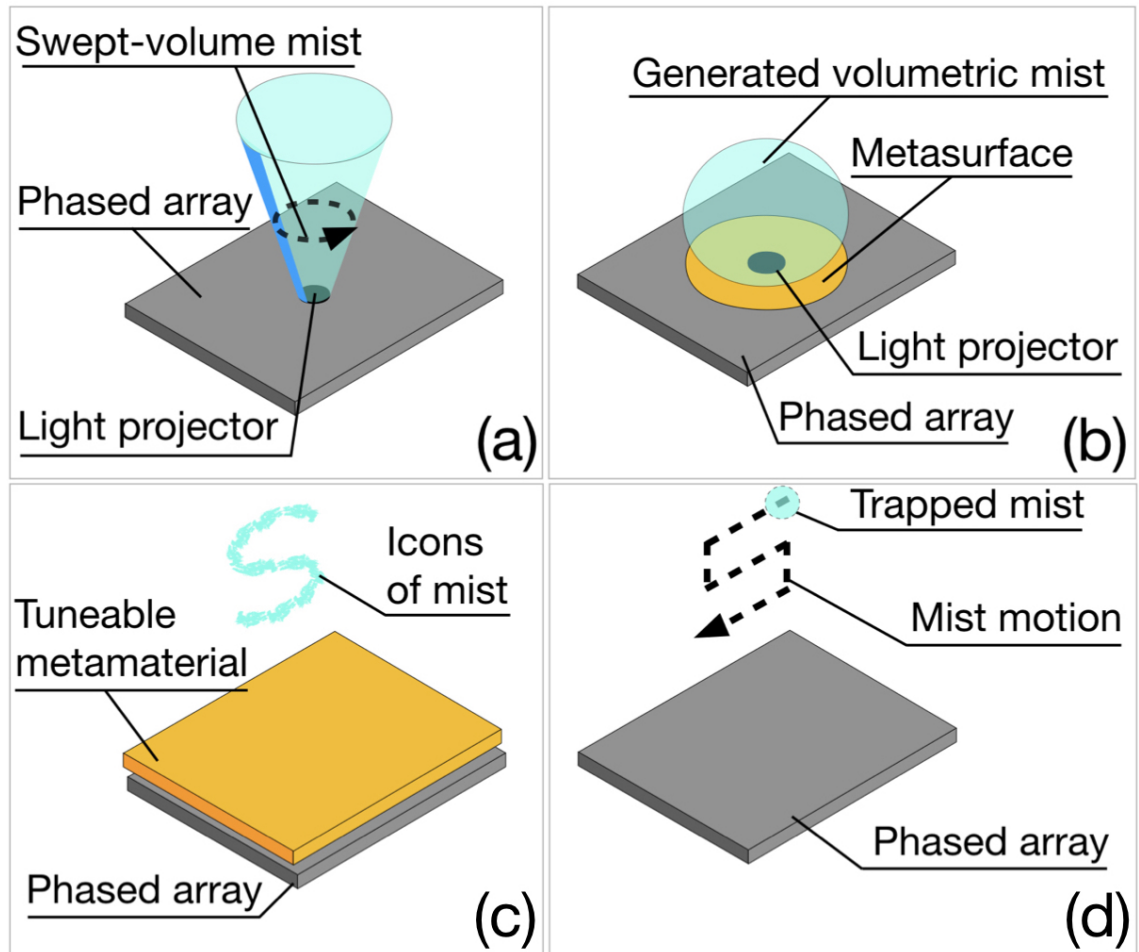


Figure 5.1: Future reconfigurable displays with new concepts: (a) a swept-volume display made from reconfigurable aerosols, (b) the volumetric display of a hybrid modulator (i.e., a PAT combined with MM), (c) icons made of mist, which are generated through tuneable MM, (d) a mid-air display made from trapped permeable materials.

swept-volume displays (for instance, research such as conducted by [Hunter et al. \(2017\)](#) and [Karnik et al. \(2011\)](#), which demonstrated a large swept-volume display that does not allow a user to touch the display directly). SonicSpray is capable of reconfiguring a narrow mist to form a volumetric shape, as shown in Figure 5.1 (a), at a persistence of vision  $\approx 12$  Hz. However, researchers will need to address the issue of the weak reaction of permeable materials to sound energy. There are several ways in which to address this problem, e.g., exploration of the mist reaction to sound energy. An investigation into the mist reaction at different sound powers should be studied with the aim of finding sound power at which the mists reacts instantaneously. Other possible explorations include an inquiry into the mist reaction at different ultrasound frequencies, and the studies on the reactions of different size of particles at different ultrasound frequencies. By solving this reaction issue, a light projector can be synchronised with the steered mist, creating a display beyond fan holograms with LEDs<sup>1</sup>. Additionally, SoundBender, which is a hybrid device (i.e., a hybrid setup of PAT and MM), can inspire work on volumetric displays (as in Figure 5.1 (b)). It is capable of constructing a volumetric sound field through an axisymmetric design of a metasurface. A designer can imagine as if revolving a volume in a 3D software package, but create the volume in the real-world using the axisymmetric design. The sound energy will force permeable materials to form the volumetric shape, and the sound field can be reconfigured (e.g., stretched and steered) through the PAT. A projector can be used to display graphical content on the formed mist, or alternatively, researchers can add a back-propagation method ([Zhang et al., 2014](#)) to transform the volumetric shape further away from the ultrasound source. The methods above are safer, more reliable, less noisy, and offer a small form factor when compared to current swept-volume displays of permeable matter ([Lam et al., 2014, 2015a](#)).

### 5.5.2 Dynamic displays with tunable MM

This thesis has introduced a hybrid modulator, a combination of a PAT and MM for displays, which represent the fastest way of exploring the capabilities of MM to reconfigure matter in free air. This research can inspire researchers to achieve greater reconfigurability beyond that demonstrated in this thesis (i.e., via SoundBender and SonicSpray), meaning that a higher degree of control for the MM can be explored. One option is to design a tunable MM, which will eventually allow permeable materials to be configured through the MM at a higher precision than with a PAT, since the use of MM can produce high fidelity

<sup>1</sup><https://www.360digitalsignage.com/product-item/3d-hologram-fan-displays/>

sound fields. The study for such reconfiguration will be able to uncover new capabilities for shaping sound fields, particularly within the HCI community. For example, directing audible sound or odours in a curvature, as in the work of [Hasegawa et al. \(2019\)](#), but with higher precision achieved by using MM, or as shown in Figure 5.1 (c), where the MM was designed to form a complex icon in mid-air through the generated sound field. Acoustic MM is a challenging task; however, interest in the investigation of this topic is growing even in the acoustic MM community, which will be beneficial to both the HCI and acoustic MM communities. SoundBender and SonicSpray have the potential to allow HCI practitioners to access more complex sound-fields, following the current thesis addressing the primary challenges and pitfalls of a hybrid modulator. New algorithms can be created to allow even better control of the static field generated by MM, and researchers can further explore dynamic MM in order to gain greater control over the permeable matter induced by the sound field.

### 5.5.3 Reconfigurable displays of trapped permeable materials

This thesis has demonstrated the ability to steer a narrow aerosol in a spatial location by using ultrasound. This capability will inspire studies on techniques for trapping permeable matter with acoustic trapping, as existing research has previously trapped only solid objects for mid-air displays. The idea is to trap the non-solid particles (e.g., mist) using a PAT (as seen in Figure 5.1 (d)), then move them at high speed (higher than the persistence of vision) in mid-air. Following on, an RGB light projector can be synchronised with the motion of the trapped mist to create an interactive visual display. This trapping technique has been shown to work in both optical ([Smalley et al., 2018b](#)) and electrical ([Berthelot and Bonod, 2019](#)) fields. Both of the works cited here trapped and moved permeable materials for their displays. However, ultrasound approach to this trapping technique remains unexplored.

## 5.6 Final conclusion

In conclusion, this thesis has already addressed the difficulty of reconfiguring permeable mid-air displays through the experimental investigation of three interactive prototypes: MistForm, SoundBender, and SonicSpray. All three prototypes demonstrated techniques for sufficiently reconfiguring the display using coarse and fine control, and have also been accepted by the HCI community. For example, [Memoli et al. \(2019\)](#) posit SoundBender

as an example of a hybrid system that will become a future sound modulator. The reason for this is that the MM can be of minimal form factor, and is cheaper and easier to fabricate compared to phased arrays. [Memoli et al. \(2019\)](#) stated that it can be used for application with the irregular shape of sound effected through conventional speakers. Scenarios include sending specific sounds to only a certain part of an audience, to pertinent space, and extending the range of haptic devices even behind obstacles, which can make a device like Google Home or Amazon Echo smarter. The reconfigurable mid-air displays of permeable matter, as described and demonstrated in this thesis, have advanced current technology, as noted by [Popovici et al. \(2019\)](#). This advanced display can also be used in area such as visualisation for 3D printers, educational objects in medical and science context, interactive public kiosks, smartphones and small form factor display devices, architecture, and in interaction with dirty hands (e.g., in kitchens or industrial design workshops).

This thesis has carried out research aimed at reconfiguring permeable materials. It presented and described prototypes that are capable of achieving this with sufficient reconfigurability. The hybrid method has already indicated significant capability for reconfiguring permeable materials in mid-air displays. More value can be added to this thesis if it were to propose and explore tunable acoustic MM. However, this will require a significant amount of time and resources. Therefore, any continuation of the study on reconfiguring permeable mid-air displays should consider the prototypes in this thesis, which should be treated as anchors for developing new knowledge related to future mid-air displays.

# Bibliography

- Alakärppä, I., Jaakkola, E., Colley, A., and Häkkinen, J. (2017). Breathscreen: Design and evaluation of an ephemeral ui. In *Proceedings of the 2017 CHI Conference on Human Factors in Computing Systems*, CHI '17, pages 4424–4429, New York, NY, USA. ACM. [87](#), [91](#)
- Alexander, J., Roudaut, A., Steimle, J., Hornbæk, K., Bruns Alonso, M., Follmer, S., and Merritt, T. (2018). Grand challenges in shape-changing interface research. In *Proceedings of the 2018 CHI Conference on Human Factors in Computing Systems*, CHI '18, pages 299:1–299:14, New York, NY, USA. ACM. [87](#), [89](#)
- Alrøe, T., Grann, J., Grönvall, E., Petersen, M. G., and Rasmussen, J. L. (2012). Aerial tunes: Exploring interaction qualities of mid-air displays. In *Proceedings of the 7th Nordic Conference on Human-Computer Interaction: Making Sense Through Design*, NordiCHI '12, pages 514–523, New York, NY, USA. ACM. [1](#), [5](#), [8](#), [48](#), [90](#)
- Ando, S., Otao, K., Takazawa, K., Tanemura, Y., and Ochiai, Y. (2017). Aerial image on retroreflective particles. In *SIGGRAPH Asia 2017 Posters*, SA '17, pages 7:1–7:2, New York, NY, USA. ACM. [87](#)
- Andrade, M. A. B., Bernassau, A. L., and Adamowski, J. C. (2016). Acoustic levitation of a large solid sphere. *Applied Physics Letters*, 109(4):044101. [53](#)
- Baresch, D., Thomas, J.-L., and Marchiano, R. (2016). Observation of a single-beam gradient force acoustical trap for elastic particles: Acoustical tweezers. *Phys. Rev. Lett.*, 116:024301. [53](#)
- Barnkob, R., Augustsson, P., Laurell, T., and Bruus, H. (2012). Acoustic radiation- and streaming-induced microparticle velocities determined by microparticle image velocimetry in an ultrasound symmetry plane. *Phys. Rev. E*, 86:056307. [101](#)

- Barnum, P. C., Narasimhan, S. G., and Kanade, T. (2010). A multi-layered display with water drops. *ACM Trans. Graph.*, 29(4):76:1–76:7. [10](#), [25](#)
- Bau, O., Petrevski, U., and Mackay, W. (2009). Bubblewrap: A textile-based electromagnetic haptic display. In *CHI '09 Extended Abstracts on Human Factors in Computing Systems*, CHI EA '09, pages 3607–3612, New York, NY, USA. ACM. [21](#)
- Berthelot, J. and Bonod, N. (2019). Free-space micro-graphics with electrically driven levitated light scatterers. *Optics letters*, 44 6:1476–1479. [5](#), [7](#), [117](#)
- Bimber, O. (2004). Combining optical holograms with interactive computer graphics. *Computer*, 37(1):85–91. [3](#), [22](#)
- Black, S. (2013). *Iron Man 3*. Marvel Studios. [2](#), [86](#)
- Brandt, E. H. (2001). Suspended by sound. *Nature*, 413:474. [52](#), [59](#)
- Butler, A., Hilliges, O., Izadi, S., Hodges, S., Molyneaux, D., Kim, D., and Kong, D. (2011). Vermeer: Direct interaction with a 360 viewable 3d display. In *Proceedings of the 24th Annual ACM Symposium on User Interface Software and Technology*, UIST '11, pages 569–576, New York, NY, USA. ACM. [3](#), [23](#)
- Carter, T., Seah, S. A., Long, B., Drinkwater, B., and Subramanian, S. (2013). Ultra-haptics: Multi-point mid-air haptic feedback for touch surfaces. In *Proceedings of the 26th Annual ACM Symposium on User Interface Software and Technology*, UIST '13, pages 505–514, New York, NY, USA. ACM. [12](#), [51](#), [53](#), [76](#), [84](#)
- Catmull, E. and Rom, R. (1974). A class of local interpolating splines. In Barnhill, R. E. and Riesenfeld, R. F., editors, *Computer Aided Geometric Design*, pages 317 – 326. Academic Press. [69](#)
- Chen, X., Xu, X., Ai, S., Chen, H., Pei, Y., and Zhou, X. (2014). Active acoustic metamaterials with tunable effective mass density by gradient magnetic fields. *Applied Physics Letters*, 105(7):071913. [56](#)
- Ciolek, T. M. and Kendon, A. (1980). Environment and the spatial arrangement of conversational encounters. *Sociological Inquiry*, 50(3-4):237–271. [42](#)
- Coelho, M., Ishii, H., and Maes, P. (2008). Surflex: A programmable surface for the design of tangible interfaces. In *CHI '08 Extended Abstracts on Human Factors in Computing Systems*, CHI EA '08, pages 3429–3434, New York, NY, USA. ACM. [21](#)

- Coelho, M. and Zigelbaum, J. (2011). Shape-changing interfaces. *Personal and Ubiquitous Computing*, 15(2):161–173. [20](#), [22](#)
- Colombi, A., Colquitt, D., Roux, P., Guenneau, S., and Craster, R. V. (2016). A seismic metamaterial: The resonant metawedge. *Scientific Reports*, 6:27717. Article. [55](#), [57](#)
- Din, I., Anwar, H., Syed, I., Zafar, H., and Hasan, L. (2014). Projector calibration for pattern projection systems. *Journal of Applied Research and Technology*, 12(1):80 – 86. [98](#)
- Eitoku, S., Hashimoto, K., and Tanikawa, T. (2006). Controllable water particle display. In *Proceedings of the 2006 ACM SIGCHI International Conference on Advances in Computer Entertainment Technology*, ACE ‘06, New York, NY, USA. ACM. [10](#)
- Eitoku, S.-i., Nishimura, K., Tanikawa, T., and Hirose, M. (2009). Study on design of controllable particle display using water drops suitable for light environment. In *Proceedings of the 16th ACM Symposium on Virtual Reality Software and Technology*, VRST ‘09, pages 23–26, New York, NY, USA. ACM. [10](#), [25](#)
- Ens, B. M., Finnegan, R., and Irani, P. P. (2014). The personal cockpit: A spatial interface for effective task switching on head-worn displays. In *Proceedings of the 32Nd Annual ACM Conference on Human Factors in Computing Systems*, CHI ‘14, pages 3171–3180, New York, NY, USA. ACM. [42](#)
- Follmer, S., Leithinger, D., Olwal, A., Hogge, A., and Ishii, H. (2013). inform: Dynamic physical affordances and constraints through shape and object actuation. In *Proceedings of the 26th Annual ACM Symposium on User Interface Software and Technology*, UIST ‘13, pages 417–426, New York, NY, USA. ACM. [20](#)
- Foresti, D., Nabavi, M., Klingauf, M., Ferrari, A., and Poulikakos, D. (2013). Acoustophoretic contactless transport and handling of matter in air. *Proceedings of the National Academy of Sciences*, 110(31):12549–12554. [49](#), [83](#)
- Freeman, E., Marzo, A., Kourtelos, P. B., Williamson, J. R., and Brewster, S. (2019). Enhancing physical objects with actuated levitating particles. In *Proceedings of the 8th ACM International Symposium on Pervasive Displays*, PerDis ‘19, pages 2:1–2:7, New York, NY, USA. ACM. [111](#)
- Freeman, E., Williamson, J., Subramanian, S., and Brewster, S. (2018). Point-and-shake: Selecting from levitating object displays. In *Proceedings of the 2018 CHI Conference*



- on *Human Factors in Computing Systems*, CHI '18, pages 18:1–18:10, New York, NY, USA. ACM. [2](#), [5](#), [8](#), [87](#), [90](#)
- Gao, H., Gu, Z.-m., Liang, B., Zou, X.-y., Yang, J., Yang, J., and Cheng, J.-c. (2016). Acoustic focusing by symmetrical self-bending beams with phase modulations. *Applied Physics Letters*, 108(7):073501. [57](#)
- Greenfield, E., Segev, M., Walasik, W., and Raz, O. (2011). Accelerating light beams along arbitrary convex trajectories. *Phys. Rev. Lett.*, 106:213902. [57](#)
- Hachet, M., Bossavit, B., Cohé, A., and de la Rivière, J.-B. (2011). Toucheo: Multitouch and stereo combined in a seamless workspace. In *Proceedings of the 24th Annual ACM Symposium on User Interface Software and Technology*, UIST '11, pages 587–592, New York, NY, USA. ACM. [22](#)
- Hardy, J., Weichel, C., Taher, F., Vidler, J., and Alexander, J. (2015). Shapeclip: Towards rapid prototyping with shape-changing displays for designers. In *Proceedings of the 33rd Annual ACM Conference on Human Factors in Computing Systems*, CHI '15, pages 19–28, New York, NY, USA. ACM. [21](#)
- Hasegawa, K., Qiu, L., Noda, A., Inoue, S., and Shinoda, H. (2017). Electronically steerable ultrasound-driven long narrow air stream. *Applied Physics Letters*, 111(6):064104. [92](#), [93](#), [96](#), [113](#)
- Hasegawa, K., Qiu, L., and Shinoda, H. (2018). Mid-air ultrasound fragrance rendering. *IEEE Transactions on Visualization and Computer Graphics*, 24(4):1477–1485. [12](#), [91](#), [96](#), [105](#)
- Hasegawa, K., Yuki, H., and Shinoda, H. (2019). Curved acceleration path of ultrasound-driven air flow. *Journal of Applied Physics*, 125(5):054902. [117](#)
- Hertz, H. M. (1995). Standing-wave acoustic trap for nonintrusive positioning of micro-particles. *Journal of Applied Physics*, 78(8):4845–4849. [52](#), [54](#)
- Hilliges, O., Kim, D., Izadi, S., Weiss, M., and Wilson, A. (2012). Holodesk: Direct 3d interactions with a situated see-through display. In *Proceedings of the SIGCHI Conference on Human Factors in Computing Systems*, CHI '12, pages 2421–2430, New York, NY, USA. ACM. [23](#)

- Hoffman, D. M., Girshick, A. R., Akeley, K., and Banks, M. S. (2008). Vergence–accommodation conflicts hinder visual performance and cause visual fatigue. *Journal of Vision*, 8(3):33–33. [27](#), [41](#)
- Huang, Y., Tsang, S.-C., Wong, H.-T. T., and Lam, M.-L. (2018). Computational light painting and kinetic photography. In *Proceedings of the Joint Symposium on Computational Aesthetics and Sketch-Based Interfaces and Modeling and Non-Photorealistic Animation and Rendering*, Expressive ‘18, pages 14:1–14:9, New York, NY, USA. ACM. [107](#)
- Hunter, S., Azuma, R., Moisant-Thompson, J., MacLeod, D., and Disanji, D. (2017). Mid-air interaction with a 3d aerial display. In *ACM SIGGRAPH 2017 Emerging Technologies*, SIGGRAPH ‘17, pages 17:1–17:2, New York, NY, USA. ACM. [3](#), [116](#)
- Ion, A., Wall, L., Kovacs, R., and Baudisch, P. (2017). Digital mechanical metamaterials. In *Proceedings of the 2017 CHI Conference on Human Factors in Computing Systems*, CHI ‘17, pages 977–988, New York, NY, USA. ACM. [49](#)
- Ishii, H., Lakatos, D., Bonanni, L., and Labrune, J.-B. (2012). Radical atoms: Beyond tangible bits, toward transformable materials. *interactions*, 19(1):38–51. [1](#), [20](#), [48](#)
- Iwata, H., Yano, H., Nakaizumi, F., and Kawamura, R. (2001). Project feelex: Adding haptic surface to graphics. In *Proceedings of the 28th Annual Conference on Computer Graphics and Interactive Techniques*, SIGGRAPH ‘01, pages 469–476, New York, NY, USA. ACM. [20](#), [21](#)
- Karnik, A., Henderson, A., Dean, A., Pang, H., Campbell, T., Sakurai, S., Herrmann, G., Izadi, S., Kitamura, Y., and Subramanian, S. (2011). Vortex: Design and implementation of an interactive volumetric display. In *CHI ‘11 Extended Abstracts on Human Factors in Computing Systems*, CHI EA ‘11, pages 2017–2022, New York, NY, USA. ACM. [116](#)
- Kataoka, A. and Kasahara, Y. (1993). Method and apparatus for a fog screen and image-forming method using the same. US Patent 5,270,752. [25](#)
- Kimura, H., Asano, A., Fujishiro, I., Nakatani, A., and Watanabe, H. (2011). True 3d display. In *ACM SIGGRAPH 2011 Emerging Technologies*, SIGGRAPH ‘11, pages 20:1–20:1, New York, NY, USA. ACM. [5](#), [24](#)

- Kimura, H., Uchiyama, T., and Yoshikawa, H. (2006). Laser produced 3d display in the air. In *ACM SIGGRAPH 2006 Emerging Technologies*, SIGGRAPH '06, New York, NY, USA. ACM. [5](#), [24](#)
- Kono, M., Hoshi, T., and Kakehi, Y. (2014). Lapillus bug: Creature-like behaving particles based on interactive mid-air acoustic manipulation. In *Proceedings of the 11th Conference on Advances in Computer Entertainment Technology*, ACE '14, pages 34:1–34:8, New York, NY, USA. ACM. [90](#)
- Korres, G. and Eid, M. (2016). Haptogram: Ultrasonic point-cloud tactile stimulation. *IEEE Access*, 4:7758–7769. [80](#)
- Kota, M. and Nakatera, K. (1996). Ultrasonic sensor. US Patent 5,495,766. [54](#), [72](#)
- Lam, M., Chen, B., and Huang, Y. (2015a). A novel volumetric display using fog emitter matrix. In *2015 IEEE International Conference on Robotics and Automation (ICRA)*, pages 4452–4457. [24](#), [91](#), [108](#), [113](#), [116](#)
- Lam, M., Chen, B., Lam, K., and Huang, Y. (2014). 3d fog display using parallel linear motion platforms. In *2014 International Conference on Virtual Systems Multimedia (VSMM)*, pages 234–237. [10](#), [12](#), [24](#), [88](#), [90](#), [91](#), [108](#), [113](#), [116](#)
- Lam, M.-L., Huang, Y., and Chen, B. (2015b). Interactive volumetric fog display. In *SIGGRAPH Asia 2015 Emerging Technologies*, SA '15, pages 13:1–13:2, New York, NY, USA. ACM. [86](#), [91](#), [108](#), [113](#)
- Lee, J., Ha, K., and Shung, K. K. (2005). A theoretical study of the feasibility of acoustical tweezers: Ray acoustics approach. *The Journal of the Acoustical Society of America*, 117(5):3273–3280. [53](#)
- Lee, J., Olwal, A., Ishii, H., and Boulanger, C. (2013). Spacetop: Integrating 2d and spatial 3d interactions in a see-through desktop environment. In *Proceedings of the SIGCHI Conference on Human Factors in Computing Systems*, CHI '13, pages 189–192, New York, NY, USA. ACM. [23](#)
- Lee, J., Post, R., and Ishii, H. (2011). Zeron: Mid-air tangible interaction enabled by computer controlled magnetic levitation. In *Proceedings of the 24th Annual ACM Symposium on User Interface Software and Technology*, UIST '11, pages 327–336, New York, NY, USA. ACM. [5](#), [7](#), [48](#), [89](#), [90](#)

- Lee, J. and Shung, K. K. (2006). Radiation forces exerted on arbitrarily located sphere by acoustic tweezer. *The Journal of the Acoustical Society of America*, 120(2):1084–1094. [53](#)
- Lee, J., Teh, S.-Y., Lee, A., Kim, H. H., Lee, C., and Shung, K. K. (2009). Single beam acoustic trapping. *Applied Physics Letters*, 95(7):073701. [57](#)
- Li, D., Levin, D. I. W., Matusik, W., and Zheng, C. (2016). Acoustic voxels: computational optimization of modular acoustic filters. *ACM Trans. Graph.*, 35(4):88:1–88:12. [49](#)
- Li, Y. and Assouar, M. B. (2015). Three-dimensional collimated self-accelerating beam through acoustic metascreen. *Scientific Reports*, 5:17612. Article. [57](#)
- Li, Y., Jiang, X., Li, R.-q., Liang, B., Zou, X.-y., Yin, L.-l., and Cheng, J.-c. (2014a). Experimental realization of full control of reflected waves with subwavelength acoustic metasurfaces. *Phys. Rev. Applied*, 2:064002. [55](#), [57](#)
- Li, Y., Lee, C., Chen, R., Zhou, Q., and Shung, K. K. (2014b). A feasibility study of in vivo applications of single beam acoustic tweezers. *Appl Phys Lett*, 105(17):173701–173701. [57](#)
- Long, B., Seah, S. A., Carter, T., and Subramanian, S. (2014). Rendering volumetric haptic shapes in mid-air using ultrasound. *ACM Trans. Graph.*, 33(6):181:1–181:10. [49](#), [51](#), [53](#), [59](#), [70](#), [76](#)
- Lucas, G. (1977). *Star Wars*. Twentieth Century Fox Film Corp. [1](#)
- Maldovan, M. (2013). Sound and heat revolutions in phononics. *Nature*, 503:209. Review Article. [57](#)
- Marquardt, D. (1963). An algorithm for least-squares estimation of nonlinear parameters. *Journal of the Society for Industrial and Applied Mathematics*, 11(2):431–441. [30](#)
- Martinez Plasencia, D., Berthaut, F., Karnik, A., and Subramanian, S. (2014a). Through the combining glass. In *Proceedings of the 27th Annual ACM Symposium on User Interface Software and Technology*, UIST ‘14, pages 341–350, New York, NY, USA. ACM. [23](#)
- Martinez Plasencia, D., Joyce, E., and Subramanian, S. (2014b). Mistable: Reach-through personal screens for tabletops. In *Proceedings of the 32nd Annual ACM Conference on*

- Human Factors in Computing Systems*, CHI '14, pages 3493–3502, New York, NY, USA. ACM. [1](#), [10](#), [25](#), [36](#), [40](#), [44](#)
- Marzo, A. (2016). Gauntlev: A wearable to manipulate free-floating objects. In *Proceedings of the 2016 CHI Conference on Human Factors in Computing Systems*, CHI '16, pages 3277–3281, New York, NY, USA. ACM. [48](#), [49](#), [53](#)
- Marzo, A., Barnes, A., and Drinkwater, B. W. (2017a). Tinylev: A multi-emitter single-axis acoustic levitator. *Review of Scientific Instruments*, 88(8):085105. [7](#)
- Marzo, A., Corkett, T., and Drinkwater, B. W. (2018). Ultraino: An open phased-array system for narrowband airborne ultrasound transmission. *IEEE Transactions on Ultrasonics, Ferroelectrics, and Frequency Control*, 65(1):102–111. [98](#)
- Marzo, A., Ghobrial, A., Cox, L., Caleap, M., Croxford, A., and Drinkwater, B. W. (2017b). Realization of compact tractor beams using acoustic delay-lines. *Applied Physics Letters*, 110(1):014102. [53](#)
- Marzo, A., Seah, S. A., Drinkwater, B. W., Sahoo, D. R., Long, B., and Subramanian, S. (2015). Holographic acoustic elements for manipulation of levitated objects. *Nature Communications*, 6:8661. Article. [51](#), [53](#), [75](#), [84](#), [90](#)
- McAtamney, L. and Corlett, E. N. (1993). Rula: a survey method for the investigation of work-related upper limb disorders. *Applied Ergonomics*, 24(2):91 – 99. [43](#)
- Melde, K., Mark, A. G., Qiu, T., and Fischer, P. (2016). Holograms for acoustics. *Nature*, 537:518. [55](#)
- Memoli, G., Caleap, M., Asakawa, M., Sahoo, D. R., Drinkwater, B. W., and Subramanian, S. (2017). Metamaterial bricks and quantization of meta-surfaces. *Nature Communications*, 8:14608. Article. [54](#), [55](#), [56](#), [59](#), [61](#), [71](#), [77](#), [96](#)
- Memoli, G., Chisari, L., Eccles, J. P., Caleap, M., Drinkwater, B. W., and Subramanian, S. (2019). Vari-sound: A varifocal lens for sound. In *Proceedings of the 2019 CHI Conference on Human Factors in Computing Systems*, CHI '19, pages 483:1–483:14, New York, NY, USA. ACM. [111](#), [117](#), [118](#)
- Monnai, Y., Hasegawa, K., Fujiwara, M., Yoshino, K., Inoue, S., and Shinoda, H. (2014). Haptomime: Mid-air haptic interaction with a floating virtual screen. In *Proceedings of the 27th Annual ACM Symposium on User Interface Software and Technology*, UIST '14, pages 663–667, New York, NY, USA. ACM. [3](#), [23](#)

- Moreno, D. and Taubin, G. (2012). Simple, accurate, and robust projector-camera calibration. In *2012 Second International Conference on 3D Imaging, Modeling, Processing, Visualization Transmission*, pages 464–471. [98](#)
- Nakajima, M., Hasegawa, K., Makino, Y., and Shinoda, H. (2018). Remotely displaying cooling sensation via ultrasound-driven air flow. In *2018 IEEE Haptics Symposium (HAPTICS)*, pages 340–343. [113](#), [114](#)
- Norasikin, M. A., Martinez-Plasencia, D., Memoli, G., and Subramanian, S. (2019). Sonicspray: A technique to reconfigure permeable mid-air displays. In *Proceedings of the 2019 ACM International Conference on Interactive Surfaces and Spaces*, ISS '19, page 113–122, New York, NY, USA. Association for Computing Machinery. [13](#), [14](#), [15](#), [47](#), [85](#), [86](#)
- Norasikin, M. A., Martinez Plasencia, D., Polychronopoulos, S., Memoli, G., Tokuda, Y., and Subramanian, S. (2018). Soundbender: Dynamic acoustic control behind obstacles. In *Proceedings of the 31st Annual ACM Symposium on User Interface Software and Technology*, UIST '18, pages 247–259, New York, NY, USA. ACM. [13](#), [14](#), [15](#), [47](#), [85](#), [88](#), [91](#), [92](#), [93](#), [96](#)
- Norasikin, M. A., Memoli, G., Plasencia, D. M., and Subramanian, S. (2017). Acoustic levitation by a metamaterial-based cloak. In *24th International Congress on Sound and Vibration*, ICSV '24. [47](#), [85](#)
- Nyquist, H. (1928). Certain topics in telegraph transmission theory. *Transactions of the American Institute of Electrical Engineers*, 47(2):617–644. [49](#), [54](#), [60](#), [72](#)
- Ochiai, Y., Hoshi, T., and Rekimoto, J. (2014). Pixie dust: Graphics generated by levitated and animated objects in computational acoustic-potential field. *ACM Trans. Graph.*, 33(4):85:1–85:13. [2](#), [5](#), [48](#), [52](#), [53](#), [59](#), [83](#), [86](#), [90](#)
- Ochiai, Y., Kumagai, K., Hoshi, T., Hasegawa, S., and Hayasaki, Y. (2016a). Cross-field aerial haptics: Rendering haptic feedback in air with light and acoustic fields. In *Proceedings of the 2016 CHI Conference on Human Factors in Computing Systems*, CHI '16, pages 3238–3247, New York, NY, USA. ACM. [80](#)
- Ochiai, Y., Kumagai, K., Hoshi, T., Rekimoto, J., Hasegawa, S., and Hayasaki, Y. (2016b). Fairy lights in femtoseconds: aerial and volumetric graphics rendered by focused femto-second laser combined with computational holographic fields. *ACM Trans. Graph.*, 35(2):17:1–17:14. [4](#), [5](#), [24](#), [107](#)

- Okada, N., Shimobaba, T., Ichihashi, Y., Oi, R., Yamamoto, K., Oikawa, M., Kakue, T., Masuda, N., and Ito, T. (2013). Band-limited double-step fresnel diffraction and its application to computer-generated holograms. *Opt. Express*, 21(7):9192–9197. [70](#), [75](#)
- Olwal, A., DiVerdi, S., Rakkolainen, I., and Höllerer, T. (2007). Consigalo: Multi-user face-to-face interaction on immaterial displays. In *Proceedings of the 2Nd International Conference on INtelligent TEchnologies for Interactive enterTAINment*, INTETAIN ‘08, pages 8:1–8:9, ICST, Brussels, Belgium, Belgium. ICST (Institute for Computer Sciences, Social-Informatics and Telecommunications Engineering). [25](#)
- Omirou, T., Marzo, A., Seah, S. A., and Subramanian, S. (2015). Levipath: Modular acoustic levitation for 3d path visualisations. In *Proceedings of the 33rd Annual ACM Conference on Human Factors in Computing Systems*, CHI ‘15, pages 309–312, New York, NY, USA. ACM. [48](#), [51](#), [52](#), [59](#), [90](#)
- Omirou, T., Perez, A. M., Subramanian, S., and Roudaut, A. (2016). Floating charts: Data plotting using free-floating acoustically levitated representations. In *2016 IEEE Symposium on 3D User Interfaces (3DUI)*, pages 187–190, Greenville, SC, USA. IEEE. [5](#), [7](#), [52](#), [59](#), [90](#)
- Otao, K. and Koga, T. (2017). Mistflow: A fog display for visualization of adaptive shape-changing flow. In *SIGGRAPH Asia 2017 Posters*, SA ‘17, pages 17:1–17:2, New York, NY, USA. ACM. [87](#)
- Palovuori, K. and Rakkolainen, I. (2012). The vanishing display: An autovisible immaterial display. In *Proceeding of the 16th International Academic MindTrek Conference*, MindTrek ‘12, pages 175–177, New York, NY, USA. ACM. [10](#)
- Pangaro, G., Maynes-Aminzade, D., and Ishii, H. (2002). The actuated workbench: Computer-controlled actuation in tabletop tangible interfaces. In *Proceedings of the 15th Annual ACM Symposium on User Interface Software and Technology*, UIST ‘02, pages 181–190, New York, NY, USA. ACM. [21](#)
- Parkes, A., Poupyrev, I., and Ishii, H. (2008). Designing kinetic interactions for organic user interfaces. *Commun. ACM*, 51(6):58–65. [20](#)
- Perlin, K. et al. (2006). Volumetric display with dust as the participating medium. US Patent 6,997,558. [10](#), [11](#), [12](#), [25](#)



- Pesce, G., Volpe, G., Maragó, O. M., Jones, P. H., Gigan, S., Sasso, A., and Volpe, G. (2015). Step-by-step guide to the realization of advanced optical tweezers. *J. Opt. Soc. Am. B*, 32(5):B84–B98. [60](#), [75](#), [93](#)
- Popa, B.-I., Shinde, D., Konneker, A., and Cummer, S. A. (2015). Active acoustic metamaterials reconfigurable in real time. *Phys. Rev. B*, 91:220303. [56](#)
- Popovici, I., Schipor, O.-A., and Vataavu, R.-D. (2019). Hover: Exploring cognitive maps and mid-air pointing for television control. *International Journal of Human-Computer Studies*, 129:95 – 107. [110](#), [118](#)
- Poston, T. and Serra, L. (1994). The virtual workbench: Dextrous vr. In *Proceedings of the Conference on Virtual Reality Software and Technology*, VRST ‘94, pages 111–121, River Edge, NJ, USA. World Scientific Publishing Co., Inc. [22](#)
- Poupyrev, I., Nashida, T., Maruyama, S., Rekimoto, J., and Yamaji, Y. (2004). Lumen: Interactive visual and shape display for calm computing. In *ACM SIGGRAPH 2004 Emerging Technologies*, SIGGRAPH ‘04, New York, NY, USA. ACM. [20](#), [21](#)
- Poynting, J. H. and Thomson, J. J. (1906). *A text-book of physics. Sound*. Charles Griffin and Company. [52](#)
- Press, W. H., Teukolsky, S. A., Vetterling, W. T., and Flannery, B. P. (1988). *Numerical recipes in C. the art of scientific computing*. Press Syndicate of the University of Cambridge. [54](#)
- Qiu, H., Uno, Y., Sai, T., Iguchi, S., Mizutani, Y., Hoshi, T., Kawahara, Y., Takehi, Y., and Takamiya, M. (2018). Luciola: A light-emitting particle moving in mid-air based on ultrasonic levitation and wireless powering. In *SIGGRAPH Asia 2018 Emerging Technologies*, SA ‘18, pages 7:1–7:2, New York, NY, USA. ACM. [2](#), [5](#), [86](#), [90](#)
- Rakkolainen, I. (2008a). Measurements and experiments of the immaterial virtual reality display. In *2008 3DTV Conference: The True Vision - Capture, Transmission and Display of 3D Video*, pages 37–40. [25](#), [32](#)
- Rakkolainen, I. (2008b). Mid-air displays enabling novel user interfaces. In *Proceedings of the 1st ACM International Workshop on Semantic Ambient Media Experiences*, SAME ‘08, pages 25–30, New York, NY, USA. ACM. [10](#), [25](#), [40](#), [88](#), [89](#), [91](#)

- Rakkolainen, I. and Palovuori, K. (2005). Laser scanning for the interactive walk-through fog screen. In *Proceedings of the ACM Symposium on Virtual Reality Software and Technology*, VRST '05, pages 224–226, New York, NY, USA. ACM. [10](#)
- Rakkolainen, I. and Sand, A. (2013). A movable immaterial volumetric display. In *SIGGRAPH Asia 2013 Posters*, SA '13, pages 2:1–2:1, New York, NY, USA. ACM. [87](#), [88](#), [91](#)
- Rakkolainen, I. K. and Lugmayr, A. K. (2007). Immaterial display for interactive advertisements. In *Proceedings of the International Conference on Advances in Computer Entertainment Technology*, ACE '07, pages 95–98, New York, NY, USA. ACM. [10](#)
- Rasmussen, M. K., Pedersen, E. W., Petersen, M. G., and Hornbæk, K. (2012). Shape-changing interfaces: A review of the design space and open research questions. In *Proceedings of the SIGCHI Conference on Human Factors in Computing Systems*, CHI '12, pages 735–744, New York, NY, USA. ACM. [22](#)
- Rogers, Y. (2006). Moving on from weiser’s vision of calm computing: Engaging ubicomp experiences. In Dourish, P. and Friday, A., editors, *UbiComp 2006: Ubiquitous Computing*, pages 404–421, Berlin, Heidelberg. Springer Berlin Heidelberg. [1](#)
- Roudaut, A., Karnik, A., Löchtefeld, M., and Subramanian, S. (2013). Morphees: Toward high ”shape resolution” in self-actuated flexible mobile devices. In *Proceedings of the SIGCHI Conference on Human Factors in Computing Systems*, CHI '13, pages 593–602, New York, NY, USA. ACM. [21](#)
- Ruiz-Avila, J. (2016). Holovect: Holographic vector display. [1](#), [2](#), [10](#), [11](#), [12](#), [86](#)
- Sahoo, D. R., Martinez Plasencia, D., and Subramanian, S. (2015). Control of non-solid diffusers by electrostatic charging. In *Proceedings of the 33rd Annual ACM Conference on Human Factors in Computing Systems*, CHI '15, pages 11–14, New York, NY, USA. ACM. [5](#), [6](#), [11](#), [12](#), [24](#), [83](#), [86](#), [87](#), [88](#), [89](#), [91](#), [101](#), [108](#), [113](#)
- Sahoo, D. R., Nakamura, T., Marzo, A., Omirou, T., Asakawa, M., and Subramanian, S. (2016). Joled: A mid-air display based on electrostatic rotation of levitated janus objects. In *Proceedings of the 29th Annual Symposium on User Interface Software and Technology*, UIST '16, pages 437–448, New York, NY, USA. ACM. [5](#), [7](#), [49](#), [51](#), [52](#), [90](#)
- Saito, H., Kimura, H., Shimada, S., Naemura, T., Kayahara, J., Jarusirisawad, S., Nozick, V., Ishikawa, H., Murakami, T., Aoki, J., Asano, A., Kimura, T., Kakehata, M., Sasaki,

- F., Yashiro, H., Mori, M., Torizuka, K., and Ino, K. (2008). Laser-plasma scanning 3d display for putting digital contents in free space. In *Proceedings of SPIE - The International Society for Optical Engineering*, volume 6803. [5](#), [24](#)
- Salter, P. S., Iqbal, Z., and Booth, M. J. (2013). Analysis of the three-dimensional focal positioning capability of adaptive optic elements. *International Journal of Optomechatronics*, 7(1):1–14. [60](#), [75](#), [93](#)
- Schneegass, S., Alt, F., Scheible, J., and Schmidt, A. (2014). Mid-air displays: concept and first experiences with free-floating pervasive displays. In *Proceedings of The International Symposium on Pervasive Displays*, PerDis ‘14, pages 27:27–27:31, New York, NY, USA. ACM. [25](#)
- Seah, S. A., Martinez Plasencia, D., Bennett, P. D., Karnik, A., Otrocol, V. S., Knibbe, J., Cockburn, A., and Subramanian, S. (2014). Sensabubble: A chrono-sensory mid-air display of sight and smell. In *Proceedings of the SIGCHI Conference on Human Factors in Computing Systems*, CHI ‘14, pages 2863–2872, New York, NY, USA. ACM. [2](#), [89](#), [113](#)
- Shibata, T., Kim, J., Hoffman, D. M., and Banks, M. S. (2011). The zone of comfort: Predicting visual discomfort with stereo displays. *Journal of Vision*, 11(8):11–11. [19](#), [41](#)
- Siviloglou, G. A. and Christodoulides, D. N. (2007). Accelerating finite energy airy beams. *Opt. Lett.*, 32(8):979–981. [57](#)
- Smalley, D., Poon, T.-C., Gao, H., Kvavle, J., and Qaderi, K. (2018a). Volumetric displays: turning 3-d inside-out. *Opt. Photon. News*, 29(6):26–33. [10](#), [11](#), [12](#), [87](#)
- Smalley, D. E., Nygaard, E., Squire, K., Van Wagoner, J., Rasmussen, J., Gneiting, S., Qaderi, K., Goodsell, J., Rogers, W., Lindsey, M., Costner, K., Monk, A., Pearson, M., Haymore, B., and Peatross, J. (2018b). A photophoretic-trap volumetric display. *Nature*, 553:486 EP –. [5](#), [8](#), [9](#), [48](#), [117](#)
- Sodhi, R., Poupyrev, I., Glisson, M., and Israr, A. (2013). Aireal: Interactive tactile experiences in free air. *ACM Trans. Graph.*, 32(4):134:1–134:10. [1](#)
- Sundvik, M., Nieminen, H. J., Salmi, A., Panula, P., and Hæggström, E. (2015). Effects of acoustic levitation on the development of zebrafish, danio rerio, embryos. *Scientific Reports*, 5:13596. Article. [52](#), [54](#)

- Sutherland, I. E. (1965). The ultimate display. In *Proceedings of IFIP Congress*, volume 506. 1, 48
- Suzuki, I., Yoshimitsu, S., Kawahara, K., Ito, N., Shinoda, A., Ishii, A., Yoshida, T., and Ochiai, Y. (2016). Gushed diffusers: Fast-moving, floating, and lightweight mid-air display. In *Proceedings of the 29th Annual Symposium on User Interface Software and Technology*, UIST ‘16 Adjunct, pages 69–70, New York, NY, USA. ACM. 2, 87, 88, 91
- Suzuki, Y. and Kobayashi, M. (2005). Air jet driven force feedback in virtual reality. *IEEE Computer Graphics and Applications*, 25(1):44–47. 114
- Takashima, K., Oyama, T., Asari, Y., Sharlin, E., Greenberg, S., and Kitamura, Y. (2016). Study and design of a shape-shifting wall display. In *Proceedings of the 2016 ACM Conference on Designing Interactive Systems*, DIS ‘16, pages 796–806, New York, NY, USA. ACM. 22
- Tokuda, Y., Hiyama, A., Hirose, M., and Yamamoto, H. (2015). R2d2 w/ airr: Real time & real space double-layered display with aerial imaging by retro-reflection. In *SIGGRAPH Asia 2015 Emerging Technologies*, SA ‘15, pages 20:1–20:3, New York, NY, USA. ACM. 3, 4, 23
- Tokuda, Y., Norasikin, M. A., Subramanian, S., and Martinez Plasencia, D. (2017). Mist-form: Adaptive shape changing fog screens. In *Proceedings of the 2017 CHI Conference on Human Factors in Computing Systems*, CHI ‘17, pages 4383–4395, New York, NY, USA. ACM. 13, 14, 15, 18, 86, 88, 91, 113
- Valkov, D., Steinicke, F., Bruder, G., and Hinrichs, K. (2011). 2d touching of 3d stereoscopic objects. In *Proceedings of the SIGCHI Conference on Human Factors in Computing Systems*, CHI ‘11, pages 1353–1362, New York, NY, USA. ACM. 43
- Vasileiou, T., Foresti, D., Bayram, A., Poulikakos, D., and Ferrari, A. (2016). Toward contactless biology: Acoustophoretic dna transfection. *Scientific Reports*, 6:20023. Article. 51
- Vi, C. T., Marzo, A., Ablart, D., Memoli, G., Subramanian, S., Drinkwater, B., and Obrist, M. (2017). Tastyfloats: A contactless food delivery system. In *Proceedings of the 2017 ACM International Conference on Interactive Surfaces and Spaces*, ISS ‘17, pages 161–170, New York, NY, USA. ACM. 7, 49, 83

- Waanders, J. W. (1991). *Piezoelectric ceramics: Properties and applications*. Philips Components. [54](#)
- Wang, W., Xie, Y., Popa, B.-I., and Cummer, S. A. (2016). Subwavelength diffractive acoustics and wavefront manipulation with a reflective acoustic metasurface. *Journal of Applied Physics*, 120(19):195103. [55](#)
- Weber, R. J. K., Benmore, C. J., Tumber, S. K., Taylor, A. N., Rey, C. A., Taylor, L. S., and Byrn, S. R. (2012). Acoustic levitation: recent developments and emerging opportunities in biomaterials research. *European Biophysics Journal*, 41(4):397–403. [52](#), [54](#)
- Westervelt, P. J. (1951). The theory of steady forces caused by sound waves. *The Journal of the Acoustical Society of America*, 23(3):312–315. [79](#)
- Williamson, J. R., Freeman, E., and Brewster, S. (2017). Levitate: Interaction with floating particle displays. In *Proceedings of the 6th ACM International Symposium on Pervasive Displays*, PerDis ‘17, pages 24:1–24:2, New York, NY, USA. ACM. [49](#), [53](#)
- Xie, W. J., Cao, C. D., Lü, Y. J., Hong, Z. Y., and Wei, B. (2006). Acoustic method for levitation of small living animals. *Applied Physics Letters*, 89(21):214102. [7](#), [52](#)
- Xie, Y., Shen, C., Wang, W., Li, J., Suo, D., Popa, B.-I., Jing, Y., and Cummer, S. A. (2016). Acoustic holographic rendering with two-dimensional metamaterial-based passive phased array. *Scientific Reports*, 6:35437. Article. [55](#), [56](#)
- Yagi, A., Imura, M., Kuroda, Y., and Oshiro, O. (2011). 360-deegree fog projection interactive display. In *SIGGRAPH Asia 2011 Emerging Technologies*, SA ‘11, pages 19:1–19:1, New York, NY, USA. ACM. [25](#), [46](#)
- Yamada, S., Kakue, T., Shimobaba, T., and Ito, T. (2018). Interactive holographic display based on finger gestures. *Scientific Reports*, 8(1):2010. [110](#)
- Yamamoto, H., Tomiyama, Y., and Suyama, S. (2014). Floating aerial led signage based on aerial imaging by retro-reflection (airr). *Opt. Express*, 22(22):26919–26924. [3](#), [23](#)
- Yui, T. and Hashida, T. (2016). Floatio: Floating tangible user interface based on animacy perception. In *Proceedings of the 29th Annual Symposium on User Interface Software and Technology*, UIST ‘16 Adjunct, pages 43–45, New York, NY, USA. ACM. [90](#)

- Zhang, P., Li, T., Zhu, J., Zhu, X., Yang, S., Wang, Y., Yin, X., and Zhang, X. (2014). Generation of acoustic self-bending and bottle beams by phase engineering. *Nature Communications*, 5:4316. Article. [56](#), [57](#), [60](#), [69](#), [116](#)
- Zhang, Z. (2000). A flexible new technique for camera calibration. *IEEE Transactions on Pattern Analysis and Machine Intelligence*, 22(11):1330–1334. [30](#), [33](#)
- Zhang, Z. (2000). A flexible new technique for camera calibration. *IEEE Transactions on Pattern Analysis and Machine Intelligence*, 22(11):1330–1334. [98](#)
- Zhao, S., Hu, Y., Lu, J., Qiu, X., Cheng, J., and Burnett, I. (2014). Delivering sound energy along an arbitrary convex trajectory. *Scientific Reports*, 4:6628. Article. [57](#)
- Zhao, S. and Wallaschek, J. (2011). A standing wave acoustic levitation system for large planar objects. *Archive of Applied Mechanics*, 81(2):123–139. [53](#)
- Zheng, F., Li, Y., Hsu, H.-S., Liu, C., Tat Chiu, C., Lee, C., Ham Kim, H., and Shung, K. K. (2012). Acoustic trapping with a high frequency linear phased array. *Applied Physics Letters*, 101(21):214104. [57](#)
- Zhou, P., Li, Y., Liu, S., and Su, Y. (2018). Compact design for optical-see-through holographic displays employing holographic optical elements. *Opt. Express*, 26(18):22866–22876. [3](#)

# List of Tables

1.1	Table of the practicality of permeable mid-air display techniques. . . . .	13
1.2	Table of the proposed prototypes, its features and limitations. . . . .	15
3.1	Related approaches and relevant features. . . . .	59
3.2	Various levitated materials . . . . .	68



# List of Figures

1.1	A mid-air display envisioned in Star Wars: Episode IV - A New Hope . . .	1
1.2	A mid-air display envisioned in Iron Man 3 . . . . .	2
1.3	A mid-air display made of a laser system and dusts . . . . .	2
1.4	Visual mid-air display concepts . . . . .	3
1.5	An example of light converging concept . . . . .	4
1.6	A mid-air display example of light diverging concept through lasers . . . . .	4
1.7	A mid-air display example of light scattering concept that uses a levitation setup. . . . .	5
1.8	A mid-air display of light scattering concept that uses electrostatics approach.	6
1.9	A mid-air display example of light scattering concept that uses optically trapped particle . . . . .	9
2.1	MistForm interaction . . . . .	19
2.2	An example of mechanically controlled displays . . . . .	21
2.3	MistForm system overview . . . . .	26
2.4	MistForm sampling ground truth data . . . . .	29
2.5	Estimation of the turbulence . . . . .	31
2.6	Rendering algorithm . . . . .	35
2.7	Brightness correction . . . . .	36
2.8	Reprojection error . . . . .	38
2.9	Interplay between position, brightness and blending . . . . .	39
2.10	Examples for 2D interaction . . . . .	40
2.11	Single user scenarios . . . . .	42
2.12	Display's zone of comfort . . . . .	43

2.13 Multi-user scenario . . . . .	44
3.1 Soundbender overview–bending beam . . . . .	50
3.2 Sound field examples . . . . .	51
3.3 An example of a display of light scattering particles . . . . .	53
3.4 Spatial aliasing effect . . . . .	55
3.5 Pre-designed Bezier curve . . . . .	58
3.6 Phase distribution and sampled phase . . . . .	60
3.7 Experimental setup . . . . .	61
3.8 Phased array transducer spatial spacing . . . . .	62
3.9 Metasurface for self–bending beam . . . . .	63
3.10 Measurement . . . . .	64
3.11 Experiment result of self-bending beam . . . . .	66
3.12 Visualisation of self-bending beam . . . . .	67
3.13 Summary of SoundBender method . . . . .	69
3.14 Metamaterial model . . . . .	71
3.15 Effect of spacing to SoundBender . . . . .	73
3.16 Control algorithm for several displacements . . . . .	76
3.17 Schematic of the sound measurement system . . . . .	78
3.18 Sound field representation evaluating methods . . . . .	79
3.19 A comparison of bent beam made of PAT and SoundBender . . . . .	80
3.20 Evaluating the proposed control mechanisms . . . . .	81
3.21 Application examples . . . . .	82
4.1 SonicSpray as a single and complementary technique for permeable mid-air display . . . . .	87
4.2 SonicSpray is visualising a graphical content in mid-air . . . . .	88
4.3 Geometrical representation of Bessel beam . . . . .	93
4.4 Simulation of Bessel beam using COMSOL Multiphysics . . . . .	94
4.5 Simulation of beam control algorithm . . . . .	95
4.6 Comparison of approaches (bead shifted $\Delta x = 35$ mm) . . . . .	96
4.7 SonicSpray setup . . . . .	97

4.8	Example of lateral reconfiguration . . . . .	98
4.9	Flowchart for SonicSpray . . . . .	100
4.10	Graph of the Reynolds Number (Re) by a different number of transducers .	102
4.11	Graphs of SPL and its resulting flows . . . . .	103
4.12	Lateral resolution of SonicSpray . . . . .	104
4.13	Applications enabled by SonicSpray . . . . .	106
4.14	SonicSpray as a single and complementary technique for permeable mid-air display . . . . .	107
5.1	Future reconfigurable displays with new concepts . . . . .	115

# Acronyms

**1D** one-dimensional. 70, 72

**2D** two-dimensional. 10, 15, 18, 19, 22, 24, 33, 38, 40, 41, 44, 55, 56, 62, 70, 71, 72, 90, 91, 106, 136

**3D** three-dimensional. 7, 12, 15, 18, 19, 20, 25, 27, 28, 29, 30, 33, 34, 37, 38, 41, 43, 44, 45, 46, 49, 50, 51, 52, 54, 55, 56, 57, 62, 68, 71, 72, 75, 77, 90, 93, 94, 97, 99, 106, 111, 113, 114, 116, 118

**ABS** acrylonitrile butadiene styrene. 56

**AIP** aerial imaging plate. 23

**CAVE** cave automatic virtual environment. 45, 111

**DOF** depth of field. 41

**DPT** dioptries. 41, 43

**FEM** finite element method. 77, 79, 80

**FFT** fast Fourier transform. 54

**FPGA** field-programmable gate array. 98

**HCI** human-computer interaction. v, 11, 14, 16, 17, 20, 48, 51, 52, 54, 83, 84, 85, 86, 89, 110, 111, 112, 113, 117

**HMD** head-mounted display. 1, 112

**IR** infrared. 10, 12, 22

**ISS 2019** 2019 ACM International Conference on Interactive Surfaces and Spaces. 111

- MM** metamaterial. iii, xi, 13, 16, 49, 50, 51, 54, 55, 56, 57, 61, 63, 67, 68, 69, 70, 71, 72, 73, 74, 75, 77, 80, 81, 84, 85, 88, 91, 92, 96, 107, 109, 111, 113, 114, 115, 116, 117, 118
- MOSFET** metal-oxide semiconductor field-effect transistor. 98
- OTD** optical trap display. 8
- PAT** phased array transducer. iii, 12, 13, 14, 16, 49, 51, 54, 56, 57, 61, 67, 68, 72, 73, 74, 75, 77, 78, 79, 80, 83, 84, 85, 88, 90, 91, 92, 93, 95, 96, 97, 103, 107, 108, 109, 112, 113, 114, 115, 116, 117, 137
- PC** personal computer. 98
- PWM** pulse-width modulation. 21
- Re** Reynolds number. 14, 101
- RGB** red-green-blue. 8, 117
- SMA** shape memory alloy. 20, 21
- SPL** sound pressure level. 13, 62, 78, 93, 94, 95, 96, 103, 108, 113, 138
- UART** universal asynchronous receiver/transmitter. 98
- VR** virtual reality. 28, 45, 112, 114
- ZoC** zone of comfort. 41, 42, 43, 45, 46, 47, 112